

International Journal of Thermodynamics

Editor-in-Chief

L. Kuddusi

Honorary Editors

A. Bejan

M. J. Moran

J. Szargut

G. Tsatsaronis

A. Valero

M. R. von Spakovsky

Abstracting and Indexing:

Chemical Abstracts Services, Copernicus, DOAJ, EBSCO, Emerging Sources Citation Index, Engineering Index, Google Scholar, Scopus, and ULAKBIM



***International Centre for
Applied Thermodynamics***

Editor-in-Chief

Prof. Dr. Lütfullah KUDDUSİ

Associate Editor-in-Chief

Assoc. Prof. Dr. Patrice ESTELLÉ

Prof. Dr. Enrico SCIUBBA

Associate Editor

Prof. Dr. Ali KOSAR

Prof. Dr. Rahul TEVATIA

Prof. Dr. Derya Burcu ÖZKAN

Prof. Dr. Mustafa ÖZDEMİR

Prof. Dr. Ahmet DURMAYAZ

Assoc. Prof. Dr. Onur TAYLAN

Prof. Dr. Mehmet ARİK

Prof. Dr. Ayşegül ABUŞOĞLU

Assoc. Prof. Dr. Ersin SAYAR

Prof. Dr. Hakan Fehmi ÖZTOP

Assoc. Prof. Dr. Silvio De Oliveira JUNIOR

Prof. Dr. G. Reza VAKİLİ-NEZHAAD

Prof. Dr. Bayram ŞAHİN

Editorial Board

Prof. Dr. Yasar DEMİREL

Prof. Dr. Lütfullah KUDDUSİ

Prof. Dr. Ahmet DURMAYAZ

Prof. Dr. Derya Burcu ÖZKAN

Prof. Dr. Mustafa ÖZDEMİR

Prof. Dr. Ali KOSAR

Assoc. Prof. Dr. Ersin SAYAR

Prof. Dr. Mehmet ARİK

Assoc. Prof. Dr. Abdussamet SUBASI

Daniel FAVRAT

Francois MARECHAL

Prof. Silvia Azucena NEBRA

Luis SERRA

Assoc. Prof. Dr. Onur TAYLAN

Rahul TEVATIA

Prof. Dr. Ayşegül ABUŞOĞLU

Vittorio VERDA

Gian Paolo BERETTA

Abel HERNANDEZ-GUERRERO

Nilufer EGRİCAN

Dr. Sean WRIGHT

Prof. Dr. Hakan Fehmi ÖZTOP

Assoc. Prof. Dr. Silvio De Oliveria JUNIOR

Prof. Dr. Enrico SCIUBBA

Prof. Dr. G. Reza VAKİLİ-NEZHAAD

Prof. Dr. Bayram ŞAHİN

Publishing Editor

Assoc. Prof. Dr. Abdussamet SUBASI

Assist Prof. Dr. Mustafa Yasin GÖKASLAN

Res. Assist. Ali Murat BİNARK

Language Editor

Assoc. Prof. Dr. Abdussamet SUBASI

Journal Contacts

Editor-in-Chief

Prof. Dr. Lütfullah Kuddusi

ISTANBUL TECHNICAL UNIVERSITY

kuddusi@itu.edu.tr

+902122931300/2452

Department of Mechanical Engineering

Istanbul Technical University

Gumussuyu, 34437 Istanbul Turkey

Volume: 26

Issue: 3

Web: <https://dergipark.org.tr/tr/pub/ijot>

International Journal of Thermodynamics (IJoT)

ISSN:1301-9724 / e-ISSN:2146-1511

CONTENTS	
<u>Research Article</u>	
1. Comparison Of The Electricity Generation Potentials Of Solar ORC Designed With Different Fluids Depending On Instantaneous Solar Radiation In Four Districts Of Türkiye	1-14
Serhat Yıldırım, Sadık Ata, Hüseyin Kurt, Ali Kahraman	
<u>Research Article</u>	
2. Performance Investigation of Ejector Assisted Power Cooling Absorption Cycle	15-24
Billal Mebarki	
<u>Research Article</u>	
3. Performances Investigation of the Eco-friendly Refrigerant R13I1 used as Working Fluid in the Ejector-Expansion Refrigeration Cycle	25-35
Youcef Maalem, Youcef Tamene, Hakim Madani	
<u>Research Article</u>	
4. Calculation of the Phase Diagrams (T – X and T – P) and the Thermodynamic Quantities for the Solid – Liquid Equilibria in n-tridecane	37-45
Ozlem Tari, Hamit Yurtseven	
<u>Review Article</u>	
5. Energy Structure Theory: A General Unified Thermodynamics Theory	47-62
Saeed Shahsavari, Seyed Mohammad Ali Boutorabi	

Research Article

Comparison Of The Electricity Generation Potentials Of Solar ORC Designed With Different Fluids Depending On Instantaneous Solar Radiation In Four Districts Of Türkiye

¹S. Yıldırım , ^{2*}S. Ata , ³H. Kurt , ⁴A. Kahraman 

¹ Necmettin Erbakan University, Graduate School of Natural and Applied Sciences, Department of Mechanical Engineering, Konya, Turkey

² KTO Karatay University, Faculty of Engineering and Natural Sciences, Department of Mechanical Engineering, Konya, Turkey

^{3,4} Necmettin Erbakan University, Faculty of Engineering, Department of Mechanical Engineering, Konya, Turkey
E-mail: ^{2*}sadik.ata@karatay.edu.tr

Received 15 February 2023, Revised 14 June 2023, Accepted 30 June 2023

Abstract

In this study, the solar Organic Rankine Cycle (ORC) system was analyzed to meet some of the electrical energy needed in large and medium-sized buildings and large enterprises such as hotels from solar energy. A simulation study was conducted for different districts in Türkiye that are rich in solar energy potential. These counties and the provinces they are affiliated with; Silifke-İçel, Alanya-Antalya, Bodrum-Muğla, Çeşme-İzmir. The power value transferred to the ORC was determined by considering the instantaneous radiation values and sunshine durations for the districts. The performance of solar ORC was determined by comparing fluids from three different organic fluid types. Organic fluids and types used in design; benzene-aromatic hydrocarbon, cyclohexane-alkane, octamethylcyclotetrasiloxane (D4)-siloxane. Considering the maximum electrical energy values obtained from Solar ORC in the summer months, it was seen that 205 MWh electricity generated was obtained for Silifke with benzene at a heat source temperature of 223 °C in July. Maximum solar parabolic trough collector (PTC) specific electric power value was determined as 59.52 W/m² in Alanya district with benzene in June. When the four districts are evaluated together, it has been determined that benzene performs better than cyclohexane by 3.8% on average and 23% better than D4. When the annual electrical energy values are examined, the highest production was determined as 1625 MWh with benzene fluid in Alanya district.

Keywords: Annual-monthly produced electricity; organic fluid; solar-organic rankine cycle (ORC); solar energy potential; different district in Turkey.

1. Aims and Scope

Photovoltaic (PV) panels, which are the most common and practical method of generating power from solar energy, may not be economically advantageous due to their low efficiency and problems such as storage. For this reason, it has been sought to find different methods and new technologies to benefit from solar energy. One of these technologies is the solar-powered Organic Rankine Cycle (ORC) systems, which is a method of producing heat and power efficiently from solar energy. It has been shown in some studies that generating power with the solar ORC system is more economical than PV systems alone, and hybrid power plants created by integrating these two systems will be more efficient [1-3].

In this study, the electricity generation potential of ORC was investigated by conducting a thermodynamic simulation study to meet the electrical energy needed in large enterprises such as hotels with solar ORC. In the calculations, in order to benefit more from solar energy, settlements with intense summer tourism were preferred. Because businesses such as hotels used in summer tourism

are actively used in periods when the solar radiation value is high and the demand for electrical energy is higher in these months. For this reason, it is hoped that this research will be an encouraging study in order to increase the energy demand from renewable energy in settlements where the amount of sunshine is high. Studies on the subject in the literature are summarized below.

Jahangir et al. [1] conducted a study on the solar-powered ORC hybrid power plant with a capacity of 80 kW, which will meet the energy needs of 20 families in a city of Iran. The feasibility of this solar-powered ORC system has been made using the exergy and exergoeconomic method. They found that the hybrid ORC-PV system is more economical than the ORC system alone. Kutlu et al. [2], the power generation of an innovative solar energy system combined with a vacuum planar solar collector and amorphous PV cells with ORC was investigated and compared with power systems in different situations. The necessary analyzes for these systems were made in Istanbul according to the hourly solar radiation values in two different days. For July 26, the daily power generation of the innovative power generation

system integrated with ORC, which has a solar collector area of 550 m² in Istanbul, was calculated as 452.35 kWh.

Patil et al. [3] compared the technical and economic performances of a 50-kW solar-powered ORC power plant and a PV power plant. When compared with energy storage systems for the same region, it has been determined that the solar-powered ORC power plant is more advantageous than the PV power plant. The reduced energy cost of the solar-powered ORC system with 1029 m² parabolic trough collector (PTC) area and the working fluid of isobutane is calculated as \$0.19/kWh, and the 1742 m² PV system is calculated as \$0.26/kWh.

Cakici et al. [4] conducted a study on integrating a geothermal energy sourced supercritical regenerative ORC power plant with PTC. The solar radiation value was accepted as 800 W/m² as the design parameter and the effect of the solar collector area variation between 822 m² and 24675 m² on the system performance was investigated by considering 5 different organic fluids. R134a showed the best performance among organic fluids. It has been concluded that hybrid ORC power systems with geothermal and solar energy are more advantageous than the ORC power system based on geothermal energy alone.

Yang et al. [5] developed an innovative operating mode for the solar-powered ORC power plant producing 1 MWe of power to be stable and regular in one day. According to the data obtained, it was observed that ORC operating in stable mode within one day had a system efficiency of 4.2% higher than ORC operating in irregular condition due to variable solar radiation values. Ustaoglu et al. [6] stated that R141-b fluid showed preferable performance when evaluated in terms of collector and total system efficiency in solar regenerative ORC studies. With a collector area of 6318 m² and an instantaneous radiation value of 1000 W/m², a power output of 616.47 kW was obtained from the turbine.

Elakhdar et al. [7] investigated the effect of solar radiation intensity on cooling and power generation by conducting a study on ORC and ejector cooling system from a low temperature solar energy source for cooling and power generation. Approximately 20% higher cooling performance (COP) was obtained from R601a fluid compared to other fluids. It was concluded that the turbine expansion ratio increased the ejector cooling system efficiency at a high rate. Arteconi et al. [8] used a linear Fresnel collector (LFR) in a micro-scale and solar-powered ORC power plant. In their study, the surface area of the collector, which gives a heat output of 80 kW at a nominal radiation value of 900 W/m², was determined as 146 m². With this micro-scale ORC system, it has been determined that 4 to 6 houses of 100 m² can meet the heating, cooling and hot water needs.

Dragomir-Stanciu et al. [9] investigated the effect of condenser temperature on cycle efficiency in ORC based solar power systems. It was determined that the thermal efficiency increased by 24.76% for the R600 fluid and by 29.78% for the R134a fluid, as the temperature decreased from 25 °C to 10 °C. Petrollese et al. [10] analyzed the Ottana solar power plant located in Italy. The facility consists of 630 kW solar powered ORC and 400 kW concentrator photovoltaic (CPV) systems. Power was produced with ORC from the energy provided by 8592 m² linear Fresnel solar collector (LFR). MM fluid from the siloxanes group was preferred as the ORC working fluid. Although the ORC unit operates with a net efficiency of 20.3% under nominal conditions, it has been determined that the cycle is generally far from this efficiency at partial loads since the actual

operating conditions are dynamic. Therefore, a new control strategy has been developed to accurately predict the next day's ORC power output of the system, which is affected by the change in ambient temperature and solar radiation values, and to maximize production efficiency.

Roumpedakis et al. [11] conducted a study on evaluating many different scenarios including different fluid types and collector types related to solar-powered ORC for four different regions (Athens, Thessaloniki, Istanbul, and Cyprus) and finding the best scenario for each region. In order to minimize the payback period and maximize the exergy efficiency, multi-purpose genetic algorithm method and optimization technique were applied. The highest exergy efficiency of the system was obtained in Istanbul when the vacuum tube solar collector and R245fa fluid were used.

Atiz and Karakilcik [12] analyzed the system that generates power with ORC by utilizing solar energy throughout the year for Adana climate conditions. In this study, 10 m² planar and vacuum tube solar collectors were compared and isobutane was used as the fluid. According to the results obtained, it was noted that when vacuum tube solar collector was used, 350.8 MJ/month was produced with approximately 70% collector efficiency and 6.25% cycle efficiency in July, and the highest turbine inlet temperature was reached with 83.24 °C in this month. Yilmaz et al. [13] designed and analyzed a hybrid power plant using solar and wind energy. To obtain power from solar energy, ORC with a capacity of 195.9 kW, working with a vacuum tube solar collector and R744 working fluid, was preferred.

Cao et al. [14] analyzed a combined solar ORC plant producing cooling, heating, and power. The system has been studied in three different modes: low irradiation state (solar mode), high irradiation state (solar and storage mode) and no solar radiation (thermal storage depletion mode).

Atiz et al. [15] evaluated the performance of an integrated geothermal solar ORC system for hydrogen and power generation relative to n-pentane, n-hexane, n-butane and cyclohexane fluids. The ORC power system has been tested according to the hourly solar irradiance values on a clear and sunny day in July for the province of Manisa. According to the results obtained, the best performance was obtained with n-butane fluid with a flow rate of 0.4 kg/s.

Aghaziarati and Aghdam [16] proposed a solar ORC system integrated with a cascade cooling system to meet the heating, cooling and electricity needs of a four-storey hospital. The effects of different ORC fluids, solar radiation variation, different type of collector and ambient temperature variation were investigated. PTC as solar collector and cyclohexane as organic fluid gave the best results for this system. Mahmood and Al-Ansari [17] studied greenhouse production with renewable energy, which is an innovative and sustainable project. They determined that 1.03 MW electricity, 4.36 MW cooling load and 17.5-27.3 m³/day water production required by the greenhouse to grow plants throughout the year can be provided by the combined power system.

Desai et al. [18] proposed a solar-powered ORC system as a cheap and feasible project, which could be a solution to the energy and water problem. Among the five different fluids (cyclopentane, n-pentane, MM, isopentane and MDM) compared, cyclopentane was found to be the most suitable circulating fluid. The reduced electricity and freshwater generation cost of the 1 MWe power plant is £0.116/kWh and £1.13/m³ for a region in Chile, and £0.163/kWh and £1.62/m³ for a region in South Africa, respectively.

Ancona et al. [19] investigated the performance of low-GWP fluids (R1234yf, R1234ze(E), R1243zf, R513A, R515A) as an alternative to R134a in their micro-solar-ORC study. The performance of these fluids was found to be lower than R134a due to the small isentropic enthalpy drop in the turbine and high pump consumption. They found that while R134a met 39% of the family's electricity needs, it met 17.5% of R513A (best low-GWP fluid). However, they suggested examining the methods of increasing their performance due to their superior environmental properties.

Aryanfar et al. [20] performed the energy, exergy, and economic analysis of the PTC-ORC- vapor compression cycle combined system. They compared the performance of R245fa, R114, R600 and R142b. They found that the minimum exergy destruction occurred in R245fa, and the minimum cost in R114 (for 137 °C turbine inlet temperature) and R142b (for 2500 kPa turbine inlet pressure).

Mirjavadi et al. [21] compared the performance of Steam Rankine Cycle (SRC)-ORC and SRC-Kalina Cycle (KC) combinations under PTC heat source. Although the two systems have different sensitivities to turbine inlet and outlet pressure changes, they stated that the two systems are equal from an economic point of view. They determined that the leveled costs of energy for both systems were 0.011 \$/kWh. Rostami et al. [22] examined the production system with PTC, PEM fuel cell, ORC, alkaline electrolysis, and TEG unit. They found that 140.8 kW of thermal power was provided from PTC, resulting in 22.5 kW of electricity and 97.3 kg of hydrogen per hour.

Kara [23] studied recuperated ORC using toluene, cyclohexane, and isopentane with PTC using Therminol 66. It was determined that the efficiency increase with the decrease of the condenser temperature. With the hourly analysis carried out on January 15 and June 15, the thermal efficiency was determined as 29.97% and 28.08%, respectively. Pourmoghadam and Kasaeian [24] studied the solar multi-generation system with PTC heat source. They determined that the solar unit consisting of PTC collector and Phase Change Material (PCM) storage tank constitutes

60.5% of the total initial cost. They achieved the best performance with toluene fluid in ORC unit. The payback period of the system was determined as 6 years.

Khalid and Kumar [25] investigated the production of electricity, cooling, water and hydrogen by ORC and vapor compression refrigeration cycles with PTC as the heat source. They have reached 17.5% energy efficiency under 2000 m² PTC and 700 W/m² radiation. Alshammari et al. [26] investigated the radial turbine model in solar ORC with PTC. They found that an increase in evaporator pressure by 100 kPa resulted in a 17.5% decrease in turbine size. Kara [27] studied PTC solar and ground cooling performance in three different ORC configurations (basic, single-stage regenerative and double-stage regenerative). He compared the annual electricity production values in different regions of Turkey. They determined 4151, 3965, 3286 and 2847 kWh/years values for Antalya, Izmir, Istanbul and Trabzon, respectively.

In this study, the prominent fluids from three different fluid groups as a result of the literature research were compared. For aromatic hydrocarbons, Yagli et al. [28], Vaja and Gambarotta [29], Carcasci et al. [30], Herath et al. [31] suggested benzene; for alkanes, Tzivanidis et al. [32], Song and Gu [33], Xu et al. [34] cyclohexane; for siloxanes, Uusitalo et al. [35], Delgado-Torres and García-Rodríguez [36], Liang et al. [37] D4 fluid in their study. Therefore, in this study, it is aimed to determine the performance of these three fluids in the solar-ORC configuration.

When the literature studies are examined, no study has been found that determines the annual electricity energy that can be produced for Turkey, which has a significant solar energy potential, by considering the instantaneous radiation value and sunshine duration of the region with the solar ORC system designed with different fluids. Since this electrical energy to be produced changes depending on the organic fluid, it has been seen that both the solar capacity of the region and the thermophysical state of the organic fluid should be examined together.

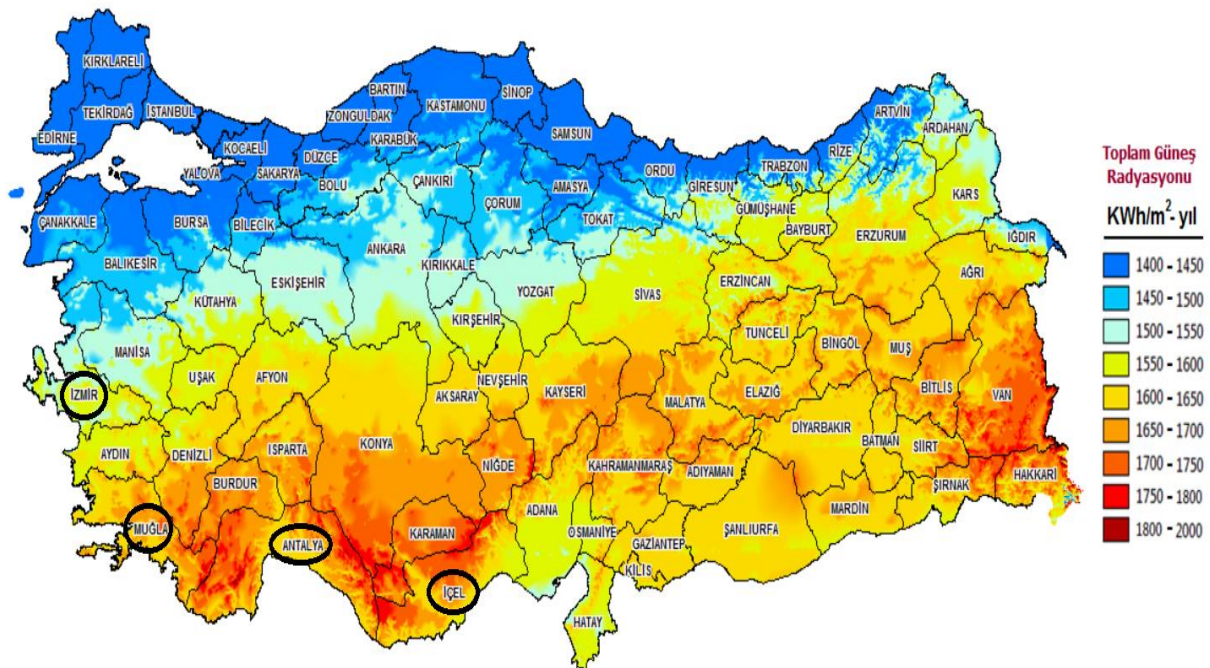


Figure 1. Turkey's Solar Energy Potential Atlas (The provinces of the examined districts are shown on the map)[38].

In this study, it is discussed that some of the electrical energy needed in large and medium-sized buildings and large enterprises such as hotels is met from solar energy. By using 3 different organic fluids in the ORC power system, 4 different districts rich in solar energy potential were simulated and the electricity generation potential of ORC was examined.

These counties and the provinces they are affiliated with; Silifke-İçel, Alanya-Antalya, Bodrum-Muğla, Çeşme-İzmir. Turkey's solar energy potential atlas and the provinces of the examined districts are given in Figure 1.

The performance of different types of organic fluids was determined in the Solar ORC system. Organic fluids and types used in design; benzene-aromatic hydrocarbon, cyclohexane-alkane, D4-siloxane.

Solar ORC was simulated with Engineering Equation Solver (EES). A solar-ORC system has been simulated that can generate 175-200 MWh of electrical energy per month and 1250-1650 MWh of electrical energy annually during the summer months.

2. Materials and Methods

In Figure 2, the working principle of the solar ORC system is given. A fluid from three different organic fluid groups was used in the design. T-s diagrams of organic fluids are given in Figure 3. The thermophysical and environmental properties of the fluids are given in Table 1. It is seen that benzene and cyclohexane are close to each other at critical temperature values, while D4 has a higher critical temperature. All three fluids are in the dry fluid category and D4 has more molecular weight and boiling point temperature. It is seen that benzene and cyclohexane show closer properties in terms of thermophysical properties. When the safety values are examined according to the National Fire Protection Association (NFPA) classification, it is seen that cyclohexane is better for health hazard.

Solar ORC simulation was done with EES. ORC thermodynamic analysis and solar collector calculations are given below Eqs. (1)-(17). Characteristics of the IST PTC system are given in Table 2.

Mass and Energy Balance [43];

$$\sum_i \dot{m}_{in} = \sum_i \dot{m}_{out} \quad (1)$$

$$(q_{in} - q_{out}) + (w_{in} - w_{out}) = 0 \quad (2)$$

Turbine and Pump;

$$\eta_t = \frac{(h_3 - h_4)}{(h_3 - h_{4s})} \quad (3)$$

$$\eta_p = \frac{(h_{2s} - h_1)}{(h_2 - h_1)} \quad (4)$$

$$W_t = \dot{m}_{ORC} x (h_3 - h_{4s}) * \eta_t \quad (5)$$

$$W_p = \dot{m}_{ORC} x (h_{2s} - h_1) / \eta_p \quad (6)$$

Evaporator and Condenser-Pinch Point Analysis;

$$\Delta T_{pp,e} = T_{p,e} - T_{3,f} \quad (7)$$

$$\Delta T_{pp,c} = T_{1,g} - T_{p,c} \quad (8)$$

$$Q_c = \dot{m}_{ORC} x (h_4 - h_1) \quad (9)$$

$$Q_e = \dot{m}_{ORC} x (h_3 - h_2) = \dot{m}_{solar} x (h_{h,i} - h_{h,o}) \quad (10)$$

Solar Collector Analysis [32];

$$\eta_c = \alpha_0 - \alpha_1 * \frac{T_{h,i} - T_0}{G} - \alpha_2 * \frac{(T_{h,i} - T_0)^2}{G} \quad (11)$$

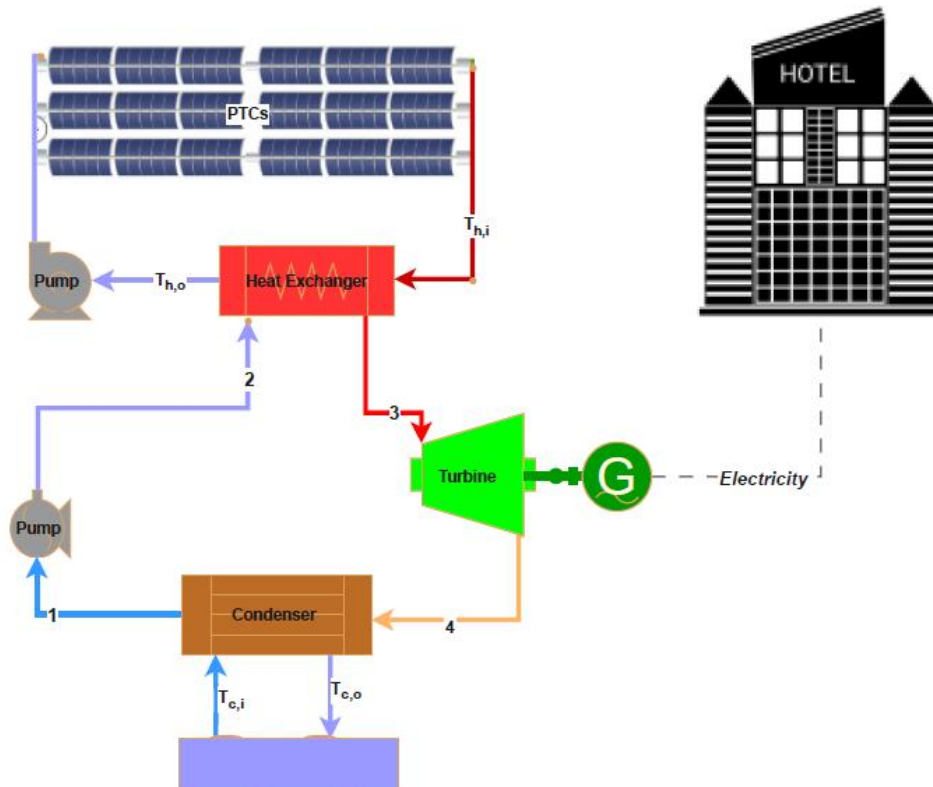


Figure 2. Solar ORC Working Principle.

Table 1. Thermophysical properties of fluids [36,39-41].

Properties/Fluid	Benzene	Cyclohexane	D4
Fluid Group	Aromatic Hydrocarbon	Alkane	Siloxane
Fluid Type	Dry	Dry	Dry
Molecular structure	C ₆ H ₆	C ₆ H ₁₂	C ₈ H ₂₄ O ₄ Si ₄
CAS Number	71-43-2	110-82-7	556-67-2
Critical Temperature (°C)	288.9	280.5	313.3
Critical Pressure (kPa)	4.89	4.081	1.332
Molecular Weight (kg/kmol)	78.11	84.16	296.6
Boiling Point (°C)	80.2	80.9	175.35
Melting Point (°C)	6.8	6.5	17
Flash Point (°C)	-11	-18	51
Autoignition Temperature (°C)	498	260	400
Specific Gravity	0.95	0.77	0.956
*Health	3	1	2
*Flammability	3	3	2
*Instability	0	0	0
GWP	3-4	4-6	n.a

* Safety information according to NFPA classification

For health hazard; 0: Normal Material; 1: Slightly Hazardous; 2: Hazardous; 3: Extreme Danger; 4: Danger.

For fire hazard; 0: Will not burn; 1: Above 93.33 °C; 2: Below 93.33 °C; 3: Below 37.78 °C; 4: Below 22.77 °C.

For instability hazard; 0: Stable; 1: Unstable if heated; 2: Violent chemical change; 3: Shock and heat may detonate; 4: May detonate.

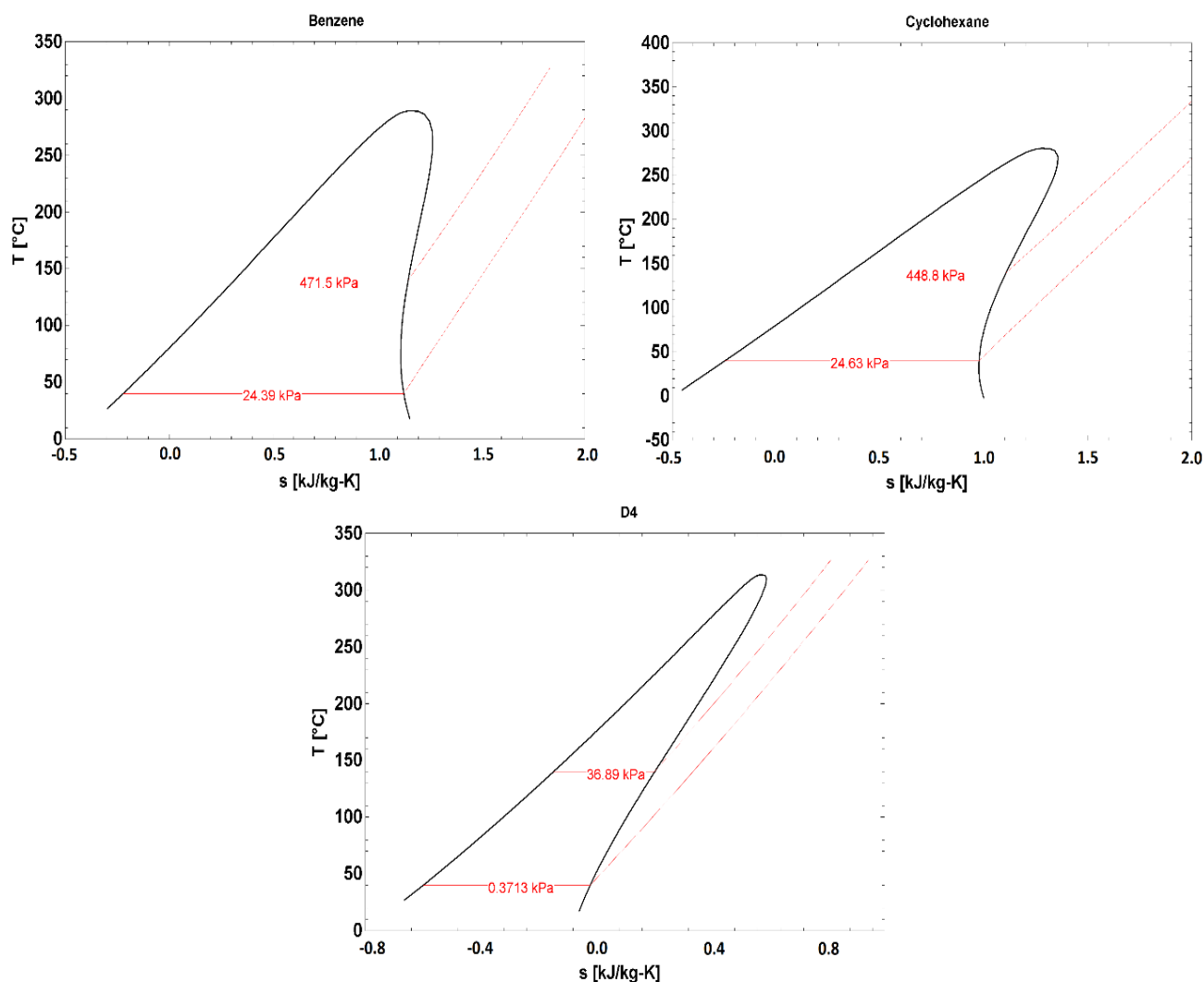


Figure 3. T-s diagrams of organic fluids used in design with evaporating and condensing pressure (Benzene, cyclohexane and D4)[42].

Table 2. Characteristics of the IST PTC system [32,44].

Efficiency Coefficient α_0	0.762
First Heat Loss Coefficient α_1 (W/m ² K)	0.2125
Second Heat Loss Coefficient α_2 (W/m ² K)	0.001672

$$Q_e = G \times A_c \times \eta_c = \dot{m}_{solar} \times (h_{h,i} - h_{h,o}) \quad (12)$$

To calculate the year-round power generation of this ORC system locally under variable solar irradiance values, daily global irradiance intensity values, averaged over months, were used. Accordingly, the average instantaneous

radiation values for each month were obtained as in Equation 13.

$$G = (E_g/t_g) \times 1000 \quad (13)$$

Here, E_g shows the average daily solar irradiation intensity (kWh/m²-day) in a month, t_g shows the daily sunshine duration (hours/day) in the same month. In the calculations, the average G value of each month was used as W/m².

The average daily solar radiation intensity values (a) and sunshine durations (b) for four districts in Turkey are given in Figure 4-7. Calculations of instantaneous radiation values for four districts are also shown in Table 3-6.

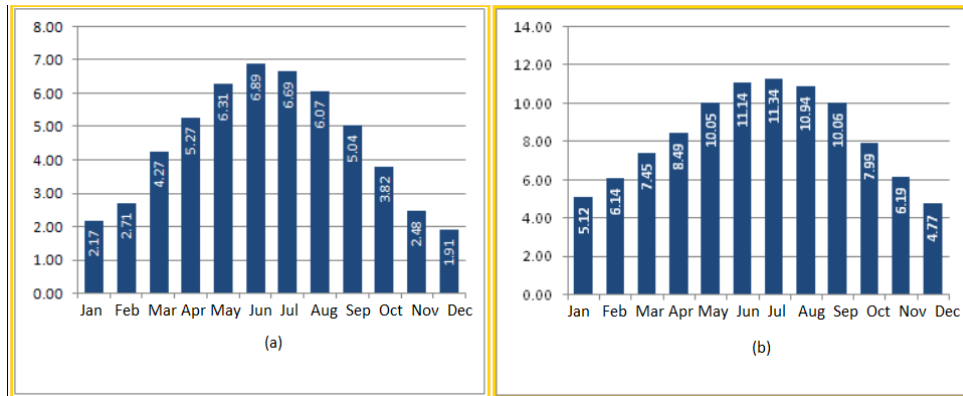


Figure 4. Average daily solar radiation intensity values for Silifke-kWh/m²-day (a) and sunshine duration-hour (b) [38].

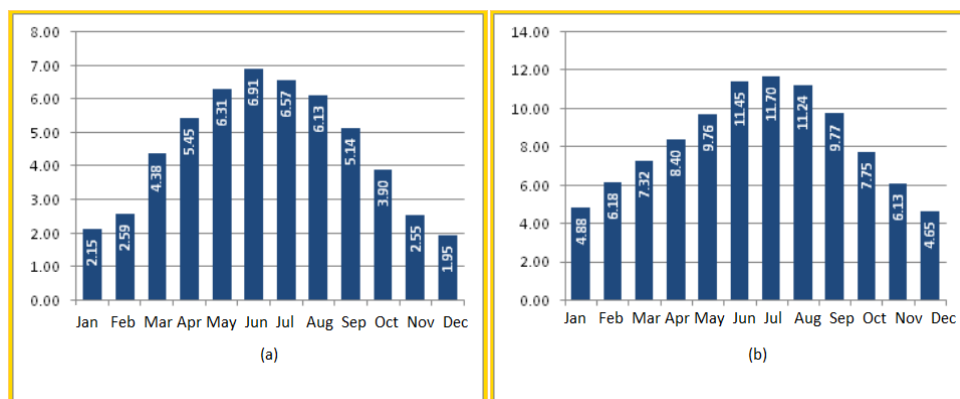


Figure 5. Average daily solar radiation intensity values for Alanya-kWh/m²-day (a) and sunshine duration-hour (b) [38].

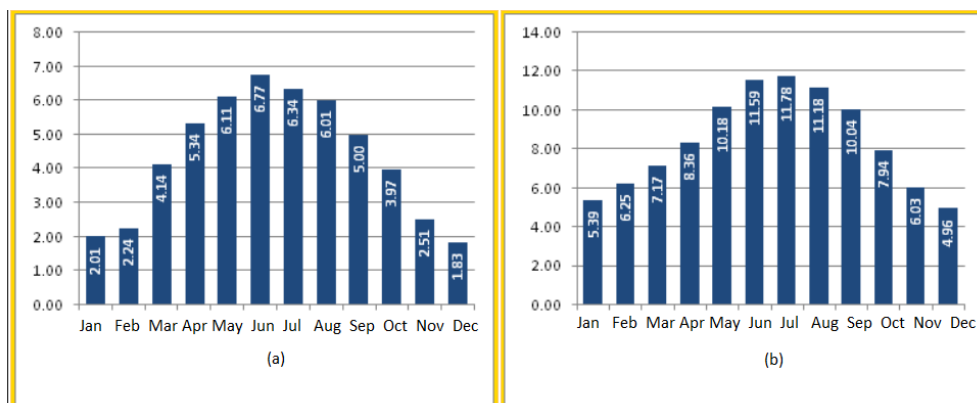


Figure 6. Average daily solar radiation intensity values for Bodrum-kWh/m²-day (a) and sunshine duration-hour (b) [38].

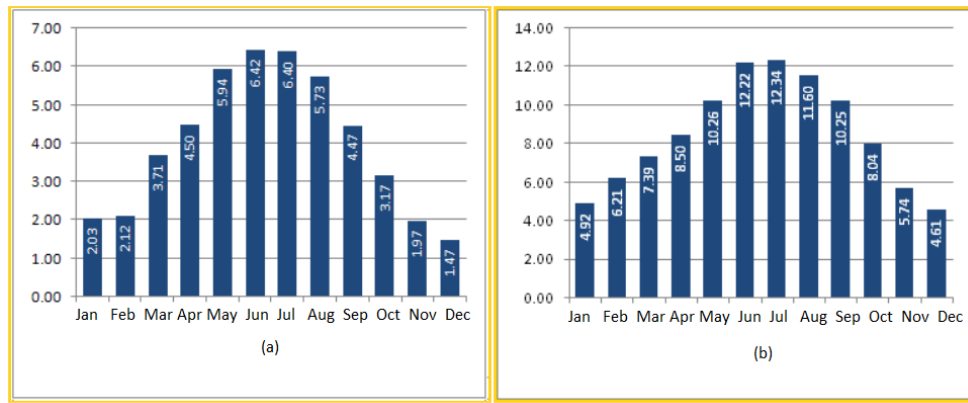


Figure 7. Average daily solar radiation intensity values for Çeşme-kWh/m²-day (a) and sunshine duration-hour (b) [38].

Table 3. Average instantaneous radiation values for Silifke.

SİLİFKE	Jan	Feb	Mar	Apr	May	Jun	Jul	Aug	Sep	Oct	Nov	Dec
Average Sunbathing Time t_g [hour/day]	5.12	6.14	7.45	8.49	10.05	11.14	11.34	10.94	10.06	7.99	6.19	4.77
Monthly Average Irradiation values E_g (kWh/m ² -day)	2.17	2.71	4.27	5.27	6.31	6.89	6.69	6.07	5.04	3.82	2.48	1.91
Instant average radiation value $G = (E_g/t_g) * 1000$ [W/m ²]	424	441	573	621	628	618	590	555	501	478	401	400

Table 4. Average instantaneous radiation values for Alanya.

ALANYA	Jan	Feb	Mar	Apr	May	Jun	Jul	Aug	Sep	Oct	Nov	Dec
Average Sunbathing Time t_g [hour/day]	4.9	6.2	7.3	8.4	9.8	11.5	11.7	11.2	9.8	7.8	6.1	4.7
Monthly Average Irradiation values E_g (kWh/m ² -day)	2.2	2.6	4.4	5.5	6.3	6.9	6.6	6.1	5.1	3.9	2.6	2.0
Instant average radiation value $G = (E_g/t_g) * 1000$ [W/m ²]	441	419	598	649	647	603	562	545	526	503	416	419

Table 5. Average instantaneous radiation values for Bodrum.

BODRUM	Jan	Feb	Mar	Apr	May	Jun	Jul	Aug	Sep	Oct	Nov	Dec
Average Sunbathing Time t_g [hour/day]	5.39	6.25	7.17	8.36	10.18	11.59	11.78	11.18	10.04	7.94	6.03	4.96
Monthly Average Irradiation values E_g (kWh/m ² -day)	2.01	2.24	4.14	5.34	6.11	6.77	6.34	6.01	5	3.97	2.51	1.83
Instant average radiation value $G = (E_g/t_g) * 1000$ [W/m ²]	373	358	577	639	600	584	538	538	498	500	416	369

Table 6. Average instantaneous radiation values for Çeşme.

ÇEŞME	Jan	Feb	Mar	Apr	May	Jun	Jul	Aug	Sep	Oct	Nov	Dec
Average Sunbathing Time t_g [hour/day]	4.92	6.21	7.39	8.5	10.26	12.22	12.34	11.6	10.25	8.04	5.74	4.61
Monthly Average Irradiation values E_g (kWh/m ² -day)	2.03	2.12	3.71	4.5	5.94	6.42	6.4	5.73	4.47	3.17	1.97	1.47
Instant average radiation value $G = (E_g/t_g) * 1000$ [W/m ²]	413	341	502	529	579	525	519	494	436	394	343	319

Net Power and Efficiency;

$$\eta_{ORC} = W_{net}/\dot{Q}_e \quad (15)$$

$$W_{net} = W_t - W_p$$

$$(14) \quad \text{Solar System Efficiency;}$$

$$\eta_{solar} = \eta_{ORC} \times \eta_c \quad (16)$$

Power supplied from solar energy and produced per square meter of solar collector area- Specific Power-Collector (SPc);

$$SP_c = \eta_{solar} \times G \text{ [W/m}^2\text{]} \quad (17)$$

Design values are given in Table 7. The assumptions made in thermodynamic analysis; steady state process, heat exchangers, turbine, and pump adiabatic, kinetic, and potential energy changes are neglected. Solar collector efficiency is assumed to be unaffected by ambient temperature. Turbine, pump, generator, and solar collector efficiencies are assumed constant over all operating ranges. Pressure losses and friction in heat exchangers and pipes has been neglecting.

Table 7. Design values for Solar-ORC.

Parameter	Value	Unit
Expander efficiency [45]	0.7	-
Pump efficiency [45]	0.7	-
Evaporating temperature [45]	140	°C
Evaporator pinch point temperature difference [46]	20	°C
Condenser pinch point temperature difference [47]	5	°C
Cooling water temperature difference [47]	5	°C
Ambient temperature	25	°C
Ambient pressure	101	kPa
Solar mass flow rate	10	kg/s
Collector Area [48-49]	10000	m ²

3. Result and Discussion

In this section, simulation results of monthly electricity production values of solar ORC designed using three different organic fluids are presented.

Considering the thermophysical properties of organic fluids, it is seen that the heat input per unit mass (enthalpy difference) is less in D4 fluid than in the others. Therefore, the required flow rate for D4 is higher at the same evaporator capacity.

Under the same evaporator capacity, the highest power was obtained in the benzene fluid, although the heat input per unit mass was higher and the flow rate was lower than the others.

Despite the low flow rate in the benzene fluid, the turbine power was found to be higher due to the high enthalpy drop in the turbine. The fact that the pump work was more than D4 also did not affect the net power. Therefore, the net power order was determined as benzene>cyclohexane>D4.

In Figure 8, monthly electricity generated for Silifke district is given. Unlike Alanya district, the highest production value was realized in July, albeit with a small difference. In July, 205 MWh was obtained with benzene, 197 MWh with cyclohexane, and 165 MWh with D4. It was determined that a maximum power of 619 kW was obtained with benzene, while a power of 596 kW was obtained with cyclohexane. When ORC mass flow rates are examined, it is noteworthy that D4 has a mass flow rate of 75% more than

other fluids. Maximum performance (205 MWh/month) for Silifke was reached in July under 589.9 W/m² radiation and 11.34 h sunbathing time. Under these conditions, the evaporator capacity was determined as 4130 kW (Table 8).

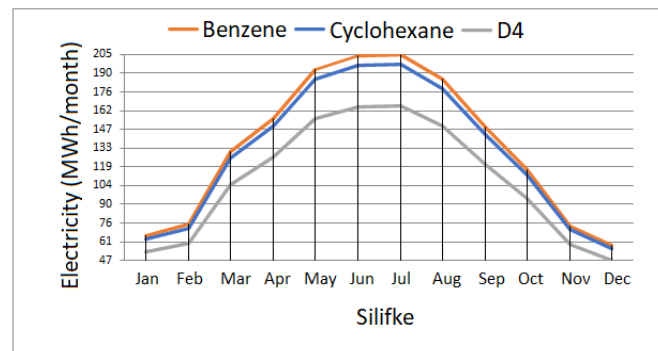


Figure 8. Distribution of electrical energy (MWh) produced by months when three different fluids are used for Silifke.

In Figure 9, monthly electricity generation for Alanya district is given. The highest production values were realized in June. In June, 204 MWh was obtained with benzene, 196 MWh with cyclohexane, and 165 MWh with D4. It was determined that maximum 638 kW power was obtained with benzene, while 614 kW power was obtained with cyclohexane. It was determined that while higher power was obtained with benzene, the mass flow rate required for ORC was also less than cyclohexane. While it is 7.83 kg/s for benzene, it is 8.01 kg/s for cyclohexane for July. Maximum performance (204 MWh/month) for Alanya was reached in June under 603.5 W/m² radiation and 11.45 hour/day sunbathing time. Under these conditions, the evaporator capacity was determined as 4224 kW. (Table 9).

When Table 8 and Table 9 are examined for the benzene fluid with maximum performance;

In June, more net power was obtained in Silifke than in Alanya due to the higher radiation, consequently higher evaporator capacity, under same evaporation-condensing temperature. However, when the electricity produced by taking into account the sunshine durations is compared, it is seen that Alanya is more.

In July, although the radiation, accordingly evaporator capacity, for both districts decreased and the sunshine duration increased, the produced electricity in Silifke increased while it decreased in Alanya. Although the rate of increase in sunshine durations is close, the produced electricity in Silifke increased in July as the radiation decreased to a lesser extent.

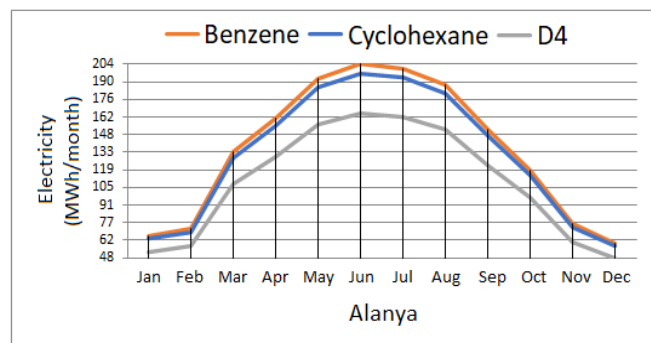


Figure 9. Distribution of electrical energy (MWh) produced by months when three different fluids are used for Alanya.

Table 8. Monthly average power (kW) and energy amounts (MWh) produced with ORC when different circulation fluids are used for Silifke in summer.

Organic Fluids	Month	Day Number	Sunbathing Time (hour/day)	G (W/m ²)	\dot{m}_{ORC} (kg/s)	$T_{h,i}$ (°C)	$W_{net,ave}$ (kW)	Electricity (MWh/month)
Benzene	May	31	10.05	627.9	8.15	227	619.3	192.94
	June	30	11.14	618.5	8.03	226	610.0	203.86
	July	31	11.34	589.9	7.66	223	581.9	204.56
	August	31	10.94	554.8	7.20	220	547.3	185.61
Cyclohexane	May	31	10.05	627.9	8.33	221	596.3	185.78
	June	30	11.14	618.5	8.21	221	587.4	196.31
	July	31	11.34	589.9	7.83	218	560.3	196.97
	August	31	10.94	554.8	7.36	214	527.0	178.73
D4	May	31	10.05	627.9	14.24	209	500.3	155.87
	June	30	11.14	618.5	14.02	209	492.9	164.73
	July	31	11.34	589.9	13.38	206	470.1	165.26
	August	31	10.94	554.8	12.58	204	442.1	149.93

Table 9. Monthly average power (kW) and energy amounts (MWh) produced with ORC when different circulation fluids are used for Alanya in summer.

Organic Fluids	Month	Day Number	Sunbathing Time (hour/day)	G (W/m ²)	\dot{m}_{ORC} (kg/s)	$T_{h,i}$ (°C)	$W_{net,ave}$ (kW)	Electricity (MWh/month)
Benzene	May	31	9.76	646.50	8.39	229.30	637.70	192.94
	June	30	11.45	603.50	7.83	224.70	595.20	204.45
	July	31	11.70	561.50	7.29	220.20	553.90	200.90
	August	31	11.24	545.40	7.08	218.40	537.90	187.43
Cyclohexane	May	31	9.76	646.50	8.58	223.30	614.00	185.77
	June	30	11.45	603.50	8.01	219.10	573.20	196.89
	July	31	11.70	561.50	7.45	214.90	533.30	193.43
	August	31	11.24	545.40	7.24	213.40	518.00	180.49
D4	May	31	9.76	646.50	14.66	210.80	515.20	155.88
	June	30	11.45	603.50	13.68	207.40	480.90	165.19
	July	31	11.70	561.50	12.73	204.10	447.50	162.31
	August	31	11.24	545.40	12.37	202.80	434.60	151.43

In Figure 10, monthly electricity generation for Bodrum district is given. The highest production values were realized in June. Unlike Alanya and Silifke, there is a difference of approximately 7 MWh between the electricity produced in June and July. In June, 200 MWh was obtained with benzene, 192 MWh with cyclohexane, and 161 MWh with D4. It was determined that a maximum power of 592 kW was obtained with benzene, while a power of 570 kW was obtained with cyclohexane. Although the mass flow rates of benzene and cyclohexane are close, the required flow rate for benzene is lower.

Maximum performance (200 MWh/month) for Bodrum was reached in June under 584.1 W/m² radiation and 11.59 sunbathing time. Under these conditions, the evaporator capacity was determined as 4089 kW. (Table 10).

In Figure 11, monthly electricity generated for Çeşme district is given. The highest production values were realized in July. While there was an overproduction of 7 MWh in Bodrum in June, it was observed that there was an excess of 6 MWh in July in Çeşme. In July, 195 MWh was obtained with benzene, 188 MWh with cyclohexane, and 158 MWh with D4. It was determined that a maximum power of 571 kW was obtained with benzene, while a power of 549 kW

was obtained with cyclohexane. Maximum performance (196 MWh/month) for Çeşme was reached in July under 518.6 W/m² radiation and 12.34 sunbathing time. Under these conditions, the evaporator capacity was determined as 3630 kW (Table 11).

When all districts were examined, the best performance was obtained in benzene fluid under the same evaporator capacity.

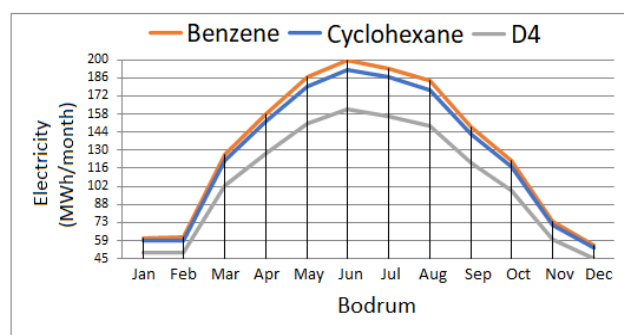


Figure 10. Distribution of electrical energy (MWh) produced by months when three different fluids are used for Bodrum.

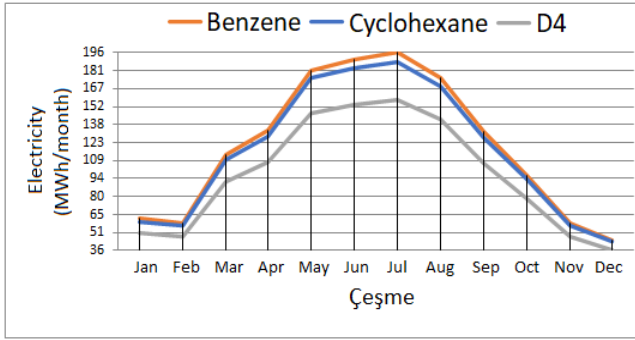


Figure 11. Distribution of electrical energy (MWh) produced by months when three different fluids are used for Çeşme.

It has been observed that the benzene fluid achieves the best performance in different districts. The purpose of comparison in different districts is to examine the effect of radiation and sunbathing time on net power and monthly electricity produced. It is seen that the energy transferred to the evaporator due to the high radiation is high for Silifke. In the same evaporation-condensation temperature conditions, the system mass flow rate was higher, so more net power generation was realized. On the other hand, the monthly

electricity produced was determined by considering the sunbathing time. If we examine the districts of Bodrum and Çeşme; although the net power in Bodrum is higher than Çeşme, the monthly electricity produced is less. Although the radiation of Bodrum is 3.77% more than Çeşme, it is seen that the sunbathing time is 4.538% less. This also affected the amount of electricity produced. Solar data and analysis results of four districts are given in Table 12.

In Figure 12, annual electricity values for four districts are compared. Although more electricity is produced in Silifke than Alanya in July with benzene fluid, it is approximately 13 MWh electricity generated less in annual production. While the annual average radiation value is 519 W/m² in Silifke, it is 527 W/m² in Alanya. The average of sunbathing time is 8.30 and 8.26 hour/day for Silifke and Alanya, respectively. Despite the longer sunbathing time, the decrease in radiation value in Silifke resulted in less electricity production in annual production. The highest annual production was realized in Alanya with 1625 MWh electricity generated. It is seen that the performance order of the fluids is benzene>cyclohexane>D4. When the four districts are evaluated together, it has been determined that benzene performs better than cyclohexane by 3.8% on average and 23% better than D4.

Table 10. Monthly average power (kW) and energy amounts (MWh) produced with ORC when different circulation fluids are used for Bodrum in summer.

Organic Fluids	Month	Day Number	Sunbathing Time (hour/day)	G (W/m ²)	\dot{m}_{ORC} (kg/s)	T _{h,i} (°C)	W _{net,ave} (kW)	Electricity (MWh/month)
Benzene	May	31	10.18	600.2	7.79	224	592.0	186.82
	June	30	11.59	584.1	7.58	223	576.1	200.31
	July	31	11.78	538.2	6.99	218	530.8	193.84
	August	31	11.18	537.6	6.98	218	530.2	183.76
Cyclohexane	May	31	10.18	600.2	7.96	219	570.0	179.88
	June	30	11.59	584.1	7.75	217	554.8	192.90
	July	31	11.78	538.2	7.14	213	511.2	186.68
	August	31	11.18	537.6	7.13	213	510.6	176.96
D4	May	31	10.18	600.2	13.61	207	478.3	150.94
	June	30	11.59	584.1	13.24	206	465.5	161.85
	July	31	11.78	538.2	12.20	202	428.9	156.63
	August	31	11.18	537.6	12.19	202	428.4	148.47

Table 11. Monthly average power (kW) and energy amounts (MWh) produced with ORC when different circulation fluids are used for Çeşme in summer.

Organic Fluids	Month	Day Number	Sunbathing Time (hour/day)	G (W/m ²)	\dot{m}_{ORC} (kg/s)	T _{h,i} (°C)	W _{net,ave} (kW)	Electricity (MWh/month)
Benzene	May	31	10.26	578.9	7.52	222	571.0	181.61
	June	30	12.22	525.4	6.82	216	518.2	189.97
	July	31	12.34	518.6	6.73	216	511.5	195.67
	August	31	11.60	494.0	6.41	213	487.2	175.20
Cyclohexane	May	31	10.26	578.9	7.68	217	549.9	174.90
	June	30	12.22	525.4	6.97	211	499.0	182.93
	July	31	12.34	518.6	6.88	211	492.6	188.44
	August	31	11.60	494.0	6.55	208	469.2	168.72
D4	May	31	10.26	578.9	13.13	206	461.4	146.75
	June	30	12.22	525.4	11.91	201	418.7	153.50
	July	31	12.34	518.6	11.76	201	413.3	158.10
	August	31	11.60	494.0	11.20	199	393.6	141.54

Table 12. Comparison of net power and amount of electricity produced in different districts of benzene fluid in July with evaporator capacity.

District	G (W/m^2)	Sunbathing Time (hour/day)	$W_{net,ave}$ (kW)	Electricity (MWh/month)	Q_{evap} (kW)
Silifke	589.9	11.34	581.9	204.561	4130
Alanya	561.5	11.7	553.9	200.900	3931
Bodrum	538.2	11.78	530.8	193.838	3767
Çeşme	518.6	12.34	511.5	195.669	3630

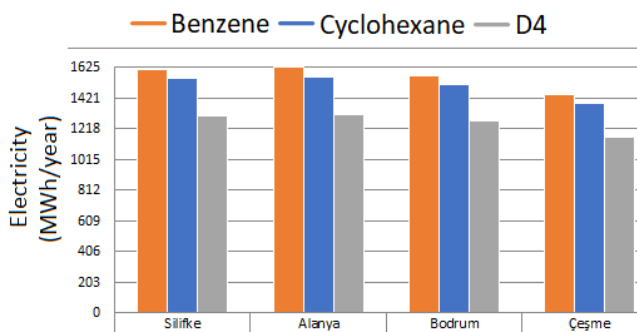


Figure 12. Annual total electricity energy production amounts (MWh) of the ORC system for four different districts with different fluids.

4. Conclusions

In this study, the potential of solar ORC designed using three different organic fluids (benzene, cyclohexane and D4) to meet some of the electricity needs of a building or hotel was analyzed. A simulation study was carried out considering the solar radiation value and sunshine duration of 4 different districts in Turkey (Silifke-İçel, Alanya-Antalya, Bodrum-Muğla, Çeşme-İzmir).

When the maximum electrical energy values obtained in the summer months are examined;

For Silifke, 205 MWh electricity generated was obtained with benzene at a heat source temperature of 223 °C in July. It has been determined that the mass flow rate for ORC should be 8.03 kg/s and the evaporator capacity is 4130 kW. The specific electric power value of the solar collector is 58.19 W/m^2 .

For Alanya, 204 MWh electricity generated was obtained with benzene at a heat source temperature of 224 °C in June. It has been determined that the mass flow rate for ORC should be 7.83 kg/s and the evaporator capacity is 4224 kW. The specific electric power value of the solar collector is 59.52 W/m^2 .

For Bodrum, 200 MWh electricity generated was obtained with benzene at a heat source temperature of 223 °C in June. It has been determined that the mass flow rate for ORC should be 7.58 kg/s and the evaporator capacity is 4089 kW. The specific electric power value of the solar collector is 57.61 W/m^2 .

For Çeşme, 196 MWh electricity generated was obtained with benzene at 216 °C heat source temperature in July. It has been determined that the mass flow rate for ORC should be 6.73 kg/s and the evaporator capacity is 3630 kW. The specific electric power value of the solar collector is 51.15 W/m^2 .

Similar results were obtained in Silifke and Alanya districts. Although Alanya is better than Silifke in the specific electrical power value of the solar collector,

Silifke is in a better situation in terms of maximum electrical energy.

In each district, the best results were obtained with benzene fluid. Although the performance of benzene and cyclohexane is close to each other, there is a serious performance difference between benzene and D4.

When the annual electrical energy values are examined, the highest production was determined as 1625 MWh electricity generated with benzene fluid in Alanya district. Annual generated electrical energy values are listed below.

- Alanya;benzene-1625 MWh>cyclohexane-1564 MWh>D4-1313 MWh;
- Silifke;benzene-1612 MWh> cyclohexane-1553 MWh>D4-1303 MWh;
- Bodrum;benzene-1572 MWh> cyclohexane-1514 MWh>D4-1270 MWh;
- Çeşme;benzene-1442 MWh> cyclohexane-1389 MWh>D4-1165 MWh

As a continuation of the study, it is proposed to determine the payback period and the saved carbon dioxide emissions by performing thermo-economic and enviro-economic analysis.

Acknowledgement

This study includes a part of Serhat Yıldırım's master's thesis.

Nomenclature

A_c	: Collector Area (m^2)
E_g	: Daily solar irradiation intensity (kWh/m^2 -day)
EES	: Engineering Equation Solver
G	: Instantaneous radiation (W/m^2)
GWP	: Global Warming Potential
IST	: Industrial Solar Technology
h	: Enthalpy (kJ/kg)
\dot{m}	: Mass Flow Rate (kg/s)
ORC	: Organic Rankine Cycle
PTC	: Parabolic Trough Collector
PV	: Photovoltaic
\dot{Q}	: Heat Flow (kW)

t_g	: Daily sunshine duration (hours/day)
T	: Temperature (°C)
T_0	: Ambient Temperature
\dot{W}	: Power (kW)

Greek letters

η_c	: collector efficiency (%)
η_{ORC}	: thermal efficiency (%)
η_p	: pump isentropic efficiency (%)
η_t	: turbine isentropic efficiency (%)
η_{solar}	: solar system efficiency (%)
Δ	: difference

Subscripts

0	: ambient condition
$1,2,3,..$: state point
c	: condenser
e	: evaporator
in	: inlet of each component
p	: pump
out	: out of each component
t	: turbine

References


- [1] M.H. Jahangir, S.A. Mousavi, M. Amin, V. Rad, "A techno-economic comparison of a photovoltaic / thermal organic Rankine cycle with several renewable hybrid systems for a residential area in Rayen, Iran," *Energy Convers. Manag.*, 195, 244-261, 2019, doi:10.1016/j.enconman.2019.05.010.
- [2] C. Kutlu, J. Li, Y. Su, Y. Wang, G. Pei, S. Riffat, "Investigation of an innovative PV/T-ORC system using amorphous silicon cells and evacuated flat plate solar collectors," *Energy*, 203, 117873, 2020, doi:10.1016/j.energy.2020.117873.
- [3] V.R. Patil, V.I. Biradar, R. Shreyas, P. Garg, M.S. Orosz, N.C. Thirumalai, "Techno-economic comparison of solar organic Rankine cycle (ORC) and photovoltaic (PV) systems with energy storage," *Renew. Energy*, 113, 1250-1260, 2017, doi:10.1016/j.renene.2017.06.107.
- [4] D.M. Cakici, A. Erdogan, C.O. Colpan, "Thermodynamic performance assessment of an integrated geothermal powered supercritical regenerative organic Rankine cycle and parabolic trough solar collectors," *Energy*, 120, 306-319, 2017, doi:10.1016/j.energy.2016.11.083.
- [5] J. Yang, J. Li, Z. Yang, Y. Duan, "Thermodynamic analysis and optimization of a solar organic Rankine cycle operating with stable output," *Energy Convers. Manag.*, 187, 459-471, 2019, doi:10.1016/j.enconman.2019.03.021.
- [6] A. Ustaoglu, J. Okajima, X. Zhang, S. Maruyama, "Assessment of a solar energy powered regenerative organic Rankine cycle using compound parabolic involute concentrator," *Energy Convers. Manag.*, 184, 661-670, 2019, doi:10.1016/j.enconman.2019.01.079.
- [7] M. Elakhdar, H. Landoulsi, B. Tashtoush, E. Nehdi, L. Kairouani, "A combined thermal system of ejector refrigeration and Organic Rankine cycles for power generation using a solar parabolic trough," *Energy Convers. Manag.*, 199, 111947, 2019, doi:10.1016/j.enconman.2019.111947.
- [8] A. Arteconi, L. Del Zotto, R. Tascioni, K. Mahkamov, C. Underwood, L.F. Cabeza, J.M. Maldonado, R. Manca, A.C. Mintsas, C.M. Bartolini, T. Gimbernat, T. Botargues, E. Halimic, L. Cioccolanti, "Multi-country analysis on energy savings in buildings by means of a micro-solar organic rankine cycle system: A simulation study," *Environments*, 5(11), 119, 2018, doi:10.3390/environments5110119.
- [9] D. Dragomir-Stanciu, S.M. Sagheblian, A. Kurchania, "The influence of condensing temperature on the efficiency of solar power systems with ORC," *Procedia Manufacturing*, 46, 359-363, 2020, doi:10.1016/j.promfg.2020.03.052.
- [10] M. Petrollese, G. Cau, D. Cocco, "The Ottana solar facility: dispatchable power from small-scale CSP plants based on ORC systems," *Renew. Energy*, 147, 2932-2943, 2020, doi:10.1016/j.renene.2018.07.013.
- [11] T.C. Roumpedakis, G. Loumpardis, E. Monokrousou, K. Braimakis, A. Charalampidis, S. Karellas, "Exergetic and economic analysis of a solar driven small scale ORC," *Renew. Energy* 157, 1008-1024, 2020, doi:10.1016/j.renene.2020.05.016.
- [12] A. Atiz, M. Karakilcik, "Comparison of heat efficiency of flat-plate and vacuum tube collectors integrated with Organic Rankine Cycle in Adana climate conditions," *Pamukkale Univ. J. Eng. Sci.* 26(1), 106-112, 2020, doi:10.5505/pajes.2019.34033.
- [13] F. Yilmaz, M. Ozturk, R. Selbas, "Design and thermodynamic modeling of a renewable energy based plant for hydrogen production and compression," *Int. J. Hydrogen Energy*, 45, 26126-26137, 2020, doi:10.1016/j.ijhydene.2019.12.133.
- [14] Y. Cao, A.M. Mohamed, M. Dahari, M. Delpisheh, M.A. Haghghi, "Performance enhancement and multi-objective optimization of a solar-driven setup with storage process using an innovative modification," *J. Energy Storage*, 32, 101956, 2020, doi:10.1016/j.est.2020.101956.
- [15] A. Atiz, H. Karakilcik, M. Erden, M. Karakilcik, "Assessment of power and hydrogen production performance of an integrated system based on middle-grade geothermal source and solar energy," *Int. J. Hydrogen Energy*, 46, 272-288, 2021, doi:10.1016/j.ijhydene.2020.10.016.
- [16] Z. Aghaziarati, A.H. Aghdam, "Thermoeconomic analysis of a novel combined cooling, heating and power system based on solar organic Rankine cycle and cascade refrigeration cycle," *Renew. Energy*, 164, 1267-1283, 2021, doi:10.1016/j.renene.2020.10.106.
- [17] F. Mahmood, T.A. Al-Ansari, "Design and thermodynamic analysis of a solar powered greenhouse for arid climates," *Desalination*, 497, 114769, 2021, doi:10.1016/j.desal.2020.114769.
- [18] N.B. Desai, H. Pranov, F. Haglind, "Techno-economic analysis of a foil-based solar collector

- driven electricity and fresh water generation system,” *Renew. Energy*, 165, 642-656, 2021, doi:10.1016/j.renene.2020.11.043.
- [19] M.A. Ancona, M. Bianchi, L. Branchini, A. De Pascale, F. Melino, A. Peretto, C. Poletto, & N. Torricelli, “Solar driven micro-ORC system assessment for residential application,” *Renewable Energy*, 195, 167-181, 2022, doi:10.1016/j.renene.2022.06.007.
- [20] Y. Aryanfar, M.E.H. Assad, A. Khosravi, R.S.M. Atiqure, S. Sharma, J.L.G. Alcaraz, & R. Alayi, “Energy, exergy and economic analysis of combined solar ORC-VCC power plant,” *International Journal of Low-Carbon Technologies*, 17, 196-205, 2022, doi:10.1093/ijlct/ctab099.
- [21] K. Mirjavadi, F. Pourfayaz, P. Pourmoghdam, & A. Kasaeian, “A comparison of using organic Rankine and Kalina cycles as bottom cycles in a solar-powered steam Rankine cycle,” *Energy Science and Engineering*, 10(8), 2714-2731, 2022, doi:10.1002/ese3.1161.
- [22] M. Rostami, M.D. Manshadi, & E. Afshari, “Energy production and storage from a polygeneration system based on parabolic trough solar collector, proton exchange membrane fuel cell, organic Rankine cycle, and alkaline electrolyzer,” *Journal of Energy Storage*, 47, 103635, 2022, doi:10.1016/j.est.2021.103635.
- [23] O. Kara, “An Evaluation of a New Solar-Assisted and Ground-Cooled Organic Rankine Cycle (ORC) with a Recuperator,” *Arabian Journal for Science and Engineering*, 2023, doi: 10.1007/s13369-022-07596-6.
- [24] P. Pourmoghdam, A. Kasaeian, “Economic and energy evaluation of a solar multi-generation system powered by the parabolic trough collectors,” *Energy*, 262, 125362, 2023, doi: 10.1016/j.energy.2022.125362.
- [25] F. Khalid, R. Kumar, “Thermodynamic assessment of a new PTC operated polygeneration system for fresh water, cooling, electricity and hydrogen production for a residential community,” *International Journal of Hydrogen Energy*, 2023, doi: 10.1016/j.ijhydene.2023.03.176.
- [26] F. Alshammari, N. Ben Khedher, & L. Ben Said, “Development of an automated design and off-design radial turbine model for solar organic Rankine cycle coupled to a parabolic trough solar collector,” *Applied Thermal Engineering*, 230, 120677, 2023, doi: 10.1016/j.applthermaleng.2023.120677.
- [27] O. Kara, “Evaluation of solar source and ground cooling performance in three different organic rankine cycle (ORC) configurations,” *Journal of Thermal Analysis and Calorimetry*, 148, 4401–4425, 2023, doi: 10.1007/s10973-023-11974-z.
- [28] H. Yağlı, Y. Koç, & H. Kalay, “Optimisation and exergy analysis of an organic Rankine cycle (ORC) used as a bottoming cycle in a cogeneration system producing steam and power,” *Sustainable Energy Technologies and Assessments*, 44, 100985, 2021, doi: 10.1016/j.seta.2020.100985.
- [29] I. Vaja, & A. Gambarotta, “Internal Combustion Engine (ICE) bottoming with Organic Rankine Cycles (ORCs),” *Energy*, 35, 1084-1093, 2010, doi: 10.1016/j.energy.2009.06.001.
- [30] C. Carcasci, R. Ferraro, & E. Miliotti, “Thermodynamic analysis of an organic Rankine cycle for waste heat recovery from gas turbines,” *Energy*, 65, 91-100, 2014, doi: 10.1016/j.energy.2013.11.080
- [31] H.M.D.P. Herath, M.A. Wijewardane, R.A.C.P. Ranasinghe, & J.G.A.S. Jayasekera, “Working fluid selection of Organic Rankine Cycles,” *Energy Reports*, 6, 680-686, 2020, doi: 10.1016/j.egy.2020.11.150.
- [32] C. Tzivanidis, E. Bellos, K.A. Antonopoulos, “Energetic and financial investigation of a stand-alone solar-thermal Organic Rankine Cycle power plant,” *Energy Conversion and Management*, 126, 421-433, 2016, doi:10.1016/j.enconman.2016.08.033.
- [33] J. Song, & C.-w. Gu, “Parametric analysis of a dual loop Organic Rankine Cycle (ORC) system for engine waste heat recovery,” *Energy Conversion and Management*, 105, 995-1005, 2015, doi: 10.1016/j.enconman.2015.08.074.
- [34] G. Xu, G. Song, X. Zhu, W. Gao, H. Li, & Y. Quan, “Performance evaluation of a direct vapor generation supercritical ORC system driven by linear Fresnel reflector solar concentrator,” *Applied Thermal Engineering*, 80, 196-204, 2015, doi:10.1016/j.applthermaleng.2014.12.071.
- [35] A. Uusitalo, T. Turunen-Saaresti, J. Honkatukia, P. Colonna, and J. Larjola, "Siloxanes as Working Fluids for Mini-ORC Systems Based on High-Speed Turbogenerator Technology," *ASME. J. Eng. Gas Turbines Power*, 135(4), 042305, 2013, doi:10.1115/1.4023115.
- [36] A.M. Delgado-Torres, & L. García-Rodríguez, “Preliminary assessment of solar organic Rankine cycles for driving a desalination System,” *Desalination*, doi: 216, 252-275, 2007, 10.1016/j.desal.2006.12.011.
- [37] Y. Liang, G. Shu, H. Tian, H. Wei, et al., "Thermodynamic Analysis of an Electricity-Cooling WHR Cogeneration System Aboard Ships using Siloxanes as Working Fluids," *SAE Technical Paper*, 2014-01-1946, 2014, doi:10.4271/2014-01-1946.
- [38] *Güneş Enerjisi Potansiyeli Atlası (GEPA)* [Online] Available: <https://gepa.enerji.gov.tr/MyCalculator/> (accessed Jan. 3, 2023).
- [39] Y. Peng, X. Lin, J. Liu, W. Su, & N. Zhou, “Machine learning prediction of ORC performance based on properties of working fluid,” *Applied Thermal Engineering*, 195, 117184, 2021, doi:10.1016/j.applthermaleng.2021.117184.
- [40] D. Vera, F. Jurado, J. Carpio, & S. Kamel, S. “Biomass gasification coupled to an EFGT-ORC combined system to maximize the electrical energy generation: A case applied to the olive oil industry,” *Energy*, 144, 41-53, 2018, doi:10.1016/j.energy.2017.11.152.

- [41] *Fluid Safety Data Sheets* [Online]. Available: <https://www.fishersci.com/us/en/home.html> (accessed June. 6, 2023).
- [42] S. Klein, EES-Engineering Equation Solver, *F-Chart Softw*, 2020.
- [43] Y.A. Çengel, M.A. Boles, *Thermodynamics: An engineering approach 6th Edition (SI Units)*. New York.: The McGraw-Hill Companies Inc; 2008.
- [44] S.A. Kalogirou, "Parabolic trough collectors for industrial process heat in Cyprus," *Energy*, 27, 813-830, 2002, doi: 10.1016/S0360-5442(02)00018-X
- [45] E. Georges, S. Declaye, O. Dumont, S. Quoilin, & V. Lemort, "Design of a small-scale organic rankine cycle engine used in a solar power plant," *International Journal of Low-Carbon Technologies*, 8, 34-41, 2013, doi: 10.1093/ijlct/ctt030.
- [46] J. Yang, J. Li, Z. Yang, & Y. Duan, "Thermodynamic analysis and optimization of a solar organic Rankine cycle operating with stable output," *Energy Conversion and Management*, 187, 459-471, 2019, doi: 10.1016/j.enconman.2019.03.021.
- [47] W. Zhao, N. Xie, W. Zhang, J. Yue, L. Wang, X. Bu, H. Li, "Performance characteristics and working fluid selection for high-temperature organic Rankine cycle driven by solar parabolic trough collector," *International Journal of Low-Carbon Technologies*, 16(4), 1135-1149, 2021, doi: 10.1093/ijlct/ctab036.
- [48] Wang, K., A.M. Pantaleo, M. Herrando, M. Faccia, I. Pasmazoglou, B.M. Franchetti, & C.N. Markides, "Spectral-splitting hybrid PV-thermal (PVT) systems for combined heat and power provision to dairy farms," *Renewable Energy*, 159, 1047-1065, 2020, doi: 10.1016/j.renene.2020.05.120.
- [49] F. Calise, D. Capuano, & L. Vanoli, "Dynamic simulation and exergo-economic optimization of a hybrid solar-geothermal cogeneration plant," *Energies*, 8(4), 2606-2646, 2015, doi: 10.3390/en8042606.

Research Article

Performance Investigation of Ejector Assisted Power Cooling Absorption Cycle

*B.Mebarki 

Laboratory of Built Environment, Department of Structures and Materials, Faculty of Civil Engineering, University of Science and Technology Houari Boumediene (USTHB), Bab Ezzouar, Alger, Algeria
E-mail: mebarkibillel88@gmail.com, billal.mebarki@usthb.edu.dz

Received 3 February 2023 , Revised 25 June 2023, Accepted 15 August 2023

Abstract

In this paper, new cycle is developed to generate simultaneously electrical and cooling power by placing a turbine between the generator and ejector in the conventional ejector-assisted absorption cooling cycle. The aim of developed cycle is to increase the exergy efficiency of cycle by adding an electrical power generation made it more environmentally friendly and reduce its dependents of fossil energy sources. The first, second laws of thermodynamic, mass and energy balance is applied for each cycle component and the constant mixing pressure ejector model is used to develop a numerical model of proposed cycle. The results depict that the augmentation of generation temperature is positively affected the work produced in the turbine contrary for cycle coefficient of performance, for every working conditions there are a certain value of generation temperature which its exergy performance of cycle achieves the maximum, the augmentation of output pressure of turbine is positively affected the cycle coefficient of performance contrary of the work produced in the turbine and the cycle exergy efficiency and the augmentation of condensation temperature is positively affected the cycle exergy efficiency and the work produced in the turbine contrary for cycle coefficient of performance and the augmentation of evaporation temperature is positively affected the cycle coefficient of performance and the cycle exergy efficiency contrary for the work produced in the turbine. The results also show that the improvement of exergy efficiency of proposed cycle is 29.41% and 46% compared with the absorption cooling cycle with double and triple effect under the same operating conditions.

Keywords: Absorption; ejector; COP; electrical power; cooling.

1. Introduction

The friendly environmentally cycle needs more independent of conventional energy source as like fossil source, the idea is to develop a cooling cycle which simultaneously can be generated an electrical power using water vapor high pressure outlet of generator of conventional ejector assisted absorption cycle. The new cycle generates electrical energy and cooling simultaneously, which is expected to improve the poor exergy efficiency of the absorption cooling cycle [1]. The new proposed cycle is based on placing a turbine between the generator and the ejector in the conventional ejector-assisted absorption cycle to exploit the maximum pressure difference between the pressure of the steam leaving the generator and the pressure of the ejector's primary fluid entering the ejector, which can operate at a pressure below the generator pressure

In recent years, many works have proposed some cycles to dispute the irreversibility of power generation from low-grade heat source or waste heat. Meng et al [2] investigated the performance of a modified organic Rankine cycle combined with a flash process using a thermodynamic and techno-economic study. The results depict that the evaporator and the condenser are mainly responsible for the irreversibility of the cycle and the use of flash tank process reduces the irreversibility Cihan and Kavasoğulları [3]

proposed a new organic Rankine cycle which produced both cooling and electrical power using an ejector and two turbine. The energy and exergy performance of proposed cycle working with various organic fluids R123, R600, R245fa, R141b, and R600a were analyzed under different evaporation and condensation temperature. The results show that the R141b is the more appropriate fluid of proposed cycle in point of view energy and exergy analysis.

Li et al [4] investigated an ejector assisted organic Rankine flash cycle using the first and second thermodynamic laws. The results show that the ejector-assisted organic Rankine flash cycle has better exergy and thermal efficiency than the conventional Rankine flash cycle in every working condition. Mendal et al [5] modified a conventional waste heat driven organic flash power cycle by replacing the low pressure throttle valve with an ejector. They found that the cooling performance is positively affected as the pressure in the flash tank increases, and the proposed cycle thermal efficiency is enhanced compared with conventional organic flash power plant. Mendel at al [6] proposed a compressor-ejector refrigeration cycle based on adding an ejector between the compressor and the condenser. The results show that there is a pressure ratio of the compressor corresponding to a maximum value of the coefficient of performance of the cycle under all operating conditions of the cycle. The coefficient of performance of

the conventional ejector cycle and the developed ejector-compressor cycle can be improved by 25.7% and 37.2%, respectively, compared to the ejector-expansion cycle operating with R32 and R1234yf. Mendel et al [7] proposed a geothermal flash steam cycle with ejector support. The main modification of the proposed cycle is that the saturated water from the high pressure steam separator enters the ejector as the primary fluid compared to the dual flash steam cycle. The results show that the proposed cycle performance can be improved by 6.67% compared to the dual flash steam cycle. The cost is also 4.5% lower.

The use of the ejector to improve the exergy efficiency and coefficient of performance of the absorption cooling cycle has been discussed in a few papers. Azhar et al [8] proposed three various cycle of a dual ejector assisted absorption cycle using flash tank working with solar energy; the approach of their study is techno economic. They found that the cycle proposed N^o3 is more 10 % cheaper than cycle proposed N^o2 and 27% cheaper than cycle proposed N^o2. They found also that the payback period and profit gain of cycle proposed N^o3 against the conventional dual ejector assisted absorption cycle with flash tank are 16 years and 874 \$. Hai et al [9] proposed and optimized a new bi evaporator cycle combined an absorption cycle and CO₂ ejector cycle. They found that the new cycle is better performance than the conventional CO₂ ejector cycle and the gas cooler. They concluded also that the generator is the main responsibility of irreversibility of cycle. Khalili et al [10] proposed a new double ejector multi pressure level absorption cycle with two schemes. The results depict that the proposal cycles developed cycle coefficient of performance by 108.35 % and 33.11 % comparing with conventional absorption cycle and the lower evaporation temperature can be reach -24°C. Al Hamed et al [11] proposed an ejector assisted absorption cycle using solar energy and geothermal energy for a small community. They found that the exergy efficiency of integrated system with two source of renewable energy reaches 55.98 % and the system coefficient of performance is equal to 63.60 %. Göktun [12] studied the effect of adding an ejector to simple effect absorption cooling cycle on its performance using the first law of thermodynamics. The results show that a growth up to 40% in the coefficient of performance of the ejector assisted absorption cycle can be achieved compared to the ordinary absorption cooling cycle. Majdi [13] designed an absorption refrigeration cycle combined with ejector which is placed between the generator and condenser to direct part of the steam coming from the evaporator to the condenser. He found that the coefficient of performance of the proposed cycle could be improved by 60% compared to the simple effect absorption cycle. Jiang et al [14] compared the ejector assisted absorption refrigeration cycle with the double effect absorption cooling cycle. They concluded that the performance coefficient of conventional double effect is slightly higher than that of the proposed cycle, which its annual operating cost is lower than that of the conventional double effect absorption cycle. Sirwan et al [15] developed a new ejector assisted absorption cooling cycle with flash tank. They found that most of the exergy destruction occurs in the evaporator, condenser and absorber, respectively. Sözen and Özalp [16] proposed ammonia absorption refrigeration cycle using liquid ejector which is placed between the generator and the absorber. They found that the coefficient of performance and exergy efficiency of

proposed cycle improved by 49% and 56%, respectively, compared to a conventional absorption refrigeration cycle. Abed et al [17] developed an electrical plant using geothermal source combined with a single stage CO₂ transcritical cycle. They concluded that the proposed cycle reaches an exergy efficiency equal to 32% in the usual operating conditions rising to 39.21% with the Genetic Algorithm and 36.16% with the Nelder–Mead simplex method. Yi et al [18] developed an ejector absorption cycle before expansion to generate electric power using ocean thermal energy. They concluded that the work of the output turbine can be improved by 79% by using the pre-expansion process in the cycle. Bhowmick et al [19] can be proposed an ejector assisted absorption cooling cycle with regenerative Rankine cycle for both cooling and power generation using waste heat sources. The results show that the exergy efficiency of proposed cycle can be achieved 44.18%. Khalili et al [20] proposed a double liquid vapor ejector absorption cycle; the two ejectors are installed between the absorber and condenser. They found that the coefficient of performance and exergy efficiency of the proposed cycle can be improved by 108.35%, 33.11% and 31.61%, 46.62% compared to the basic absorption cycle and to the ejector assisted absorption cycle, respectively. Sioud et al [21] developed a dual effect ejector assisted absorption cycle. They concluded that the coefficient of performance of the cycle can be equaled 1.7 at a generation temperature equal to 340 °C. Vereda et al [22] proposed ejector assisted absorption cycle; the ejector is placed between the solution heat exchanger and the absorber to direct the refrigerant vapor coming from the evaporator with the rich solution coming from the generator. They concluded that the coefficient of performance of the proposed cycle is the same coefficient of performance as a single-effect absorption cycle with higher generation temperature of 9°C. Therefore; it can be used with a low grade temperature source.

The enhancement of ejector process is subject of many studies. Tang et al [23] developed a novel physical model of the mixing chamber of an ejector and concluded that the conventional laws of chamber mixing between primary ejector fluid and secondary ejector fluid do not accurately represent the mixing process, which is also true for the energy and momentum laws. Therefore, a complete understanding of the mixing process was presented in their work. Thongtip and Aphornratana [24] conducted an experimental study to determine the effects of nozzle chamber geometry on ejector performance. They concluded that for specific working conditions, there are certain geometry is required to achieve maximum performance, e.g., for low temperature generation, the use of a nozzle with the largest throat area is recommended to achieve maximum performance. Wang et al [25] performed a simulation of the primary nozzle with different geometries and surface roughness. They concluded that the entrainment ratio is high depending on the geometry of the primary nozzle and the surface roughness. Van Nguyen et al [26] performed an experimental and numerical study on an ejector with variable nozzle geometries. They concluded that a 24% improvement in the coefficient of performance can be achieved with using an ejector with variable nozzle geometries.

The ejector that has been used is various applications like refrigeration, lubricant and desalination [27], and it is the subject of many researchers which have focused on

ejector modeling. Kavasogullari et al [28] developed a dual ejector refrigeration cycle by adding second ejector and refrigeration pump to conventional ejector assisted compression refrigeration cycle. They found that the coefficient of performance and exergy efficiency of proposed cycle can be achieved 7.52 and 38.8%, respectively and the improvement in the coefficient of performance and exergy efficiency are significantly in the high condensing and low evaporation temperature Varga et al. [29] studied the effect of many design parameters on the performance of ejector like nozzle exit position, constant area length and the ratio of the area between the nozzle and the constant area. They concluded that for every working condition there is an optimal ratio which had the maximum performance of ejector. Sriveerakul et al. [30] developed a CFD model of ejector in refrigeration cycle, the model developed is validated by experimental data. They concluded that the CFD is an efficient method to represent the flow inside the ejector. Ariafar [31] used CFD method to study the effect of exit diameter of primary nozzle. He concluded that the increasing of motive pressure will increase the entrainment ratio and the increasing of Mach number in the exit of nozzle chamber and its area does not affect the ejector performance but it will affect the pressure distribution at outlet nozzle chamber.

Li et al. [32] developed a new ejector assisted high temperature compressor refrigeration cycle. They studied the effect of many ejector parameters like throat area and primary nozzle chamber length and the output area of nozzle chamber. They found that the new cycle using ejector could be reduced the cost of refrigeration machine from 59 795\$ to 3311 \$, thus an economical cost can be reach 94 % and the temperature outlet of compressor reduced from 184.8°C to 110 °C in comparing with conventional high temperature compressor refrigeration cycle. Tashtoush and Nayfeh [33] compared both constant and variable geometry ejector as the expansion component in the compression refrigeration cycle. They found that the variable geometry ejector is more suitable ejector for solar refrigeration cycle because of variation of its working condition.

However, the ejector design can be divided into two designs according to the existing nozzle chamber, if there is a constant area, therefore, the ejector is called the constant area ejector, if not, the ejector with constant pressure ejector is called Huang et al [34]. The constant pressure ejector theory developed by Keenan et al [35] is mostly used to modulate the pressure in the mixing chamber of the ejector because it has high stability and performance compared to the constant area ejector [26]. In this study, the ejector is a constant mixing pressure ejector to maximize the performance, and the model used is one-dimensional as it is very often used in thermodynamic studies of the cycle [36].

This study based on the use of high pressure of generator to rotate a turbine for electrical power generation and an ejector to entrain the water vapor coming from evaporator with water vapor coming from turbine. The aim of this paper is to investigate the performance of proposed cycle and the effect of various design parameters on its performance.

2. Cycle Description

The proposed ejector absorption cycle is shown in Figure 1. The refrigerant/absorbent pair used in this study is water/lithium bromide. The objective of this study is to thermodynamically analyze the proposed cycle. Our proposed cycle consists of a generator, a condenser, a turbine, an evaporator, a heat exchanger, an expansion valve, a reducing valve, an ejector, and a solution pump. In the evaporator, the refrigerant water is converted into steam, which then splits into two parts. The first part of the vapor enters the absorber and then meets the strong solution coming from the generator and passes through the heat exchanger and the reducing valve. The refrigerant out letting the evaporator enters into absorber and reaches the weak solution coming from reducing valve to produce strong solution. As the amount of lithium bromide dissolved in the water increases, the temperature of the solution decreases and leaves the heat as a condenser. The weak solution leaves the absorber and enters the pump, where its pressure increases to the pressure of the generator. Then the steam leaves the generator at high pressure and enters the turbine, where it expands to an intermediate pressure between the pressure of the generator and the pressure of the condenser. The expanded steam leaves the turbine and enters the ejector as the primary fluid, where it meets the second part of the steam leaving the evaporator in the mixing part of the ejector as the second fluid of the ejector, then the steam leaves the ejector under condenser pressure, enters the condenser and returns to the evaporator through the expansion valve to close the cycle.

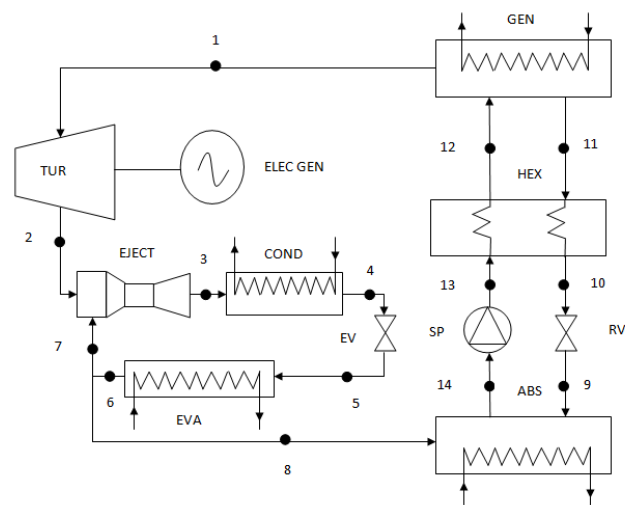


Figure 1. The proposed cycle of ejector assisted absorption cycle.

Where TUR is the turbine, ELEC GEN is the electrical generator, EJECT is the ejector, COND is the condenser, EVA is the evaporator, ABS is the absorber, HEX is the solution heat exchanger, GEN is the generator, SP is the solution pump, EV is the expansion valve and RV is the reducing valve.

In The state points 1, 2, 3, 6, 7 and 8, the state of fluid is water vapor but in the state point 4, the state of fluid is saturate liquid which became mixture (liquid vapor) in the state point 5. In the state points 9, 10 and 11, the solution of lithium bromide water is poor solution but became rich solution in the state points 12, 13 and 14.

3. Thermodynamic Cycle Model

3.1 Ejector Model

The ejector model used in our study is a one dimensional model constant mixing pressure based on the following simplicity assumptions:

- An adiabatic one dimensional flow in the ejector [37].
- The velocities of primary and secondly fluid in the inlet and outlet of ejector are neglected [37].
- The efficiency of the nozzle, mixing chamber and diffusers are assumed to be constant [37].
- All losses of refrigerants flow are measured by using of different efficiency chambers [37].

Applying the mass, energy and momentum conservation in the different chambers of ejector and respect the above assumptions. The different parameters of ejector model are defined.

The velocity of primary fluid in the outlet of nozzle chamber is presented in the following equation by using of energy conservation and neglected of its velocity in the inlet of the nozzle chamber [37]:

$$U_{n,out} = \sqrt{\eta_n \cdot (h_{p,in} - h_{n,out,is})} \cdot 1000 \quad (1)$$

Where U is the velocity of primary fluid, $h_{p,in}$ is the enthalpy of primary fluid to nozzle chamber, η_n is the nozzle chamber isentropic efficiency, in is the inlet of the nozzle chamber, out is the outlet of the nozzle chamber and is is the isentropic expansion.

Applying the momentum and the energy conservation in the mixing chamber and the neglecting of the secondly fluid velocity, the velocity and the enthalpy of mixing fluid in the outlet of mixing chamber are presented by following equations [37]:

$$U_{m,out} = \frac{U_{n,out}}{1+\mu} \sqrt{\eta_m} \quad (2)$$

$$h_{m,out} = \frac{h_{n,in} + \mu \cdot h_{s,in}}{1+\mu} - \left(\frac{U_{n,out}^2}{2} \right) / 1000 \quad (3)$$

Where $h_{s,in}$ is the enthalpy of secondly fluid in the inlet of the nozzle chamber, η_m is the mixing chamber efficiency and the μ depicts the entrainment ratio where is defined by the following equation [37]:

$$\mu = \frac{m_p}{m_s} \quad (4)$$

Applying of energy conservation in the diffuser and assuming that the compression in the diffuser chamber is isentropic, the enthalpy of outlet of diffuser and the ejector can be presented by following equation [37]:

$$h_{d,out} = h_{m,out} + \frac{h_{d,out,is} - h_{m,out}}{\eta_d} \quad (5)$$

Where the η_d is the diffuser efficiency.

Based on the previous equations the entrainment ratio can be calculated by following equation [37]:

$$\mu = \sqrt{\eta_n \cdot \eta_m \cdot \eta_d \frac{h_{p,in} - h_{n,out,is}}{h_{d,out,is} - h_{m,out}}} - 1 \quad (6)$$

3.2 Thermodynamic Model

The energy and exergy analysis are used in this study to investigate the thermodynamic performance of proposed cycle. According to many researchers the exergy analysis is the best way to evaluate the performance of thermodynamic process [1].

In this study, the mass conservation, the first and second laws of thermodynamics are applied to each component of proposed cycle.

Some simplify assumptions are made to simplify the study of our machine:

- The proposed cycle is under steady condition [1], [34].
- The drop of pressure in all component of system is negligible except in the ejector [1], [34].
- There is no loss or gain heat from or to system except what are considered in study [1].
- The expansion in the expansion valve, in the reducing vane and is isenthalpic [1].
- The expansion in the turbine is isentropic.
- The state of refrigerant of outlet of condenser and evaporator are in saturate liquid and saturate vapor, respectively [1].

3.3 Mass Conservation

Mass conservation includes the mass balance of total mass and each material of the solution. The governing equations of mass and type of material conservation for a steady state system are [1]:

$$\sum m_i - \sum m_o = 0 \quad (7)$$

$$\sum m_i \cdot x_i - \sum m_o \cdot x_o = 0 \quad (8)$$

Where m is the mass flow rate and x is the mass fraction of lithium bromide in the solution. The mass fraction of the mixture at different points of the process (Figure1) is calculated using the corresponding temperature and pressure data.

3.4 The first Law of Thermodynamics

For each component of the proposed cycle, the first law of thermodynamics is applied as follows [1]:

$$\left(\sum m_i \cdot h_i - \sum m_o \cdot h_o \right) + \left(\sum Q_i - \sum Q_o \right) + W = 0 \quad (9)$$

Where h is the specific enthalpy, Q is heat exchanged and W is the mechanical work to or from to component.

The energy balance equations of different components of the proposed cycle are summarized in the table 1.

3.5 The Second Law of Thermodynamics

In an open system and neglecting of kinetics energy, the exergy balance equation can be expressed follows as [1]:

$$Ex = \sum_j Q_j \cdot \left(1 - \frac{T_0}{T_i} \right) + \left(\sum_i m_i \cdot ex_i \right)_{in} - \left(\sum_i m_i \cdot ex_i \right)_{out} - W \quad (10)$$

Where ex_i is the specific exergy of flow which can be defined as [1]:

$$ex_i = (h_i - h_0) - T_0 \cdot (S_i - S_0) \quad (11)$$

Where h_0, T_0 and S_0 are represent the specific enthalpy, temperature and specific entropy of reference environmental state of water which are $T_0=25$ °C and $P_0=101$ KPa.

Table 1. The energy balance of different cycle component.

Cycle component	The energy balance
Generator	$Q_g = m_1 \cdot h_1 + m_{11} \cdot h_{11} - m_{12} \cdot h_{12}$
Absorber	$Q_a = m_8 \cdot h_8 + m_9 \cdot h_9 - m_{14} \cdot h_{14}$
Condenser	$Q_c = m_4 \cdot h_4 - m_3 \cdot h_3$
Evaporator	$Q_e = m_6 \cdot h_6 - m_5 \cdot h_5$
Expansion valve	$h_5 = h_4$
Reducing valve	$h_{10} = h_9$
Heat exchanger	$T_{10} = T_{11} - \varepsilon \cdot (T_{11} - T_{13})$ $h_{12} = \frac{m_{11}}{m_{13}} \cdot (h_{11} - h_{13}) + h_{13}$
Turbine	$W_t = m_1 \cdot (h_2 - h_1)$
Pump	$W_p = m_{14} \cdot \frac{(P_{13} - P_{14})}{\eta_p \cdot \rho_{14}}$

The destruction exergy of different component of proposed cycle are presented in the table 2:

Table 2. The exergy destruction of different cycle component.

Cycle component	The destruction exergy
Generator	$Ex_g = Q_g \cdot \left(1 - \frac{T_0}{T_g}\right) - m_1 \cdot ex_1 - m_{11} \cdot ex_{11} + m_{12} \cdot ex_{12}$
Absorber	$Ex_a = -Q_a \cdot \left(1 - \frac{T_0}{T_a}\right) + m_8 \cdot ex_8 + m_9 \cdot ex_9 - m_{14} \cdot ex_{14}$
Condenser	$Ex_c = -Q_c \cdot \left(1 - \frac{T_0}{T_c}\right) - m_4 \cdot ex_4 + m_3 \cdot ex_3$
Evaporator	$Ex_e = Q_e \cdot \left(1 - \frac{T_0}{T_e}\right) + m_6 \cdot ex_6 + m_5 \cdot ex_5$
Expansion valve	$Ex_{ev} = m_4 \cdot T_0 \cdot (S_4 - S_5)$
Reducing valve	$Ex_{rv} = m_{10} \cdot T_{10} \cdot (S_{10} - S_9)$
Heat exchanger	$Ex_{hx} = m_{11} \cdot ex_{11} + m_{13} \cdot ex_{13} - m_{10} \cdot ex_{10} - m_{12} \cdot ex_{12}$
Turbine	$Ex_t = m_1 \cdot ex_1 - m_2 \cdot ex_2 - W_t$
Pump	$Ex_p = m_{14} \cdot ex_{14} - m_{13} \cdot ex_{13} + W_p$

The destruction exergy of the proposed cycle Ex_{dt} is the sum of exergy destruction of each its component. It can be calculated by following equation [37]

$$Ex_{dt} = \sum Ex_i \quad (12)$$

The exergy entering in the proposed cycle can be evaluated by [35]

$$Ex_{in} = Q_g \cdot \left(1 - \frac{T_0}{T_g}\right) + W_p \quad (13)$$

The exergy efficiency of the presented cycle is calculated by following equation [37]

$$\eta_{ex} = 1 - \frac{Ex_{tot}}{Ex_{in}} \quad (14)$$

4. Results and Discussions

The performance simulation of the proposed cycle is based on a program developed in Matlab.

The thermodynamic properties of lithium bromide water and liquid water are calculated using the efficient calculation formulas developed by Patek and Klomfar [38], and the thermodynamic properties of steam are calculated using the formula developed by Patek and Klomfar [39].

Based on the thermodynamic model presented above, the flowchart of the simulation resolution equation is shown in Figure 2.

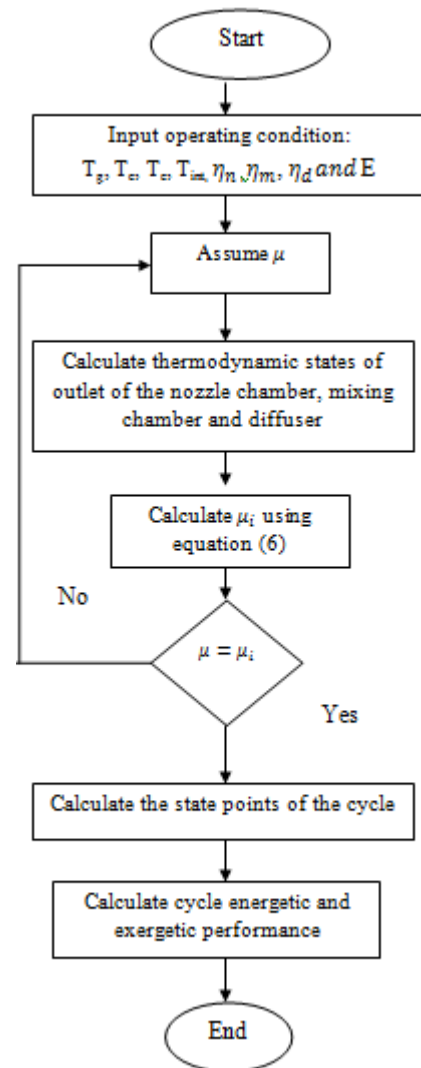


Figure 2. The flowchart of simulation calculation.

An iterative method is applied to define the entrainment ratio of ejector by assumed its value then calculate the different state of fluid in the outlet of the nozzle chamber, mixing chamber and diffuser of ejector applying Eqs. (1) – (5) and calculate the new value of entrainment ratio using Eq. (6), if the different between its two successive value calculated is under 10^{-4} then it is the real value of entrainment ratio.

After the known of entrainment ratio, it could be determinate the firstly ejector fluid mass flow which is equal to mass flow thronging the evaporator multiplied by entrainment ratio and the firstly ejector fluid mass flow which is equal to mass flow thronging the evaporator multiplied by $(1 - \mu)$. Then, it can be applied all Eqs. (7) – (14) to determine different mass and heat balance, exergy destruction in the different component, the cycle coefficient of performance and the cycle exergy efficiency. The table 3 depicts the different state point properties of proposed cycle at optimum operating conditions.

4.1 Model Validation

The ejector model validation based on the comparison between results available in the literature experimental study of ref [34], numerical study of ref [37] and results

obtained from our proposed model in same working conditions, the evaporator temperature is equal to 8 °C, the working fluid is R141b and same different generator and condenser temperature. The results of comparison are resumed in table 4. It can be seen that the average of error of calculated results with experimental is 3.86% and 3.3% with numerical data of ref [37]. Thus, it can be used our model to predict ejector behavior.

Table 3. The different properties of proposed cycle state point at optimum operating condition.

Number of state point	T (K)	P (kPa)	h (kJ/kg)	S (kJ/kg.K)	X (g/kg)	m (kg/sec)
1	426	513.66	3361	7.91		0.09791
2	333	19.80	2609	7.91		0.09791
3	321	4.21	2589	8.563		0.1253
4	303	4.21	125.1	0.4347		0.1253
5	283	1.216	125.1	0.4445		0.1253
6	283	1.216	2519	8.903		0.1253
7	283	1.216	2519	8.903		0.02739
8	283	1.216	2519	8.903		0.09791
9	339.9	1.216	279.4	0.9152	0.1	0.2006
10	339.9	513.66	278.8	0.9147	0.1	0.2006
11	426	513.66	644.4	1.869	0.1	0.2006
12	392.7	513.66	942.9	0.8258	488	0.29851
13	303	513.66	398.8	0.2215	488	0.29851
14	303	1.216	59.73	0.2283	488	0.29851

Table 4. Comparisons of ejector model results with experimental results of ref [34] and numerical results of ref [37].

T _g (°C)	T _c (°C)	Entrainment Ratio			Error Exp [34] (%)	Error Num [37] (%)
		Exp [34]	Num [37]	Our model		
95	31.3	0.4377	0.4584	0.4473	-2.15	2.48
	33	0.3937	0.4114	0.4003	-1.65	2.77
	34.2	0.3505	0.3811	0.3701	-5.30	2.97
90	33.8	0.3488	0.3614	0.3507	-0.54	3.05
	36.7	0.3040	0.2967	0.284	7.04	4.47
	37.5	0.2718	0.2806	0.27	0.67	3.93
84	32.3	0.3883	0.3608	0.3504	10.82	2.97
	33.6	0.3117	0.3286	0.3182	-2.04	3.27
	35.5	0.2880	0.2858	0.2754	4.58	3.78

4.2 Effect of Generation Temperature

The figure 3 depicts the effect of varying the generation temperature on the coefficient performance of cycle, the cycle exergy efficiency and on the work produced in the turbine. These results obtained in the following operating conditions, the condensation temperature has been assumed at 30°C, the evaporation temperature has been assumed at 10°C, the cooling capacity is equal to 300 kW and the outlet pressure of turbine is equal to 12.261 kPa. It can be seen that the coefficient of performance decrease with increasing the generation temperature contrary of work produced in the turbine. The exergy efficiency of the cycle increase to a certain value of generation temperature then decrease with increasing the generation temperature, in our operating conditions the maximum exergy efficiency is equal to 42.63% with 95.33 kW of work produced in the turbine at generation temperature equal to 152.3 °C. these results can be explained by an increasing in the generation temperature conducts an increasing in the water vapor desorbed in the generator and in the amount flow of turbine which is developing its work produced, contrary for coefficient of performance an increasing in the generation temperature conducts an increasing in the heat absorbed by generator from generation source with a constant cooling

power produced equal to 300 kW, thus, the COP deteriorate. The exergy efficiency of cycle is increasing with increasing of generation temperature because the augmentation of exergy production which is the work produced in the turbine is more important than the augmentation of exergy destruction which is the heat absorbed by generator until a certain generation temperature which the exergy destruction in the generator become more important than the exergy production with augmentation of generator temperature.

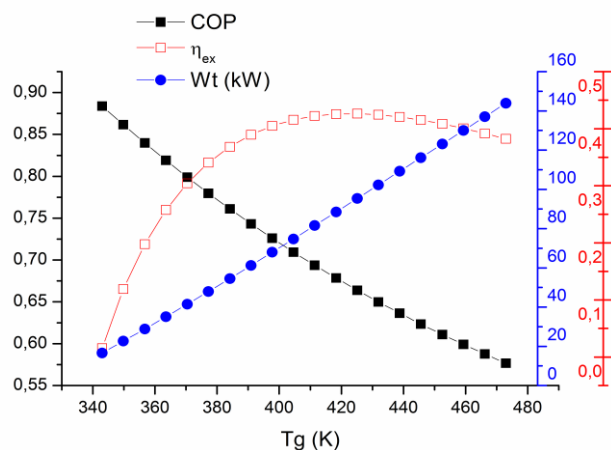


Figure 3. The effect of generation temperature on the coefficient of performance, the exergy efficiency and on the turbine work produced.

4.3 Effect of Outlet Pressure of Turbine

The figure 4 depicts the effect of varying the pressure outlet of turbine on the coefficient performance of cycle, the exergy efficiency and on the turbine work produced. The operating conditions of simulation are the condensation temperature is equal to 30°C, the evaporation temperature is equal to 10°C, the cooling capacity is equal to 300 kW and the temperature of generation is equal to 120 °C. It is clear that the coefficient of performance slowly increases but the work produced in the turbine slowly decrease with increasing the pressure outlet of turbine. The exergy efficiency is strongly deteriorated by the increasing the outlet pressure of turbine. These results can be explained by the augmentation of outlet pressure of the turbine conducts to decrease both the work produced of turbine and the exergy produced of cycle which is deteriorate the cycle exergy efficiency, on the contrary for the entrainment ratio, an increasing in the outlet pressure of the turbine which is the pressure of primary fluid of ejector conducts to develop the entrainment ratio which means that the mass flow of secondly fluid of ejector increased and the rest water vapor enters to absorber decreased which conducts to diminution of generation heat absorbed by generator and increases the coefficient performance of cycle COP.

The figure 5 depicts the effect of varying the pressure outlet of turbine on the entrainment ratio of ejector. The results depict that the entrainment ratio of ejector increases with an increasing of the pressure outlet of turbine. These results can be explained by the increasing of the outlet pressure of the turbine which is the primary fluid pressure of ejector conducts an increase in the secondly fluid mass flow of the ejector which is water vapor leaving the evaporator as consequently the entrainment ratio increases. Deng et al [40] found the similar phenomena in their study.

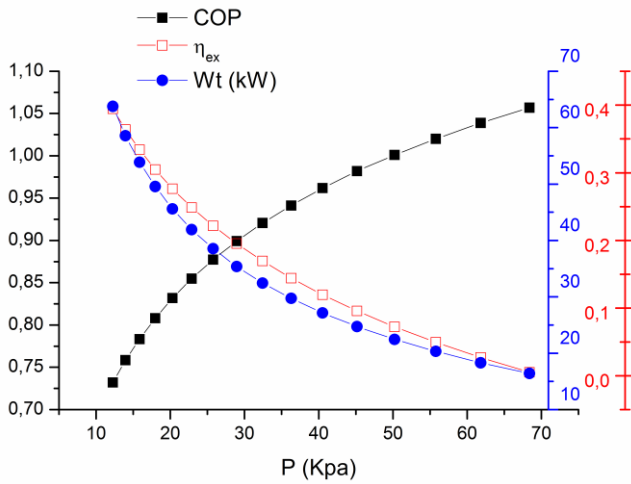


Figure 4. The effect of pressure outlet of turbine on the coefficient of performance, the exergy efficiency and the work produced in the turbine.

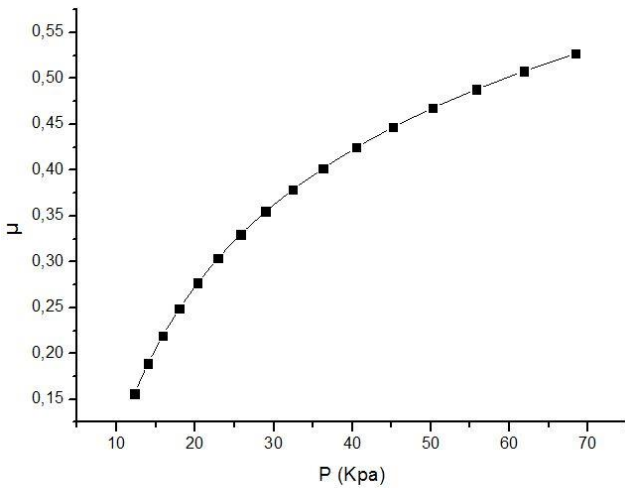


Figure 5. The effect of pressure outlet of turbine on the entrainment ratio of ejector.

4.4 The Effect of Condensation Temperature

The figure 6 depicts the effect of varying the condensation temperature on the cycle coefficient of performance, the cycle exergy efficiency and the work produced in the turbine. This simulation operated under following conditions the outlet pressure of turbine seems to be equal to 12.261 kPa, the evaporation temperature is equal to 10°C, the cooling capacity is equal to 300 kW and the temperature of generation is equal to 120 °C. It is clear that the increasing in the condensation temperature is positively affecting the work produced in the turbine and the exergy efficiency contrary of coefficient of performance. It can be explained these results by the condensation pressure is also the pressure of ejector diffuser which is inversely proportional to the second fluid mass flow of ejector as consequence the water vapor flow entering the absorber augmented correspondingly the rich solution flow entering to the generator which conducts an increasing in the heat absorbed by the generator.

The figure 7 depicts the effect of varying the condensation pressure on the entrainment ratio of ejector. It can be seen that an increasing in the condensation pressure conducts to diminution in the entrainment ratio. These results can be explained by the secondly fluid mass flow is negatively affected with an augmentation in the

condensation pressure because of it is the pressure of water vapor leaving the ejector.

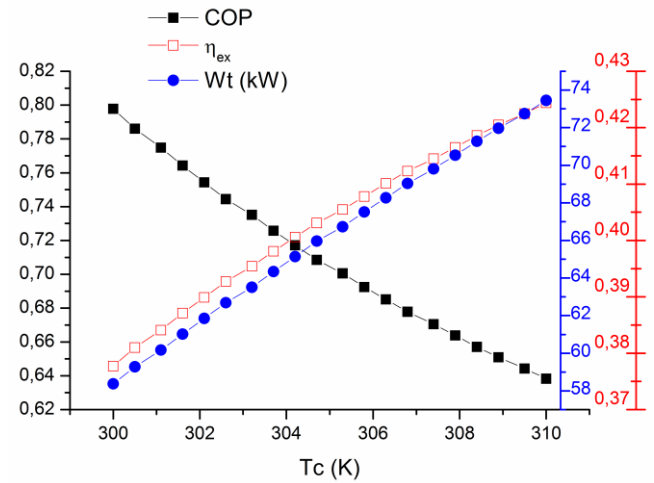


Figure 6. The effect of condensation temperature on the coefficient of performance, the exergy efficiency and the work produced in the turbine.

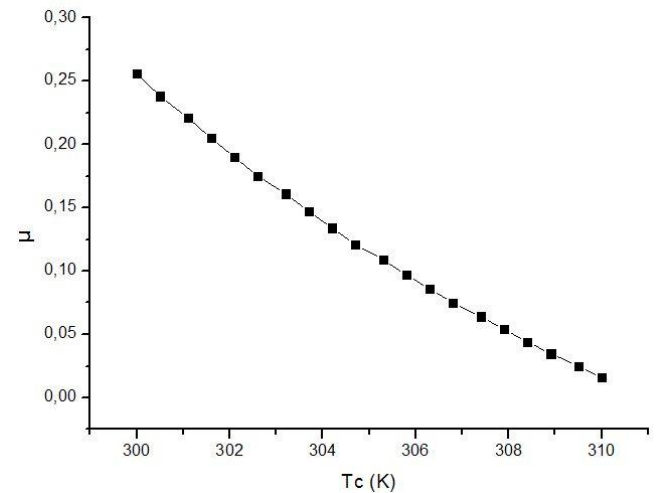


Figure 7. The effect of condensation temperature on the entrainment ratio.

4.5 Effect of Evaporation Temperature

The figure 8 depicts the impact of varying the evaporation temperature on the coefficient performance of cycle, the cycle exergy efficiency and on the work produced in the turbine under following operated conditions the outlet pressure of turbine is equal to 12.261 kPa, the condensation temperature is equal to 30°C, the cooling capacity is equal 300 kW and the temperature of generation is equal to 120°C. It is clear that an augmentation in the evaporation temperature positively affected the coefficient performance of cycle and the cycle exergy efficiency contrary the work produced in the turbine. It can be explained this results by the increasing the evaporation temperature conducts an increasing the pressure of evaporation which is the pressure of secondly fluid of ejector as consequence the secondly fluid flow of ejector augmented contrary for primary ejector fluid flow which conducts to diminution in the turbine work produced and in the heat absorbed in the generator.

Figure 9 represents the effect of varying the evaporation temperature on the entrainment ration. It is clear that the entrainment ratio is positively affected with an augmentation of evaporation temperature. These results can

be explained by an increasing in the evaporation temperature conducts to augmentation of evaporation pressure which is the secondly fluid pressure of ejector. It well known that an augmentation of secondly fluid pressure of ejector conducts an augmentation of its mass flow. The same effect of evaporation temperature on the entrainment ratio is detected by Deng et al [40].

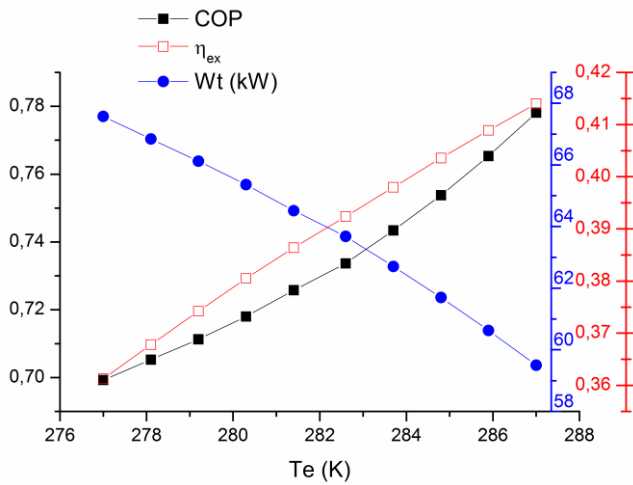


Figure 8. The effect of evaporation temperature on the coefficient of performance COP, The exergy efficiency and on the work produced in the turbine.

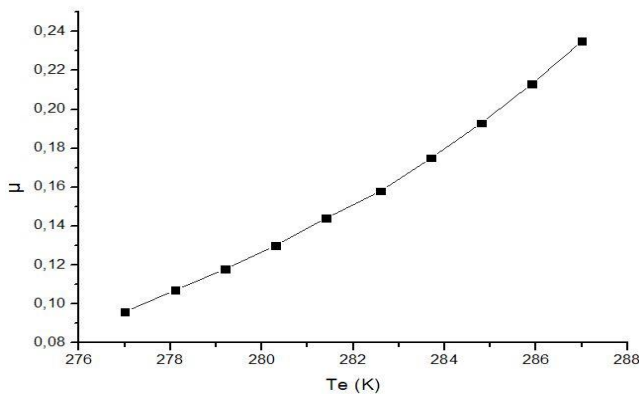


Figure 9. The effect of evaporation temperature on the entrainment ratio.

4.6 The Improvement of Exergy Efficiency

The proposed ejector power cooling absorption cycle efficiency improvement compared with the absorption simple effect, double effect and triple effect cycle Gomri [1] in various generation temperature, the evaporation temperature is equal to 4°C and the condensation temperature is equal to 39°C and the cooling capacity is equal to 300 kW presented in figure 10.

It is clear that for low grade temperature generation less than 100°C the proposed cycle has poor exergy efficiency because of low work produced in the turbine in comparing with the simple effect absorption cycle but the coefficient performance of proposed cycle is higher than its coefficient of performance. The proposed cycle has a high exergy efficiency in comparing with double and triple effect in middle range of generation temperature between 100 and 225 °C because of it has the same cooling capacity of double and triple effect absorption cycle adding up a respectable work produced in the turbine can be used to generate electrical power and the proposed cycle is very simple to realize end maintenance in comparing with

double and triple effect absorption cycle, in point of view practical.

Table 5 represent the maximum improvement of proposed cycle exergy efficiency compared with double and triple effect absorption cycle of ref [1]

The reason behavior that the proposed ejector assisted absorption cycle has high exergy efficiency that the exergy production of proposed cycle is more important that the double and triple effect is the proposed cycle has many advantages as like produce a work in the turbine added to cooling power, use smartly the ejector to have a gratuitous compression of water vapor from evaporation pressure to condensation pressure and low number of cycle component and simplicity of cycle which are important factor to reduce the exergy destruction of cycle.

It can be concluded that the proposed cycle is recommended for cycle working with generation temperature of waste heat source of industries or geothermal or renewable energy source upper than 100°C.

Table 5. The maximum improvement of proposed cycle exergy efficiency compared with double and triple effect absorption cycle.

T_g (°C)	Double effect Absorption Cycle [1]	Tripple effect Absorption Cycle [1]	Proposed cycle	Exergy efficiency Improvement
132.6	0.2453	-	0.3174	29.41 %
163	-	0.2529	0.3692	46 %

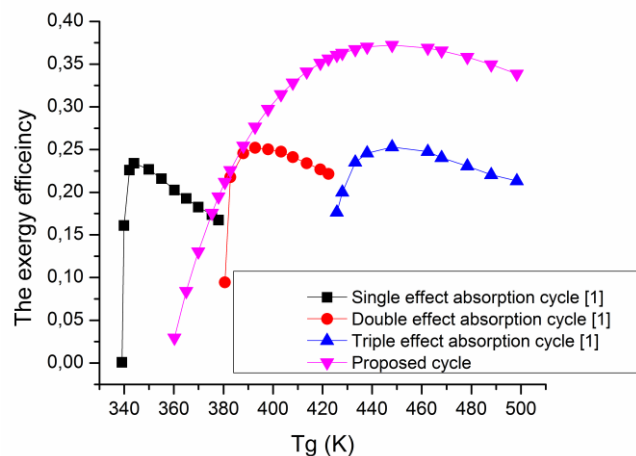


Figure 10. The comparison between the proposed cycle and the simple effect, double effect and triple effect exergy efficiency from ref [1].

5. Conclusions

A detailed numerical study of new proposed ejector assisted power cooling absorption cycle is carried out using first and second law of thermodynamic under often operating conditions used in the absorption cooling cycle. A constant mixing pressure model of ejector used in this simulation and its results validated with numerical and experimental data available in the literature. The analysis of simulation data of proposed cycle conducted to following conclusions:

- The increase of generation temperature is positively affected the work produced in the turbine contrary for coefficient performance of proposed cycle.
- For each operating conditions there is a certain value of generation temperature which is correspondence a maximum value of the cycle exergy efficiency.
- The increasing of pressure outlet of turbine is negatively

affected the work produced in the turbine and the cycle exergy efficiency contrary for the coefficient performance of proposed cycle and the entrainment ratio of the ejector.

- An increase in the condensing temperature leads to an increase in the work generated in the turbine and the cycle exergy efficiency and to a decrease in the coefficient of performance of the proposed cycle and the entrainment ratio of the ejector.
- An augmentation of evaporation temperature conducts an increasing of the coefficient performance, the exergy efficiency of proposed cycle and the entrainment ratio of ejector contrary for the work produced in the turbine.
- The proposed cycle is more efficiency in comparing with double and triple effect of absorption cycle for generation temperature superior of 100°C.
- The proposed cycle can be reaches 29.41 % and 46 % of exergy efficeincy improvement in comparaisn with double and triple effect absorption cycle under generation temperature 132.6 °C and 162 °C respectively.
- Despite that the exergy efficiency of proposed cycle is lower than simple effect of absorption cycle but the coefficient of performance of proposed cycle is higher than its coefficient of performance for generation temperature under 100°C.

A thermodynamic comparaisn of proposed cycle with simple, double and triple absorption effect is achieved in this paper but to make a final decision a technico economics study and analysis is required which will realize in the future works.

Nomenclature

COP	coefficient of performance of absorption cooling machine
η_{ex}	exergy efficeincy
Ex	exergy (kW)
h	enthalpy (kJ/kg)
x	mass fraction of lithium bromide by mass of solution (g/kg)
Q	heat transfert rate (kW)
S	Entropy (kJ/kg.K)
T	Temperature (K)
W_t	The turbine work produced (kW)
ρ	mass density (kg/m ³)
ε	efficiency
μ	entrainment ratio
Subscripts	
0	reference value
a	absorber
c	condenser
e	evaporator
g	generator
i	the ith chemical species
1,2,...,14	the state point number

References:

[1] R. Gomri, “ Investigation of the potential of application of simple and multiple effect absorption cooling systems,” *Energy Conver. Manag.*, 51, 1629-1636, 2010.

[2] N. Meng ,T. Li, X. Gao, Q. Liu, X. Li, H. Gao, “ Thermodynamic and techno-economic performance comparison of two-stage series organic Rankine cycle

and organic Rankine flash cycle for geothermal power generation from hot dry rock,” *Appl. Therm. Eng.*, 200, 117715 , 2022 .

[3] E. Cihan and B. Kavasogullari, “Energy and exergy analysis of a combined refrigeration and waste heat driven organic rankine cycle system,” *Therm. Sci.*, 21, No. 6A, 2621-2631, 2017.

[4] T. Li, H. Gao, X. Gao, N. Meng, “Thermodynamic performance comparison of organic Rankine flash cycle with and without ejector for geothermal power output,, *Appl. Therm. Eng.*, 214, 118846, 2022.

[5] S. Mondal, D. Sudipta, “Ejector based organic flash combined power and refrigeration cycle (EBOFCP&RC)–A scheme for low grade waste heat recovery,” *Energy*, 134, 638-648, 2017.

[6] S. Mondal, D. Sudipta, “ Performance assessment of a low-grade heat driven dual ejector vapour compression refrigeration cycle,” *Appl. Therm. Eng.*, 179, 115782, 2020.

[7] S. Mondal, C. Sahana, D. Sudipta, “Optimum operation of a novel ejector assisted flash steam cycle for better utilization of geothermal heat, ”, *Energy Conver. Manag.*, 253, 115164, 2022.

[8] A. M. Abed, H. SH. Majdi, K. Sopian, F. H. Ali, M. Al Bahrani, Q. R. Al Amir, A. K. Yakoob, “Techno-Economic Analysis of dual ejectors solar assisted combined absorption cooling cycle,” *Cas. Stud. Therm. Eng.* , 39, 102423, , 2022.

[9] T. Hai, M. A. Ali, H. A. Dhahad, A. Alizadeh, K. Sharma, S. F. Almojil, A. I. Almohana, A. F. Alali, E. Attia, “A novel bi-evaporator cooling system via integration of absorption refrigeration cycle for waste energy recovery from an ejector-expansion trans-critical CO2 (EETRCC) cycle: Proposal and optimization with environmental considerations,” *Sustain. Energy Technol. Assess.*, 57, 103118, 2023.

[10] S. khalili, L. G. Farshi, “Design and performance evaluation of a double ejector boosted multi-pressure level absorption cycle for refrigeration,” *Sustain. Energy Technolo. Assess.*, 42, 100836, 2020.

[11]K. H. M. Al Hamed, I. Dincer, “Investigation of a concentrated solar-geothermal integrated system with a combined ejector-absorption refrigeration cycle for a small community,” *Int. J. of Refr.*, 106, 407-426, 2019.

[12] S. Göktun,“ Optimal performance of a combined absorption and ejector refrigerator,” *Energy Conver. Manag.*, 40, 51-58, 1999.

[13] H. S. Majdi,“ Performance evaluation of combined ejector LiBr/H2O absorption cooling cycle,” *Cas. Stud. Therm. Eng.*, 7, 25-35, 2016.

[14] L. Jiang, Z. Gu, X. Feng, Y. Li, “Thermo-economical analysis between new absorption–ejector hybrid refrigeration system and small double-effect absorption system,” *Appl. Therm. Eng.*, 22, 1027-1036, 2022.

[15] R. Sirwan, M. A. Alghoul, K. Sopian, Y. Ali, “ Thermodynamic analysis of an ejector- flash tank-absorption cooling system,” *Appl. Therm. Eng.*, 58, 85-97, 2013.

- [16] A. Sözen, Ö. Mehmet, “ Performance improvement of absorption refrigeration system using triple-pressure-level,” *Appl. Therm. Eng.*, *23*, 1577-1593, 2003.
- [17] A. M. Abed, J. Huang, S. M. Eldin, Y. Aryanfar, J. L. G. Alcaraz, “ Exergy analyses and optimization of a single flash geothermal power plant combined with a transcritical CO₂ cycle using genetic algorithm and Nelder-Mead simplex method,” *Geotherm. Energy*, *11*, 4, 2023.
- [18] S. Yi, Z. Zhang, W. Peng, J. Zhang, H. Yuan, “ Pre-expansion ejector absorption power cycle for ocean thermal energy conversion,” *Energy Conver. manag.*, *269*, 116151, 2022.
- [19] A. Bhowmick ,B. Kundu, “Extremum analysis based on exergy and economic principle for ejector-absorption cycles combined with regenerative organic-Rankine and gas-turbine cycles,” *Energy Conver. Manag.*, *253*, 115174 , 2022.
- [20] S.KhaliliL, G. Farshi, “Design and performance evaluation of a double ejector boosted multi-pressure level absorption cycle for refrigeration,” *Sustain. Energy Technol. Assess.* , *42*, 2020.
- [21] D. Sioud, M. Bourouis, A. Bellagi, “Investigation of an ejector powered double-effect absorption/recompression refrigeration cycle,” *Int. J. of Refr.*, *99*, 453-468, 2019.
- [22] C. Vereda, R. Ventas, A. Lecuona, M. Venegas, “ Study of an ejector-absorption refrigeration cycle with an adaptable ejector nozzle for different working conditions,” *Appl. Energy*, *97*, 305-312, 2012.
- [23] Y. Tang, Z. Liu, Y. L. F. Zhao, P. Fan, K. J. Chua, “Mixing process of two streams within a steam ejector from the perspectives of mass, momentum and energy transfer,” *Appl. Therm. Eng.*, *185*,116358, 2021.
- [24] T. Thongtip, S. Aphornratana, “An experimental analysis of the impact of primary nozzle geometries on the ejector performance used in R141b ejector refrigerator,” *Appl. Therm. Eng.*, *110*, 89-101, 2017.
- [25] L. Wang, J. Yan ,C. Wang, X. iLi, “Numerical study on optimization of ejector primary nozzle geometries,” *Int. J. of Refr.*, *76*, 219-299, 2017.
- [26] V. Nguyen, S. Varga, J. Soares, V. Dvorak, A. C. Oliveira, “Applying a variable geometry ejector in a solar ejector refrigeration system,” *Int. J. of Refr.*, *113*, 187-195, 2020.
- [27] Y. H. Liu, “ Experimental and numerical research on high pumping performance mechanism of lobed exhaust-ejector mixer,” *Int. Communi. Heat and Mass Transf.*, *34*, 197-209, 2007.
- [28] B. Kavasogullari, E. Cihan, H. Demir , “ Energy and Exergy Analyses of a Refrigerant Pump Integrated Dual-Ejector Refrigeration (DER) System,” *Arab. J. Sci. Eng.*, *46*, 11633–11644 , 2021.
- [29] S. Varga, A. C. Oliveira, B. Diaconu, “ Influence of geometrical factors on steam ejector performance – A numerical assessment,” *Int. J. of Refri.*, *32*, 1694-1701, 2009.
- [30] T. siveerakul, S. Aphornratana, K. chunnanond, “Performance prediction of steam ejector using computational fluid dynamics: Part 2. Flow structure of a steam ejector influenced by operating pressures and geometries,” *Int. J. of Therm. Sci.*, *46*, 823-833, 2007.
- [31] K. Ariafar, “ Performance evaluation of a model thermocompressor using computational fluid dynamics,” *Int. J. of Mech.*, *6*, 35-42, , 2012.
- [32] X. Li, X. Wang, Y. Zhang, L. Fang, N. Deng, Y. Zhang, Z. Jin, X. Yu, S. Yao, “ Experimental and economic analysis with a novel ejector-based detection system for thermodynamic measurement of compressors,” *Appl. Energy*, *261*, 1 ,114395, 2020.
- [33] B. Tashtoush, Y. Nayfeh, “ Energy and economic analysis of a variable-geometry ejector in solar cooling systems for residential buildings”, *J. of Energy Storage*, *27*, 101061, 2020.
- [34] B. J. Huang, J. M. Chang, C. P. Wang, and V. A. Petrenko, “A 1-D analysis of ejector performance,” *Int. J. of Refr.*, *22*, 354-364, 1999.
- [35] H. Keenan, E. P. Neumann, F. Lustwerk, “An investigation of ejector design by analysis and experiment, ” *J. Appl. Mech., Trans. ASME*, *72*, 299-309, 1950.
- [36] V. Kumar, K. Yadav, S. Ram, “A comprehensive studies on constant area mixing (CAM) and constant pressure mixing (CPM) Ejectors: A review,” *Materials Today Proceedings*, DOI: <https://doi.org/10.1016/j.matpr.2022.09.258>.
- [37] Y. Cheng, M. Wang, J. Yu, “Thermodynamic analysis of a novel solar-driven booster-assisted ejector refrigeration cycle,” *Sol. Energy*, *218*, 85-94, 2022.
- [38] J. Patek, J. Klomfar, “A computationally effective formulation of the thermodynamic properties of LiBr–H₂O solutions from 273 to 500 K over full composition range”, *Int. J. of Refr.*, *29*, 566-578, 2006.
- [39] J. Patek, J. Klomfar , “A simple formulation for thermodynamic properties of steam from 273 to 523 K, explicit in temperature and pressure,” *Int. J. of Refr.*, *32*, 1123-1125, 2009.
- [40] J. Q. Deng, P. X. Jiang, T. Lu, W. Lu, “Particular characteristics of transcritical CO₂ refrigeration cycle with an ejector,” *Appl. Therm. Engi.*, 381-388, 2007.

Research Article

Performances Investigation of the Eco-friendly Refrigerant R131I used as Working Fluid in the Ejector-Expansion Refrigeration Cycle

¹Y.Maalem , ^{2*}Y.Tamene , ³H.Madani 

^{1,2,3} Laboratory of Studies of Industrial Energy Systems (LESEI), Department of Mechanical Engineering, Faculty of Technology, University of Batna 2, 05000 Batna, Algeria
E-mails: ¹y.maalem@univ-batna2.dz, ^{2*}y.tamene@univ-batna2.dz, ³h.madani@univ-batna2.dz

Received 12 March 2023, Revised 27 May 2023, Accepted 5 July 2023

Abstract

Knowing that from 2030 refrigerants used in refrigerating engineering should have a global warming potential (GWP) of less than 150. Searching for eco-friendly refrigerants with good performance and minimal environmental impact to substitute conventional working fluids such as R134a (GWP=1430) represents a great challenge for researchers. The present research aims to investigate and compare the performances of the eco-friendly refrigerant R131I (Zero GWP) used as a possible new working fluid in the ejector-expansion refrigeration cycle (EERC) with the commonly used R134a which has good performances but a high GWP. To reach this objective, a numerical program was developed using MATLAB software to evaluate the coefficient of performance (COP), the entrainment ratio (μ), the exergy destruction and the exergy efficiency for both refrigerants. Furthermore, the effect of the diffuser efficiency of the ejector on the COP and the compressor work was explored. Furthermore, the effect of the diffuser efficiency of the ejector on the COP, and the compressor work were explored. The simulation was realized for T_c selected between 30 and 55 °C and T_e ranging between -10 and 10 °C. Results proved that the use of R131I as a working fluid in the EERC system exhibited a higher COP, μ , and exergy efficiency, as well as lower exergy destruction compared with R134a under the same operating temperatures. On another hand, the energetic analysis revealed that as T_c increases the COP and μ decrease. However, as T_e varies from -10 and 10 °C, the COP and μ increase. Regarding exergy analysis, it should be noted that both exergy destruction and exergy efficiency are sensitively influenced by T_c more than T_e . Overall, the study confirms that R131I could be a suitable substitute for the phase-out R134a in terms of performance and environmental protection.

Keywords: R131I working fluid; zero GWP; ejector; coefficient of performance; entrainment ratio; exergy efficiency.

1. Introduction

The search for alternative refrigerants to substitute the traditional refrigerants which have a high global warming potential (GWP) is based on two major prerogatives: having good performances and a low environmental impact. According to the restrictive regulations by the international agreements Montreal (1987) and the Kyoto (1997) protocols, and the European (F-gas) regulation, the fluoride substances: chlorofluorocarbons (CFCs), hydrochlorofluorocarbons (HCFCs) and hydrofluorocarbons (HFCs) widely used in the applications of the thermodynamic machines such as heat pump, air-conditioning and refrigeration systems, would be phased out because of their great impact on the environment and their contribution to the atmospheric greenhouse [1,2]. The Paris climate convention adopted on 4 November 2016, makes the research for sustainable refrigerants that can answer the environmental concern and the demand for cooling efficiency a pressing priority.

Currently, seeking alternative work fluids to meet environmental requirements, as well as more efficient refrigeration systems has become an important research topic in refrigeration engineering. Furthermore, the development of new technologies for performance enhancement of the conventional mechanical vapor compression refrigeration

cycle (CMVCRC) by diverse cycle changes has acquired a particular interest newly. Accordingly, several modifications have been proposed in the mechanical single-stage vapor compression systems to improve their energy efficiency and reduce power consumption with different working fluids.

One of the most recent effective ways that have noticeable benefits is the ejector expansion technology. The use of an ejector apparatus as the expansion valve instead of a classical expansion valve reduces throttling mechanism losses by recovering expansion work, additionally, its design and build are inexpensive and it has low maintenance requirements [3]. An ejector expansion device, which consists of a motive nozzle, suction nozzle, mixing section and diffuser is able of converting the kinetic energy of the expansion operation to pressure flow work, increasing compressor absorption pressure to a level higher than that in the evaporator and consequently reducing the power consumption of the compressor and improving the performance of the mechanical refrigeration system. With the introduction of the technology of ejector expansion in the cooling systems to improve their cooling efficiency for the first time by Kornhauser in 1990 [4], studies in this area have seen a growing trend, where many numbers of academic researchers have performed investigations both numerically

and experimentally with different working fluids[5]. It is also found from the literature reviews that the preceding ejector-expansion refrigeration cycle (EERC) works are usually related to pure fluid: CFCs [6,7], HCFCs [7], HFCs [7-9], natural fluids such as carbon dioxide (R744) [10-12] and hydrocarbon (Propane (R290)[13], Butane (R600), Propane (R290), Isobutane (R600a) and Propylene (R1270) [14] or zeotropic blends like (R245fa/R134a) [15], (R290/R170) [16], R410A [17],(R134a/R143a) [18] and (R290/R600a) [19].

Due to the increased environmental consciousness, the traditional refrigerants CFCs, HCFCs and HFCs would be phased out and the hydrocarbons have potential safety hazards in applications owing to their flammable and explosive properties. Furthermore, although R744 fluid is ecofriendly, it undergoes high running pressure and relatively low performance, which results in a ponderous and expensive refrigeration machine. In addition, the zeotropic blends exhibit various problems in the cooling cycles (CMVCRC, EERC) due to their behavior compared to the single-fluids such as mole fraction difference of the vapor to liquid and temperature variation during constant pressure phase change, they present also a low coefficient of performance[20-22,3], this can be induced by the delay of the liquid-vapor equilibria such as overheating or undercooling, which results from the temperature change during the cooling process (temperature glides) [20]. The dilemma for the refrigeration industry is finding a new working fluid in the EERC system that can meet the requirements of environmental properties, safety and high performance at the same time.

On the other hand, there is recently a renewed interest in the use of Trifluoriodomethane (R131I) refrigerant as the working fluid in the thermodynamic systems of the production units [23,24], however studies on the EERC system using R131I as working fluid in the field of refrigeration were not found in the literature. While this fluid has excellent thermo-physical properties [25] like R134a, good safety, and negligible environmental impact [Zero Ozone Depletion Potential (ODP=0), Zero Global Warming Potential (GWP=0)] [26], so it can be considered as an alternative refrigerant. Considering the increasing restrictions imposed by the international Montreal and Kyoto protocols, the refrigerant can be selected as a possible new working fluid in the EERC system and can be recommended as a good candidate for replacing the above working fluids and especially the phase-out R134a (HFC), which is widely used in EERC system, due to its good performances in the EERC system, unfortunately, it has high global warming potential (GWP=1430).


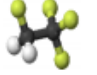


As far as the authors are aware, no previous study has found an appropriate pure substance with high performances (such as COP) in the EERC system to replace R134a and can meet the requirements of environmental properties, thermo-physical properties and high performance at the same time. This study is conducted for this purpose.

The eco-friendly R131I, which has good characteristics in terms of thermo-physical properties and environmental protection, has not been used before in the EERC system, and there is no published literature about comparison between the thermodynamic performances of R131I and R134a at present. Therefore, the present study aims to investigate theoretically the performance of the EERC system in terms of coefficient of performance (COP), entrainment ratio (μ), exergy destruction and exergy

efficiency using the eco-friendly R131I refrigerant as a substitute to the traditional R134a fluid.

The fundamental environmental and thermodynamic properties of the investigated refrigerants are shown in Table 1 [26-28].

Table 1. Physical and environmental properties of investigated refrigerants.

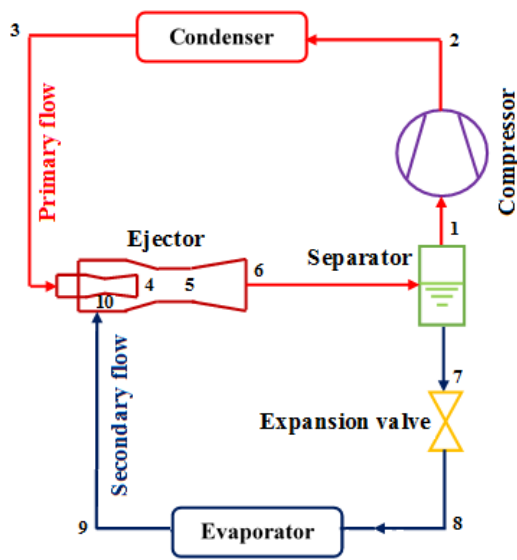
Refrigerants	R131I	R134a
Cas N°	2314-97-8	811-97-2
Molecular formula	CF ₃ I	C ₂ H ₂ F ₄
Molecular structure		
Chemical structure		
Molar mass (kg/kmol)	195.91	102.03
Critical temperature (K)	396.44	374.21
Critical pressure (MPa)	3.9530	4.0593
Normal boiling point (K)	251.3	247.08
GWP	0	1430
ODP	0	0

The thermodynamic properties of the working fluids greatly affect the cycle performances. So, to investigate an alternative refrigerant that gives suitable performances similar to the existing refrigerant R134a in the EERC system, the thermodynamic and environmental properties should be taken into account. As illustrated in Table 1, the values indicate that R131I has similar thermodynamic properties to that of R134a such as the normal boiling point and the critical pressure. The high normal boiling point has an effect on the latent heat of vaporization whereas the high normal boiling point makes a greater latent heat of vaporization and as a result, the refrigerating effect increases. About the critical temperature, the R131I has a critical temperature much higher than that of R134a, which makes a greater heat transfer. In terms of environmental friendliness, environmental properties are discussed in the paragraphs above. In overall, the working fluid R131I has good thermodynamic and environmental properties.

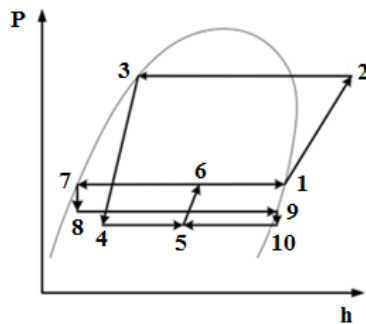
To reach the objectives of this study, a numerical model based on the energetic and exergetic methods of the EERC system is developed and validated to compare the performances of the eco-friendly refrigerant R131I with the usually used fluid R134a in the EERC system under the same operating parameters. The thermodynamic performances studied include the coefficient of performance (COP), the entrainment ratio (μ), the exergy destruction, and the exergy efficiency. Furthermore, the influences of evaporator and condenser temperatures on the EERC system performances and the effect of the isentropic efficiency of the diffuser section on the COP and the compressor work are also examined and discussed.

2. Description of EERC System

A general illustration of the configuration (Figure 1(a)) and the corresponding pressure-enthalpy (P-h) diagram (Figure 1(b)) of the EERC system is presented in Figure 1.



(a)



(b)

Figure 1. Configuration (a) and (P-h) diagram (b) of the (EERC) system [29].

The studied system includes six components that are: a compressor, a condenser, an ejector, an evaporator, a throttle valve and a liquid-vapor separator.

The processes of the EERC system can be described as follows: the working fluid in the form of saturated vapor enters the compressor at pressure P_1 (state 1) where it is compressed to high pressure up to pressure P_2 (1→2). The refrigerant in the superheated state (state 2) thus obtained is cooled in the condenser to the temperature corresponding to state 3 (2→3). This constitutes the primary flow (primary fluid) which enters the primary nozzle of the ejector expansion device; and then undergoes an expansion in this nozzle (3→4). At the outlet (state 4), the primary fluid (motive flow) drives the secondary fluid at lower pressure from the evaporator (state 10). Then the primary and secondary streams mix in the mixing section (state 5). The mixed flow at the end of the mixing section at state 5 enters the diffuser section where its velocity drops and pressure increases. On leaving the ejector (state 6), the mixture goes to a separator which divides the two phases (liquid-vapor) of the mixture. At last, the saturated vapor in state 1 is sucked by the compressor while the saturated liquid in state 7 passes through an expansion valve (7→8) before entering the evaporator to produce cold (8→9) and completes the cycle.

3. System Modeling and Assumptions

3.1 Assumptions

For the sake of simplification of the thermodynamic analysis of the EERC system, the following assumptions were made [30,31]:

- The heat loss from the ejector expansion device, condenser, compressor, separator, evaporator and expansion is negligible;
- The flow inside the ejector is one-dimensional and homogeneous;
- The velocities of the refrigerant are negligible at the inlets and outlet of the ejector;
- Mixing operation of the primary and secondary fluids in the ejector device occurs at constant pressure ($P = \text{constant}$);
- The ejector component efficiencies (η_{mn} , η_{sn} , η_{ms} and η_d) keep constant;
- The working operation in the ejector complies with the conservations of mass, momentum and energy;
- Pressure drops in piping, heat exchangers and separator are neglected;
- The refrigerant leaving the condenser, the evaporator and the separator outlet is saturated;
- The compressor has a given specified isentropic efficiency;
- Flow across the expansion valve is isenthalpic ($h = \text{constant}$).

3.2 Numerical Tools and Theoretical Analysis of EERC

3.2.1 Ejector Analysis Model

The ejector expansion device plays an important role in the EERC system where the latter is strongly dependent on the performance of this device. So the prediction of the ejector performance is very important for the refrigeration system behavior thermodynamic modelling.

Presently, the thermodynamic studies for ejector simulation are fundamentally categorized into two models: the constant-area model and the constant mixing pressure model. Several academic studies in the open literature showed that the constant-pressure mixing model gives better results than the constant-area model [5,32-34]. So, in the present study, the constant-pressure mixing model was employed (Figure 2) to conduct performance analysis.

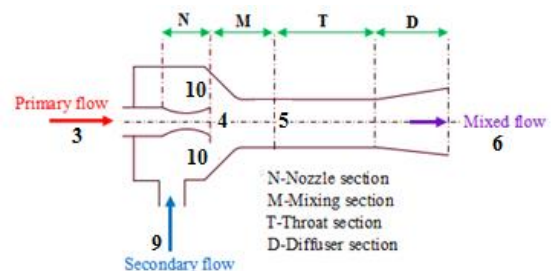


Figure 2. Configuration of constant-pressure mixing ejector.

The entrainment ratio (μ) of the ejector is the key parameter to assess its performance, which is defined as the ratio between the mass flow of refrigerant of the secondary (m_9) and the primary (m_3) leaving from the evaporator and the condenser respectively in the ejector.

It is given as [30-31]:

$$\mu = \frac{m_9}{m_3} \quad (1)$$

Using the mentioned assumptions previously, for thermodynamic modeling of the ejector device the procedure presented by Li et al [30] and Sarkar [31] was followed, and the states of each point of this equipment were calculated using the principle of conservation of mass, momentum and energy.

The modeling begins by determining the states parameters of the primary and secondary flows leaving from the condenser and evaporator respectively to the ejector.

Based on the above analysis, the system equations for ejector can be formulated as follows:

For the motive nozzle outlet:

$$p_4 = p_9 - \delta p \quad (2)$$

$$h_{4,is} = p(p_4, s_3) \quad (3)$$

$$h_4 = h_3 - \eta_{mn}(h_3 - h_{4,is}) \quad (4)$$

$$u_4 = \sqrt{2(h_3 - h_4)} \quad (5)$$

At the suction nozzle outlet, the following equations can be applied:

$$p_{10} = p_4 \quad (6)$$

$$h_{10,is} = p(p_4, s_9) \quad (7)$$

$$h_{10} = h_9 - \eta_{sn}(h_9 - h_{10,is}) \quad (8)$$

$$u_{10} = \sqrt{2(h_9 - h_{10})} \quad (9)$$

For the mixing section:

At the ejector mixing chamber, the mixing process is done at a constant pressure.

Applying the momentum and energy conservations on the mixing chamber would result relations for its exit velocity and enthalpy.

$$p_5 = p_{10} \quad (10)$$

$$u_5 = \sqrt{\eta_{ms} \left(\frac{1}{(1+\mu)} u_4^2 + \frac{\mu}{(1+\mu)} u_{10}^2 \right)} \quad (11)$$

$$h_5 = \frac{1}{(1+\mu)} \left(h_4 + \frac{u_4^2}{2} \right) + \frac{\mu}{(1+\mu)} \left(h_{10} + \frac{u_{10}^2}{2} \right) - \frac{u_5^2}{2} \quad (12)$$

$$s_5 = s(h_5, p_5) \quad (13)$$

For the diffuser outlet, it can be written:

$$h_6 = h_5 + \frac{u_5^2}{2} \quad (14)$$

$$h_{6,is} = h_5 + \eta_d(h_6 - h_5) \quad (15)$$

$$p_6 = p(h_{6,is}, s_5) \quad (16)$$

$$x_6 = x(h_6, p_6) \quad (17)$$

To verify the preliminary input value for the entrainment ratio (μ), the following relationship of the quality (x_6) outlet must be satisfied:

$$x_6' = \frac{1}{1+\mu} \quad (18)$$

3.2.2 Energy Analysis Model

The energy balance equations for system components are established as follows [30]:

The specific cooling (q_{evap}) of the EERC is expressed as:

$$q_{evap} = \frac{\mu(h_9 - h_8)}{1+\mu} \quad (19)$$

The compressor work (w_{comp}) can be expressed as:

$$w_{comp} = \frac{(h_2 - h_1)}{1+\mu} \quad (20)$$

With :

$$h_2 = h_1 + \frac{h_{2,is} - h_1}{\eta_{comp}} \quad (21)$$

Where η_{comp} is the isentropic efficiency of the compressor, which is closely related to the compression ratio, given as [35]:

$$\eta_{comp} = 0.874 - 0.0135\pi \quad (22)$$

The thermodynamic performance EERC system is evaluated by its coefficient of performance, which reflects the cycle performance and is the major criterion for selecting a new refrigerant as a substitute.

The coefficient of performance is defined as the ratio of the specific cooling to the consumption of compressor work (specific work):

$$COP = \frac{q_{evap}}{w_{comp}} \quad (23)$$

Then, the improvements in COP of the EERC over the conventional mechanical cycle (basic cycle) are determined using the following equation:

$$COP_{imp} = \frac{COP - COP_{BC}}{COP_{BC}} \quad (24)$$

3.3.3 Exergy Analysis Model

For the EERC system, exergy analysis enables the evaluation of the contribution of the irreversibility of each

device in the system. Furthermore, exergy analysis can also help to evaluate the improvement degree in the exergy efficiency in comparison with the conventional cycle.

For the exergy analysis, the procedure presented by Zhang et al [36] and Ma et al [14] was used. It is assumed that the chemical exergy and kinetic and potential exergies are ignored, and only the physical exergy is considered.

For the refrigerant flowing in a refrigerating system, the specific exergy at any state points is expressed as follows:

$$Ex = (h - h_0) - T_0(s - s_0) \quad (25)$$

For q at constant temperature T , the heat exergy rate Ex_q can also be calculated by:

$$Ex_q = \left(1 - \frac{T_0}{T}\right)q \quad (26)$$

The exergy destruction for the components: compressor, condenser, ejector, expansion valve and evaporator in EERC system is calculated from the following relationships:

In the compressor:

$$Ex_{comp} = T_0(s_2 - s_1) \quad (27)$$

In the condenser:

$$Ex_{cond} = h_2 - h_3 - T_0(s_2 - s_3) \quad (28)$$

In the ejector:

$$Ex_{ej} = T_0((1 + \mu)s_6 - s_3 - \mu s_9) \quad (29)$$

In the throttle valve:

$$Ex_{tv} = T_0(s_8 - s_7) \quad (30)$$

In the evaporator:

$$Ex_{evap} = T_0\mu[(s_9 - s_8) + (h_8 - h_9)/T_r] \quad (31)$$

Where $T_r = T_e + 5$ [14]

The total exergy destroyed of the EERC system is the sum of exergy destruction in each element of the cycle is by the following equation:

$$Ex_{Tot} = Ex_{comp} + Ex_{cond} + Ex_{ej} + Ex_{tv} + Ex_{evap} \quad (32)$$

The exergy efficiency of the EERC system is calculated by:

$$\eta_{ex} = 1 - \frac{Ex_{Tot}}{w_{comp}} \quad (33)$$

The decrease in Ex_{Tot} and improvement in exergy efficiency of the EERC system over the conventional mechanical cycle are [14, 36] :

$$Ex_{Tot,imp} = \frac{Ex_{Tot,EERC} - Ex_{Tot,BC}}{Ex_{Tot,BC}} \quad (34)$$

$$\eta_{ex,imp} = \frac{\eta_{ex,EERC} - \eta_{ex,BC}}{\eta_{ex,BC}} \quad (35)$$

Based on the mathematical model built above, a computer program was developed in MATLAB and the refrigerants thermodynamic properties were obtained using REFPROP Version 9.0 to investigate the performance potential of the EERC system in a wide range of working conditions using the working fluids R131I and R134a.

The detailed flowchart for the EERC system calculation procedure is presented in Figure 3.

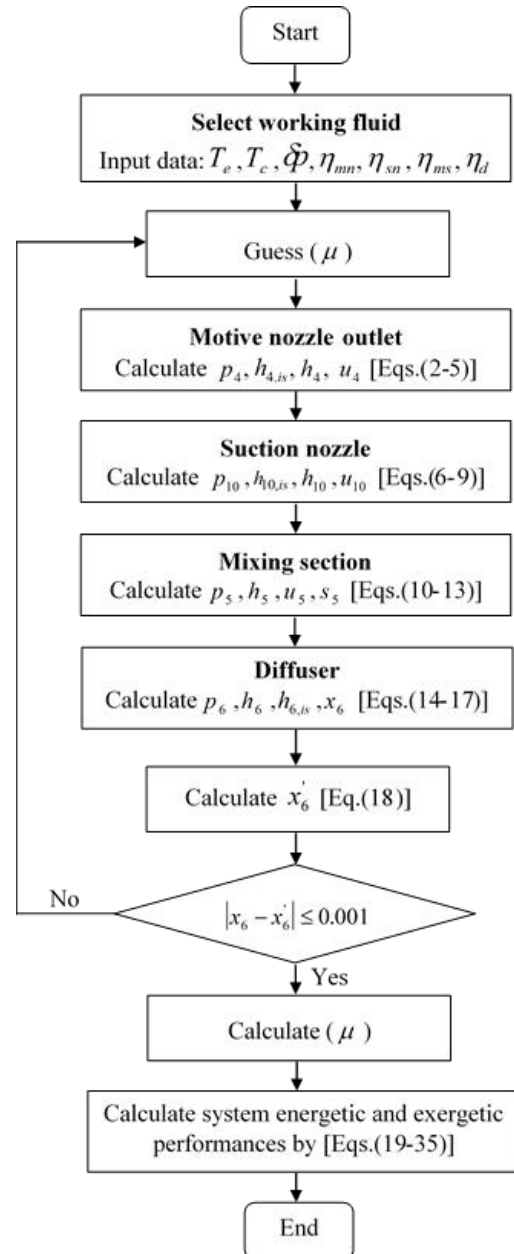


Figure 3. Flowchart for EERC cycle calculation procedure.

4. Results and Discussion

4.1 Validation With the Literature Data

Before using the developed program to evaluate the performance of the EERC system using eco-friendly R131I refrigerant, the program was validated by comparing the

values of the maximum COP reported by Li et al [30] and Sarkar [31] using the refrigerant R600a (Isobutane) as working fluid under the same operating conditions (condensation temperatures (T_c) vary from (35 to 55 °C) and the constant evaporation temperature (T_e) of 5°C).

The simulation results are illustrated in Figure 4 for different condenser temperatures.

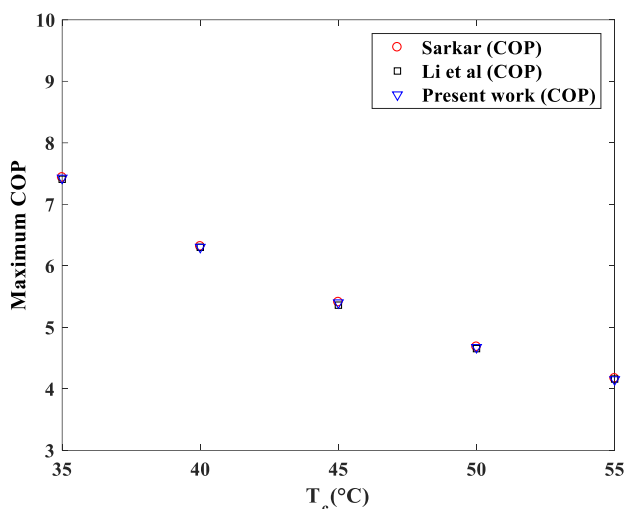


Figure 4. Validation of the present work results with those of [30, 31] results.

As can be seen, the values of the maximum COP of the refrigeration system (EERC) calculated using the developed program indicate a very good agreement with those of [29, 30], which confirms the validity of our simulation model.

4.2 Performance Characteristics of EERC

To explore the thermodynamic performances of the EERC system using eco-friendly R131I (Trifluoroiodomethane) refrigerant, the energetic and exergetic performances were made in the following working conditions: The condensing temperature is set at (40 °C) when T_e vary, and when T_c vary; the evaporating temperature is set at (5 °C). The ejector component efficiencies (motive nozzle (η_{mn}), suction nozzle (η_{sn}), mixing section (η_{ms}) and diffuser (η_d) are assumed to be constant at: ($\eta_{mn} = \eta_{sn} = \eta_d = 0.85$ and $\eta_{ms} = 0.95$) [34]. The reference environment temperature is set at 27 °C [36,37].

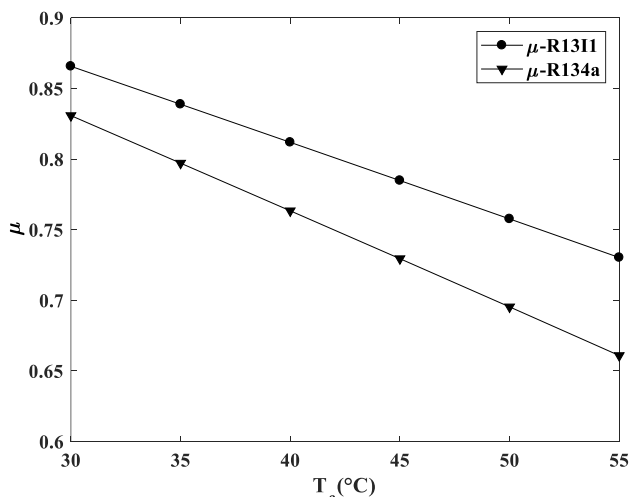


Figure 5. Influence of condensing temperature on μ .

Based on the model developed, the performances of EERC is investigated using R131I and compared with those of the traditional R134a refrigerant for various condensing temperature (30 to 55 °C) and evaporation temperature (-10 to 10 °C).

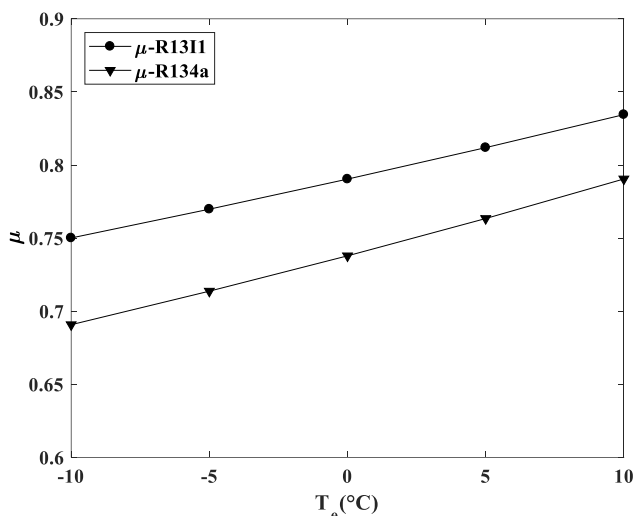


Figure 6. Influence of evaporating temperature on μ .

Figures 5 and 6 give the simulation results of the variation of the entrainment ratio (μ) values of the EERC system for both working fluids versus the condensing temperature (T_c) and the evaporating temperature (T_e), respectively.

It is noticed from the figures that the operating temperatures (T_c and T_e) has a great effect on the (μ). It could be observed that the (μ) of R131I and R134a increases with the evaporation temperatures which vary from -10 to 10 °C at a constant condensation temperature of 40 °C, and decreases with the condensation temperatures varying from 30 to 55 °C at a constant evaporation temperature of 5 °C. This is due to the fact that when the (T_e) rises from -10 to 10 °C, the primary mass flow rate (m_3), leaving from the condenser decreases, and the secondary mass flow rate (m_9), leaving from the evaporator increases, and hence the entrainment ratio (μ) increases.

The entrainment ratio (μ) is a function of the power consumption of the compressor and working fluids effect, so it directly affects the coefficient of performance of the EERC system.

On the other hand, when T_c raises from 30 to 55 °C, the primary mass flow rate (m_3), leaving from the condenser increases, and the secondary mass flow rate (m_9), leaving from the evaporator decreases, and hence the entrainment ratio (μ) decreases.

Compared with the traditional R134a refrigerant which has high GWP, the eco-friendly R131I refrigerant offers higher entrainment ratio (μ) than that of the R134a under the same operating temperatures (T_c and T_e).

The (μ) values calculated of the R131I and R134a decrease from (0.8657 to 0.7303) and from (0.8308 to 0.6609), respectively, as the (T_c) increases from (30 to 55 °C) as it can be observed from Figure 5. However, the (μ) values calculated of the R131I and R134a increase from (0.7501 to 0.845) and from (0.6908 to 0.7905), respectively, as the (T_e) increases from (-10 to 10 °C) as it can be observed from Figure 6.

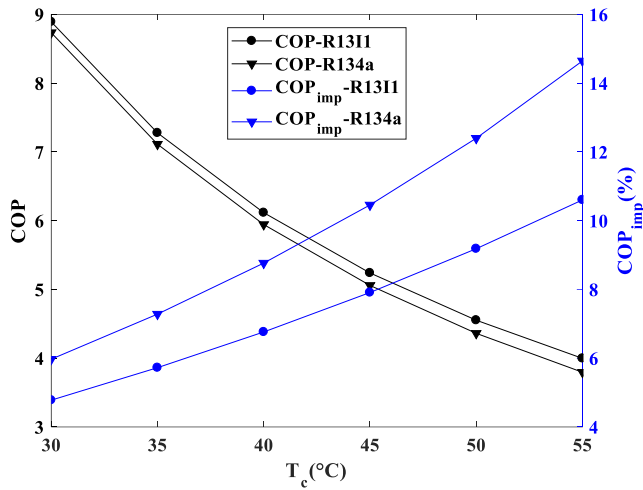


Figure 7. Influence of condensing temperature on COP and COP_{imp} .

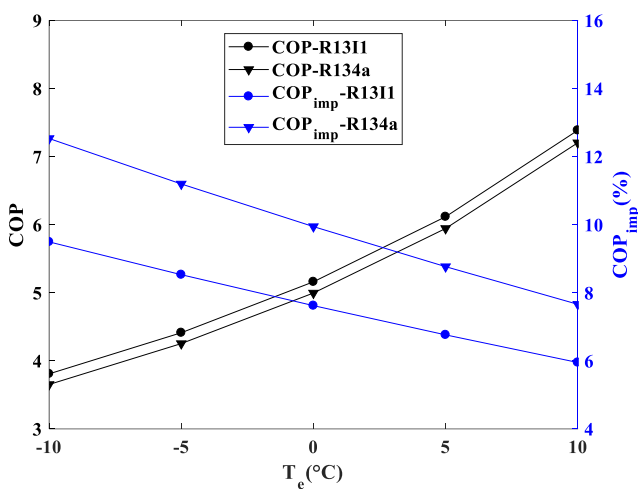


Figure 8. Influence of evaporating temperature on COP and COP_{imp} .

The simulation results of performance evolution of the EERC system, based on the maximum COP for both refrigerant R131I and R134a with the condensation temperatures (T_c) varying from 30 to 55 °C and with constant evaporation temperature of 5 °C and evaporation temperatures (T_e) varying from -10 to 10 °C with constant condensation temperature of 40 °C are shown in Figures 7 and 8, respectively.

The coefficient of performance can be defined as an energy efficiency index of the cooling equipment. It is clear that both curves of the coefficient of performance (COP) of the examined working fluids (R131I and R134a) decrease with the (T_c) and increase with the (T_e). This case can be interpreted by as the condenser exit temperature increases, the enthalpy of the working fluids (R131I and R134a) at the inlet to the evaporator increases. Meanwhile, the evaporator exit enthalpy remains constant and hence causing a low cooling effect and low coefficient of performance (COP). However, as the evaporator exit temperature increases, the pressure difference between the nozzle exit and the evaporator (p_9-p_4) increases. This has resulted in an increase in the secondary flow rate and hence, the COP and cooling capacity of the system have also increased. In addition, the reason for the COP increase or decrease is also due to that the COP is directly proportional to the ejector entrainment ratio.

On other hand, we can find that the benefit of the ejector is increased (higher COP_{imp}) at higher condensing temperatures (T_c) or lower evaporating temperatures (T_e) owing to the greater potential for expansion work recovery for the two fluids.

Compared with the traditional R134a refrigerant, this result reveals that the eco-friendly R131I refrigerant has a higher coefficient of performance which occurs due to its better thermodynamic properties and exhibited a lower coefficient of performance improvements (COP_{imp}) over the basic cycle for all studied temperatures T_c and T_e range.

The COP values calculated of the examined working fluids R131I and R134a decrease from 8.893 to 3.997 and from 8.735 to 3.795, respectively, as the (T_c) increases from 30 to 55 °C. However, they increase from 3.809 to 7.386 and from 3.652 to 7.203, respectively, as the (T_e) increases from -10 to 10 °C.

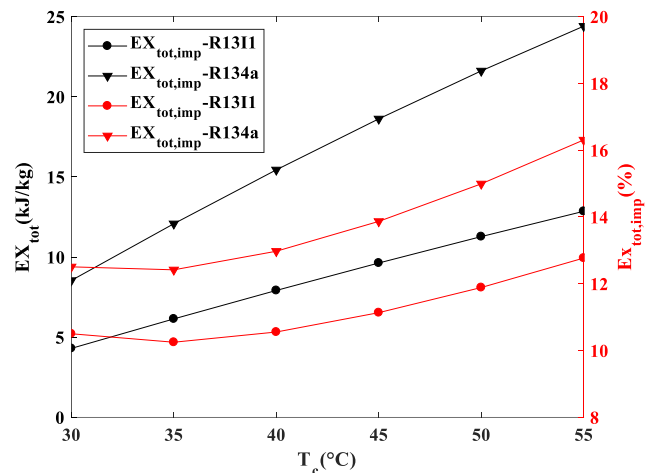


Figure 9. Influence of condensing temperature on Ex_{tot} and $Ex_{tot,imp}$.

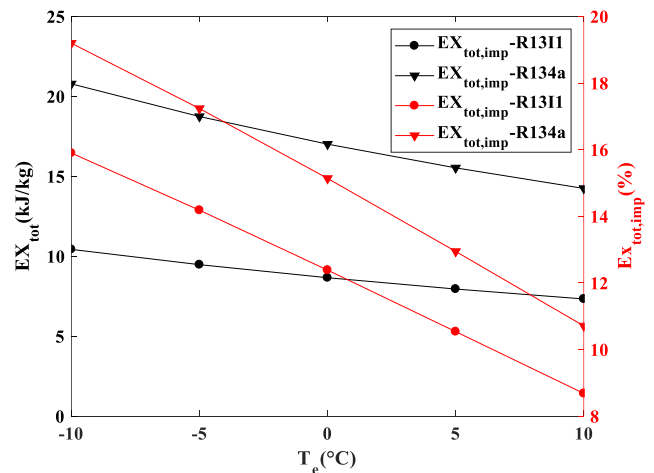


Figure 10. Influence of evaporating temperature on Ex_{tot} and $Ex_{tot,imp}$.

Figures 9 and 10 display the effect of the studied range of the condensing temperature ($T_c= 30$ to 55 °C with $T_e=5$ °C) and the evaporating temperature ($T_e= -10$ to 10 °C with $T_c=40$ °C) respectively, on the total exergy destruction of the investigated cycle using the examined refrigerants R131I and R134a as working fluids.

It can be seen from those results that as the (T_c) increases or the (T_e) decreases, the total exergy destruction of the investigated system increases. This can be interpreted by the fact that when the compressor pressure ratio becomes

superior, the compressor will need more input specific work (w_{comp}), and the heat rejection in the condenser will be higher for the same specific cooling (q_{evap}), resulting in superior exergy destruction for the refrigeration system.

Compared to the traditional R134a fluid, which has high GWP, the proposed candidate R131I has lesser total exergy destruction and offers lower exergy destruction decrement over corresponding basic cycle.

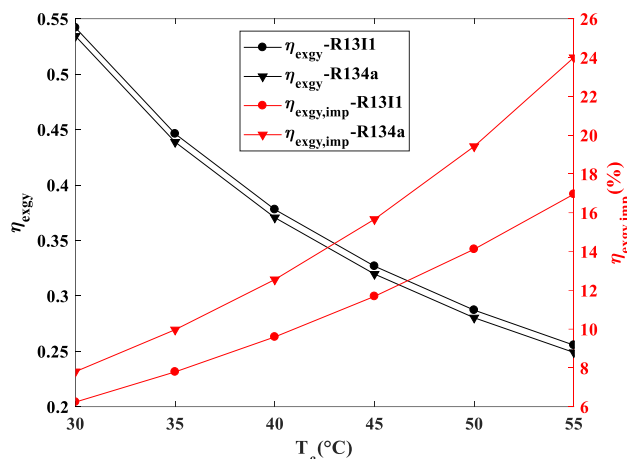


Figure 11. Influence of condensing temperature on η_{exgy} and $\eta_{exgy,imp}$.

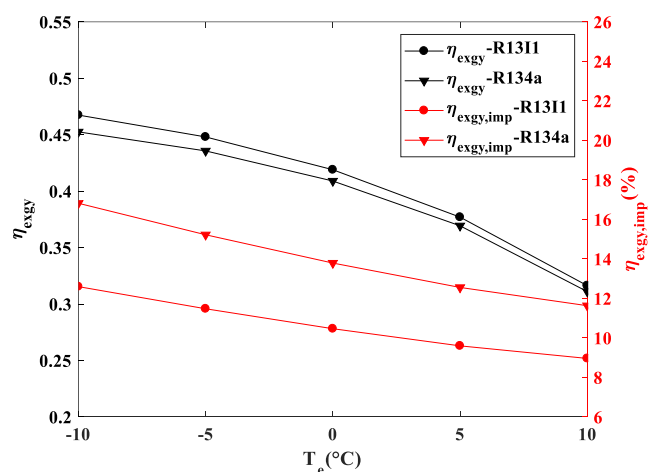


Figure 12. Influence of evaporating temperature on η_{exgy} and $\eta_{exgy,imp}$.

Using the investigated fluids R131I and R134a, the simulation results of the evolution of the exergy efficiency at $T_c=5^\circ\text{C}$ and for condensing temperatures ranging from (30 to 55°C), and at $T_c=40^\circ\text{C}$, and for the evaporating temperatures ranging from (-10 to 10°C) were presented respectively on Figures 11 and 12.

As shown in the figures, it is clear as the (T_c) or the (T_e) increases, the exergy efficiency of the studied cycle decreases. The exergy efficiency is based on the total exergy destruction and the input work of the compressor as mentioned in the equation (32), so when these two parameters increase with the increase of the condensing temperature (T_c), the total exergy destruction increases faster than that of the compressor work, which results in the decrease of exergy efficiency with the condensing temperature (T_c). On other hand, when the evaporator temperature (T_e) increases, the total exergy destruction, and the compressor work decrease and hence, the total exergy destruction decreases slower than that of the compressor

work, which results in the decrease of exergy efficiency with the evaporating temperature (T_e). It can also be seen that the eco-friendly R131I refrigerant has outperformed exergy efficiency compared with R134a refrigerant and exhibited lower exergy efficiency improvement over the corresponding conventional mechanical cycle.

The exergy efficiency of the studied refrigerants (R131I and R134a) varies from (0.2556 to 0.5419) and from (0.2490 to 0.5343), respectively, as the (T_c) increases from (30 to 55°C) as it can be observed from Figure 11, and from Figure 12 it can be seen that the exergy efficiency of the R131I and R134a varies from (0.3163 to 0.4674) and from (0.3110 to 0.4525), respectively, as the (T_e) increases from (-10 to 10°C).

On other hand, we can find that the exergy efficiency improvement is increased (higher $\eta_{ex,imp}$) at higher condensing temperatures or lower evaporating temperatures owing to the greater potential for expansion work recovery for both working fluids.

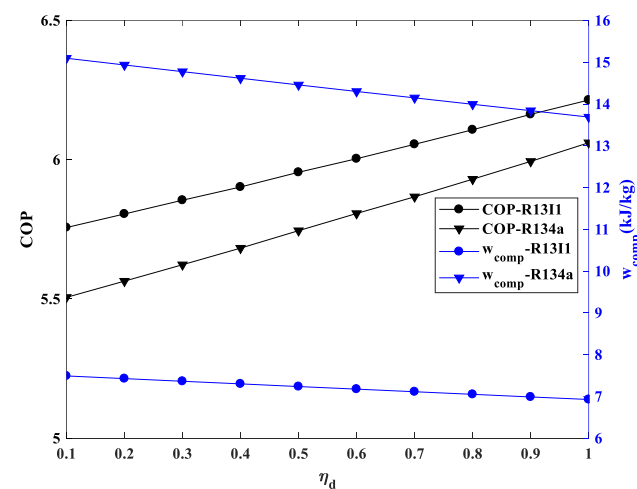


Figure 13. Variation of COP and compressor work with respect to diffuser efficiency of the ejector expansion device.

Figure 13 has been plotted to show the effect of diffuser efficiency of the ejector expansion device on the COP of the system and the specific work (w_{comp}) of the compressor working with the investigated refrigerants (R131I and R134a) with the same condensing temperature $T_c=40^\circ\text{C}$ and the evaporating temperature $T_e=5^\circ\text{C}$.

As shown in this figure, the result indicates that when the diffuser efficiency (η_d) of the ejector expansion device increase, the specific work of compression is lower. Since better efficiency has boosted the compressor inlet pressure, less compression work is needed by the compressor for a given compression ratio (π). As a result, the coefficient of performance (COP) increases as the diffuser efficiency (η_d) of the ejector expansion device increases as exposed in Figure 13.

Compared with the traditional R134a refrigerant, the eco-friendly R131I offers a lower specific work under the same operating temperatures ($T_c=40^\circ\text{C}$ and $T_e=-5^\circ\text{C}$), which confirms that it could be a good suitable substitute for the conventional working fluid R134a.

5. Conclusion

In this paper, a numerical model based on the energetic and exergetic methods of the EERC system is developed and validated to compare the performances of the eco-friendly

refrigerant R131I with the usually used fluid R134a in the EERC system under the same operating parameters.

The thermodynamic performances studied include the coefficient of performance (COP), the entrainment ratio (μ), the exergy destruction, and the exergy efficiency. Furthermore, the influences of evaporator and condenser temperatures on the EERC system performances and the influence of the isentropic efficiency of the diffuser section on the COP and on the compressor work are also examined and discussed.

The numerical results indicate that the R131I has a better performance, as well as lower exergy destruction compared to R134a.

Based on the results obtained from the present study, the main conclusions are listed as follows:

- The COP and μ for both working fluids R131I and R134a decrease with increasing the condenser temperature (T_c) and increase with the increasing evaporation temperature (T_e);
- The refrigerant R131I offers high better performances than R134a in terms of the entrainment ratio and the coefficient of performance under the same operating conditions;
- R131I refrigerant offers a lower exergy destruction compared to R134a for the same ranges of (T_c) and (T_e);
- The COP and the specific work are influenced by the diffuser efficiency (η_d) of the ejector expansion device;
- The COP increases and the compressor work decreases with the increase of the (η_d).

By analyzing the energetic performance of both studied working fluids, the investigated refrigerant R131I yields better performances in most of the cases, furthermore has excellent environmental properties, which confirms that it could be a suitable substitute for conventional working fluid R134a in the studied refrigeration system. From the results obtained, it would be very interesting to make a thermo-economic analysis in future works as well as research for new alternative azeotropic refrigerant blends.

Nomenclature

Symbols

COP	Coefficient of performance
h	Specific enthalpy [kJ kg^{-1}]
m	Mass flow rate [kg s^{-1}]
s	Specific entropy [$\text{kJ kg}^{-1} \text{K}^{-1}$]
u	Velocity [m s^{-1}]
q	Specific cooling [kJ kg^{-1}]
w	Specific work [kJ kg^{-1}]
p	Pressure [kPa]
T	Temperature [$^{\circ}\text{C}$ or K]
x	Vaporquality
δp	Pressure drop [kPa]
Ex	Exergy [kJ kg^{-1}]

Greek letters

μ	Entrainment ratio of ejector
η	Efficiency
ρ	Density [kg m^{-3}]
π	Compression ratio (P_2/P_1)

Subscripts

0	Reference environment
BC	Basic refrigeration cycle

c	Condensing process
$comp$	Compressor
$cond$	Condenser
d	Diffuser
e	Evaporation process
$evap$	Evaporator
ej	Ejector
tv	Throttle valve
is	Isentropic process
imp	Improvement
ms	Mixing chamber
mn	Motive nozzle
sn	Suction nozzle
Tot	Total
r	Refrigerated object
1-10	State point
Refrigerants name	
R134a	1,1,1,2-Tetrafluoroethane
R131I	Trifluoriodomethane

References:

- [1] W.T.Tsai, "Environmental risks of new-generation fluorocarbons in replacement of potent greenhouse gases," *Int. J. Glob. Warm.*, 5,84–95, 2013, doi:10.1504/IJGW.2013.051484.
- [2] A. Mota-Babiloni, J. Navarro-Esbrí, Á. Barragán-Cervera, F. Molés, and B. Peris, "Analysis based on EU Regulation No 517/2014 of new HFC/HFO mixtures as alternatives of high GWP refrigerants in refrigeration and HVAC systems," *Int. J. Refrig.*, 52,21–31, 2015, doi:10.1016/j.ijrefrig.2014.12.021.
- [3] J. Zhang, B. Elmegaard, and F. Haglind, "Condensation heat transfer and pressure drop characteristics of zeotropic mixtures of R134a/R245fa in plate heat exchangers," *Int. J. Heat. Mass. Transf.*, 164,120577, 2021, doi:10.1016/j.ijheatmasstransfer.2020.120577.
- [4] AA. Kornhauser, "The Use Of An Ejector as Refrigerant Expander," *Int. J. Refrig. Air. Cond.*, 1990, doi:10.1109/IECEC.1990.747930.
- [5] J. Sarkar, "Ejector enhanced vapor compression refrigeration and heat pump systems - A review," *Renew Sustain Energy Rev.*, 16, 6647–6659 2012, doi:10.1016/j.rser.2012.08.007.
- [6] M. Yari, "Exergetic analysis of the vapour compression refrigeration cycle using ejector as an expander," *Int. J. Exergy*, 5,326–340, 2008, doi:10.1504/IJEX.2008.018114.
- [7] E. Nehdi, L. Kairouani, and M. Bouzaina, "Performance analysis of the vapour compression cycle using ejector as an expander," *Int. J. Energy. Res.*, 31,364–375, 2007, doi:10.1002/er.1260.
- [8] Bilir HKE. Nagihan, "Performance improvement of the vapour compression refrigeration cycle by a two-phase constant area ejector," , 33,23–40, 2012, doi:10.1002/er.
- [9] P. Chaiwongsa, and S. Wongwiset, "Experimental study on R-134a refrigeration system using a two-phase ejector as an expansion device," *Appl Therm Eng.*, 28,467–477, 2008, doi:10.1016/j.applthermaleng.2007.05.005.

- [10] J. Sarkar, "Optimization of ejector-expansion transcritical CO₂ heat pump cycle," *Energy*, 33,1399–1406, 2008, doi:10.1016/j.energy.2008.04.007.
- [11] S. Elbel, and P. Hrnjak, "Experimental validation of a prototype ejector designed to reduce throttling losses encountered in transcritical R744 system operation," *Int. J. Refrig.*, 31, 411–422,2008, doi:10.1016/j.ijrefrig.2007.07.013.
- [12] HK. Ersoy, and N. Bilir, "Performance characteristics of ejector expander transcritical CO₂ refrigeration cycle," *Proc Inst Mech Eng Part A J Power Energy*, 226,623–635, 2012, doi:10.1177/0957650912446547.
- [13] Y. Gao, G. He, D. Cai, and M. Fan, "Performance evaluation of a modified R290 dual-evaporator refrigeration cycle using two-phase ejector as expansion device," *Energy*, 212,118614, 2020, doi:10.1016/j.energy.2020.118614.
- [14] Z. Ma, X. Liu, H. Wang, H. Li, and X. Wang, "Off-Design Analysis of Hydrocarbon-based Ejector-Expansion Refrigeration Cycle," *Energy Procedia*, 105, 4685–4690, 2017, doi:10.1016/j.egypro.2017.03.1015.
- [15] A. Shen, K. Guan, X. Yang, S. Jin, and L. Yang, "Theoretical analysis of a novel liquid-vapor separation condensation ejector refrigeration cycle with zeotropic mixtures," *Energy Convers Manag.*, 223,113322, 2020, doi:10.1016/j.enconman.2020.113322.
- [16] Y. Liu, and J. Yu, "Performance evaluation of an ejector subcooling refrigeration cycle with zeotropic mixture R290/R170 for low-temperature freezer applications," *Appl Therm Eng.*, 161, 114128, 2019, doi:10.1016/j.applthermaleng.2019.114128.
- [17] KKI. Al-Chlaihawi, and K. Al-Farhany, "A Comprehensive Energetic and Exergetic Analysis of an Ejector Expansion Refrigeration Cycle Using R22 and R410A," *Int J Air-Conditioning Refrig.*, 29, 2150013, 2021, doi:10.1142/S2010132521500139.
- [18] L. Zhao, X. Yang, S. Deng, H. Li, and Z. Yu, "Performance analysis of the ejector-expansion refrigeration cycle using zeotropic mixtures," *Int. J. Refrig.*, 57, 197-207, 2015, doi:10.1016/j.ijrefrig.2015.05.006.
- [19] G. Yan, T. Bai, and J. Yu, "Thermodynamic analysis on a modified ejector expansion refrigeration cycle with zeotropic mixture (R290/R600a) for freezers," *Energy*, 95, 144-154, 2016, doi:10.1016/j.energy.2015.11.067.
- [20] P. Jakończuk, K. Śmierciew, H. Zou, D. Butrymowicz, and A. Dudar, "Temperature drop of heating fluid as a primary condition for effective utilization of low-grade heat using flash cycles and zeotropic mixtures in refrigeration ejector systems," *Energy Sources, Part A Recover Util Environ Eff*, 1–19, 2021, doi:10.1080/15567036.2021.1876185.
- [21] TA. Jacob, and BM. Fronk, "In-Tube condensation of zeotropic refrigerant R454C from superheated vapor to subcooled liquid," *Sci Technol Built Environ.*, 26,1177–1190, 2020, doi:10.1080/23744731.2020.1804281.
- [22] SC. Yelishala, K. Kannaiyan, Z. Wang, H. Metghalchi, YA. Levendis, and R. Sadr, "Thermodynamic Study on Blends of Hydrocarbons and Carbon Dioxide as Zeotropic Refrigerants," *J Energy Resour Technol.*, 142,19-1855, 2020, doi:10.1115/1.4045930.
- [23] JM. Calm, "The next generation of refrigerants – Historical review, considerations, and outlook," *Int. J. Refrig.*, 31,1123–1133, 2008, doi:10.1016/J.IJREFRIG.2008.01.013.
- [24] H. Chen, DY. Goswami, and EK. Stefanakos, "A review of thermodynamic cycles and working fluids for the conversion of low-grade heat," *Renew Sustain Energy Rev.*, 4,3059–3067, 2010, doi:10.1016/j.rser.2010.07.006.
- [25] YY. Duan, L. Shi, LQ. Sun, MS. Zhu, and LZ. Han, "Thermodynamic Properties of Trifluoroiodomethane (CF₃I)," *Int. J. Thermophys.*, 21,393–404, 2000, doi:10.1023/A:1006683529436.
- [26] L. Benussi, S. Bianco, D. Piccolo, S. Colafranceschi, J. Kjølbro, A. Sharma, D. Yang, G. Chen, Y. Ban, and Q. Li "Properties of potential eco-friendly gas replacements for particle detectors in high-energy physics," *J. Instrum.*, 13, P03012–P03012, 2018, doi:10.1088/1748-0221/13/03/P03012.
- [27] H. Guo, M. Gong, X. Dong, and J. Wu, "Measurements of (vapour+liquid) equilibrium data for {trifluoroiodomethane (R131I) + isobutane (R600a)} at temperatures between (263.150 and 293.150) K," *J. Chem. Thermodyn.*, 58,428–431, 2013, doi:10.1016/j.jct.2012.10.003.
- [28] X. Dong, M. Gong, J. Liu, and J. Wu, "Experimental measurement of vapor pressures and (vapor + liquid) equilibrium for {1,1,1,2-tetrafluoroethane (R134a) + propane (R290)} by a recirculation apparatus with view windows," *J. Chem. Thermodyn.*, 43,505–510, 2011, doi:10.1016/J.JCT.2010.11.001.
- [29] Y. Maalem, S. Fedali, H. Madani, and Y. Tamene, "Performance analysis of ternary azeotropic mixtures in different vapor compression refrigeration cycles," *Int. J. Refrig.*, 119,139–151, 2020, doi:10.1016/j.ijrefrig.2020.07.021.
- [30] H. Li, F. Cao, X. Bu, L. Wang, and X. Wang, "Performance characteristics of R1234yf ejector-expansion refrigeration cycle," *Appl Energy*, 121, 96-103,2014, doi:10.1016/j.apenergy.2014.01.079.
- [31] J. Sarkar, "Performance characteristics of natural-refrigerants- based ejector expansion refrigeration cycles," *Proc Inst Mech Eng Part A J Power Energy*, 223, 543-550, 2009, doi.org/10.1243/09576509JPE753.
- [32] K. Sumeru, H. Nasution, and FN. Ani, "A review on two-phase ejector as an expansion device in vapor compression refrigeration cycle," *Renew Sustain Energy Rev.*, 16,4927–4937, 2012, doi:10.1016/j.rser.2012.04.058.
- [33] S. He, Y. Li, and RZ. Wang, "Progress of mathematical modeling on ejectors," *Renew Sustain Energy Rev.*, 13,1760–1780, 2009, doi:10.1016/j.rser.2008.09.032.
- [34] A. Khalil, M. Fatouh, and E. Elgendy, "Ejector design and theoretical study of R134a ejector refrigeration cycle," *Int. J. Refrig.*, 34,1684–1698, 2011, doi:10.1016/j.ijrefrig.2011.01.005.

- [35] O. Brunin, M. Feidt, and B. Hivet, "Comparison of the working domains of some compression heat pumps and a compression-absorption heat pump," *Int. J. Refrig.*, 20, 308-318, 1997, doi:10.1016/S0140-7007(97)00025-X.
- [36] Z. Zhang, L. Tong, L. Chang, Y. Chen, and X. Wang, "Energetic and Exergetic Analysis of an Ejector-Expansion Refrigeration Cycle Using the Working Fluid R32," *Entropy.*, 17, 4744-4761, 2015, doi:10.3390/e17074744.
- [37] J. Yu, H. Chen, Y. Ren, and Y. Li, "A new ejector refrigeration system with an additional jet pump," *Appl Therm Eng.*, 26, 312-9, 2006, doi:10.1016/j.applthermaleng.2005.04.018.

Research Article

Calculation of the Phase Diagrams (T – X and T – P) and the Thermodynamic Quantities for the Solid – Liquid Equilibria in n-tridecane

¹O. Tari^{ORCID}, ^{2*}H. Yurtseven^{ORCID}

¹ Department of Electrical and Electronics Engineering, Istanbul Arel University, 34537 Büyükçekmece, Istanbul - TURKEY

² Department of Computer Engineering, Baskent University, 06790 Ankara – TURKEY
E-mail: ^{2*}hamit@metu.edu.tr

Received 20 March 2023, Revised 26 May 2023, Accepted 28 July 2023

Abstract

The solid – liquid equilibria in n-tridecane is investigated by calculating phase diagrams and the thermodynamic quantities using the Landau phenomenological model. By expanding the free energy in terms of the order parameter of the solid phase, the phase line equations are fitted to the experimental data for the T – X and T – P phase diagrams from the literature. The temperature dependences of the thermodynamic quantities (order parameter ψ , susceptibility χ_ψ , free energy F , the heat capacity C , entropy S and the enthalpy H) are predicted for the n-tridecane from this model. Our results give that the slope $dT/dP \cong 2$ K/MPa for n-C₁₃ to n-C₁₇. ψ varies with T as $\psi \sim (T - T_m)^{1/2}$ above T_m . It is linear for the χ_ψ^{-1} , $S(T)$ and $C(T)$, and quadratic for the $F(T)$ and $H(T)$ in n-tridecane. This indicates that the Landau model, describes the observed behaviour of the phase diagrams satisfactorily for the solid – liquid equilibria in n-tridecane. Predictions of the thermodynamic quantities can also be compared with the measurements and predictions of some other theoretical models. The pressure effect, in particular, on the solid – liquid equilibria in n-tridecane can also be investigated under the model studied here.

Keywords: Solid – liquid equilibria; T – X and T – P phase diagrams; thermodynamic quantities; n-tridecane.

1. Introduction

The phase behavior of pure n-alkanes has been the subject of various experimental and theoretical studies. Experimental determination of thermodynamic and structural properties of pure long-chain n-alkanes, and phase diagrams of their molecular alloys have been reported in the literature as also indicated previously [1, 2]. Solid-liquid equilibria (SLE) of the n-alkanes [3] with the effect of pressure have been studied experimentally [4] and, the phase equilibria for the binary systems have been determined using a cryometric dynamic method at atmospheric pressure, additionally, the influence of pressure on liquidus curve up to 800 MPa was determined for systems [5]. A liquid to solid transition has been predicted by the high pressure molecular dynamics (MD) simulations [6], as also reported previously [7]. Various experimental studies [8-13] have been reported in the literature to explain the structure and the phase transitions of the rotator phases in n-alkanes. As stated some years ago, binary mixtures of normal alkanes exhibit a first order character of the liquid – solid transition [8 - 13], which has been studied by the Landau phenomenological theory [14]. It has also been indicated that binary normal alkane (n-alkane) shows the isotropic liquid state and the low temperature ordered crystal phase [15]. Experimentally, systematic hysteresis has been observed by photopyroelectric calorimetry confirming the first order behavior of n-alkanes [16]. The crystallization and phase transition behaviours of normal alkane (n-docosane) were

studied by the DSC, XRD and variable – temperature solid state NMR [17]. Also, pressure – induced phase changes of n-heptane have been studied experimentally [7]. Recently, theoretically by means of the molecular dynamic simulations, thermodynamic properties of small linear alkanes have been studied [18]. Experimentally, for the tetradecane + hexadecane system the T – X phase diagram was obtained at various pressures [1, 19]. Also, the experimental measurements were conducted for the phase diagrams of the n-tridecane + n-hexane (n-cyclohexane) systems [20]. The equilibrium phase diagram of n-octadecane + n-nonadecane has been studied [21].

Regarding the phase diagrams for the binary systems, the alkane system of dodecane-tridecane has been obtained to find phase change materials (PCMs) for freezing applications [22]. Also, the phase diagram for the binary systems of $n - C_{11} \dots$ was experimentally investigated to employ potential PCMs for cryogenic materials [23]. The equilibrium phase behaviours and thermal characteristics (phase diagrams, enthalpies, melting / freezing temperatures) of the binary systems were experimentally investigated [24]. Very recently, we have also studied the liquid – solid phase diagram of n-alkanes (C_nH_{2n+2}) [25] and the thermodynamic properties of the binary system of tetradecane and hexadecane [26, 27] by using Landau mean field theory which has also been used to describe the liquid – solid transitions in n-alkanes in some previous studies [14, 28]. Since adequate thermodynamic models can describe the

phase behavior of the very complex systems such as pure n-alkanes and synthetic mixtures by knowing their structural properties [1], the Landau model can be an appropriate one to describe the observed behavior of those mixtures. As indicated previously, the main aim is to further understand the complexity of the phase stability and the phase transition of n-alkanes [17]. In order to describe the thermal characteristics of the solid-liquid transition in n-alkanes generally their common physical properties can be investigated by modelling them theoretically. This can provide an universal curve for their phase diagrams ($T - T_m$ vs. $x_m - x$ or $T - T_m$ vs. $P - P_m$) and also for their thermodynamic quantities close to the liquid-solid transitions in n-alkanes. This has motivated us to investigate the liquid – solid transition on the phase boundary between the liquid phase and the two-phase liquid – solid phase domain, particularly, in n-tridecane within the Landau phenomenological model. $T - X$ and $T - P$ phase diagrams of n-tridecane are calculated by means of the phase line equation which is fitted to the experimental data [4]. Based on the phase diagrams calculated, the temperature dependences of the thermodynamic quantities such as the order parameter, susceptibility, free energy, entropy, heat capacity and enthalpy are predicted for n-tridecane.

2. Theory

The solid – liquid phase equilibria in synthetic waxes can be studied by the Landau mean field theory. By expanding the free energy of the solid phase in terms of the order parameter, the phase line equation and the order parameter can be obtained by means of the coefficients in the expansion. From the free energy expansion, thermodynamic functions of interest can be obtained for the solid – liquid equilibria in those mixtures.

2.1 Phase Line Equation and the Order Parameter

We can express the free energy of the solid – liquid phase equilibria in synthetic waxes which exhibit first order transition, in terms of the order parameter on the basis of the Landau phenomenological model as

$$F = a_2\psi^2 + a_3\psi^3 + a_4\psi^4 \quad (1)$$

where the coefficients a_2 , a_3 and a_4 can depend on the temperature, concentration (mole fraction) and pressure in general. Note that there is no ordering in the liquid phase so that the free energy of this phase is zero ($F_L = 0$). Various forms of the free energy expanded in terms of the order parameters including the coupled terms for the rotator phases in n-alkanes, have been given in some previous studies [14, 28]. We have also given the functional form of the free energy in terms of the order parameters for n-alkanes in our recent studies [25-27].

The free energy can be minimized with respect to the order parameter ψ of the solid phase ($\partial F/\partial\psi = 0$), which gives

$$4a_2\psi^2 + 3a_3\psi + 2a_4 = 0 \quad (2)$$

By solving Eq. (2.2) for ψ , we get

$$\psi = (-3a_3 \pm \sqrt{9a_3^2 - 32a_2a_4})/8a_4 \quad (3)$$

In the root square, by assuming that

$$(32a_2a_4/9a_3^2) \ll 1 \quad (4)$$

using the Taylor's expansion

$$(1 - x)^n = 1 - nx + \frac{n(n-1)}{2!}x^2 + \dots \quad (5)$$

the order parameter ψ becomes

$$\psi = -\frac{3a_3}{8a_4} \pm \frac{3a_3}{8a_4} \left(1 - \frac{16a_2a_4}{9a_3^2}\right) \quad (6)$$

where only the first two terms in Eq. (5) are taken into account (higher order terms are ignored). By also taking the positive root solution (Eq. (6)), the order parameter can be written simply as

$$\psi = -\frac{2a_2}{3a_3} \quad (7)$$

This can express the temperature and pressure dependence of the order parameter in the solid phase for the solid – liquid equilibria in synthetic waxes. In order to get the phase line equation for the solid – liquid transition, the order parameter ψ (Eq. (7)) can be substituted into the free energy (Eq. (1)) which gives

$$a_2a_4 = -3a_3^2/4 \quad (8)$$

This is the phase line equation for the solid – liquid equilibria in synthetic waxes. By considering temperature, concentration or pressure dependence of the coefficients a_2 , a_3 and a_4 , $T - X$, $T - P$ or $P - X$ phase diagrams of those compounds can be predicted by the Landau mean field theory using the experimental data. In this study, we calculated $T - T_m$ versus $x_m - x$ (T_m and x_m are the melting temperature and composition, respectively) and $T - T_m$ versus $P - P_m$ (P_m denotes the melting pressure) for the liquid-solid transition in n-tridecane by using the experimental data [4].

2.2 Thermodynamic Quantities

For the solid – liquid equilibrium in synthetic waxes, the temperature dependence of the thermodynamic quantities such as the order parameter susceptibility, entropy, enthalpy, heat capacity and the free energy can be predicted from the Landau phenomenological model.

The order parameter susceptibility (χ_ψ) can be obtained from the free energy (Eq. (1)) in terms of the order parameter ψ for the solid – liquid equilibria in synthetic waxes. By using the definition of the susceptibility, $\chi_\psi^{-1} = \partial^2 F/\partial\psi^2$, we find that

$$\chi_\psi^{-1} = 2(a_2 + 3a_3\psi + 6a_4\psi^2) \quad (9)$$

or by using ψ (Eq. (7)) in this equation, the inverse susceptibility becomes

$$\chi_\psi^{-1} = -2a_2 + \frac{16a_2^2a_4}{3a_3^2} \quad (10)$$

As in the order parameter ψ , by means of the dependences of the coefficients a_2 , a_3 and a_4 , the order parameter susceptibility χ_ψ can be obtained as functions of temperature, pressure and concentration for the solid – liquid

Table 1. Values of the coefficients (Eq. (15)) at the melting pressure ($P = P_m = 0.1 \text{ MPa}$) with the melting temperatures (T_m) and composition (x_m) of M_1 to M_9 [4] of the various mixtures ($n\text{-C}_{13}$ to $n\text{-C}_{17}$) for the liquid – solid transition in n -tridecane. Uncertainties of the coefficients and the R^2 values are also given.

Mixtures	Melting Temperature T_m (K)	Melting composition x_m (mass %)	$-a_0'$ (K)	$-a_1'$ K/(mass %)	$-a_2' \times 10^{-1}$ K/(mass %) ²	$-a_3' \times 10^{-3}$ K/(mass %) ³	R^2
n-C₁₃	270.6	50.02	41.3±8.4	5.43±0.94	2.18±0.33	3.10±0.38	0.9991
n-C₁₄	270.6	49.98	39.1±7.9	5.21±0.90	2.11±0.32	3.02±0.36	0.9991
n-C₁₅	273.7	33.33	7.5±3.3	2.24±0.69	-1.55±0.43	4.88±0.86	0.9996
n-C₁₆	277.0	25.4	10.4±3.3	4.17±1.07	4.03±1.05	16.83±3.19	0.9996
n-C₁₇	279.9	20.13	-3.5±0.5	-0.75±0.22	-2.21±0.30	2.22±1.32	1

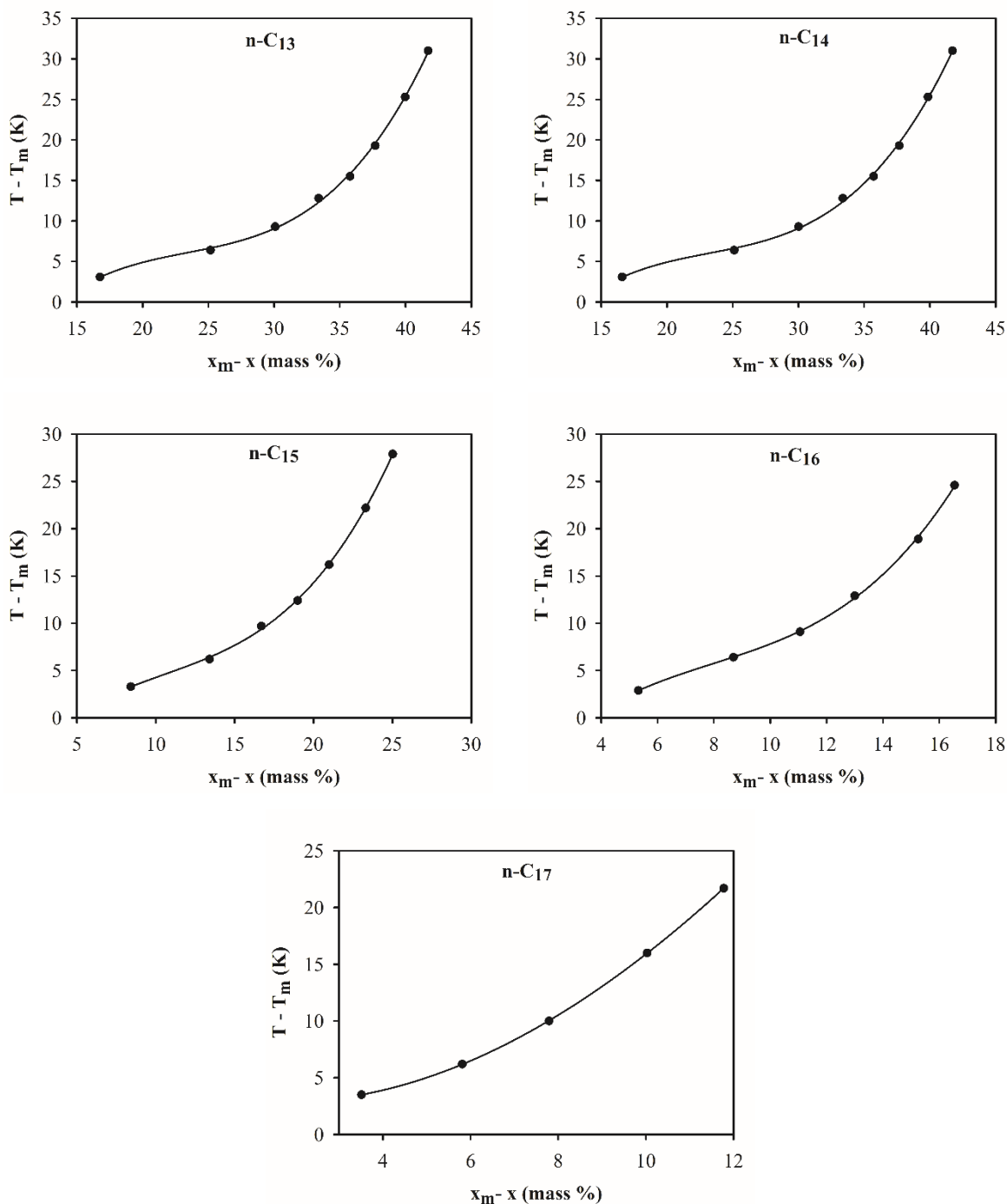


Figure 1. $T - X$ phase diagram of liquid – solid phase transition in n -tridecane of various mixtures according to Eq. (15). T_m and x_m indicate the melting temperature and composition (mass %), respectively, ($P = P_m$) with the experimental data [4] as shown.

equilibria in synthetic waxes. The temperature dependence of the other thermodynamic quantities can also be predicted which is given below. As we have calculated the thermodynamic quantities of the binary system of tetradecane and hexadecane for its liquid-solid phase transition previously [26], we also calculated in this study the order parameter, inverse susceptibility, free energy, entropy, heat capacity and the enthalpy as a function of $T - T_m$ for n-tridecane.

Table 2. Values of the coefficients (Eq. (15)) at the melting composition ($x = x_m$) with the melting temperatures (T_m at $P = 0.1$ MPa) of various components M_1 to M_9 [4] for the liquid – solid transition in n-tridecane. Uncertainties of the coefficients and the R^2 values are also given.

Mixtures	T_m (K)	$a_0' \times 10^{-1}$ (K)	$a_4' \times 10^{-1}$ (K/MPa)	R^2
M_1	270.6	3.21 ± 2.12	1.99 ± 0.03	0.9987
M_2	273.7	3.67 ± 2.22	1.95 ± 0.04	0.9986
M_3	277.0	4.13 ± 2.90	1.91 ± 0.05	0.9975
M_4	279.9	3.51 ± 2.75	1.90 ± 0.05	0.9977
M_5	283.4	2.96 ± 1.85	1.88 ± 0.03	0.9989
M_6	286.1	3.41 ± 2.31	1.94 ± 0.04	0.9984
M_7	289.9	3.45 ± 2.68	1.92 ± 0.04	0.9979
M_8	295.9	2.48 ± 1.84	1.95 ± 0.03	0.9990
M_9	301.6	1.21 ± 1.14	1.97 ± 0.02	0.9996

3. Calculations and Results

3.1 Calculation of Phase Diagram

In this study, we first obtained the phase diagrams ($T - P$ or $T - X$) for the solid – liquid equilibria in synthetic waxes. This was done by assuming the temperature, pressure and concentration (mole fraction) of the coefficients a_2 , a_3 and a_4 as Eqs. (1) - (4).

$$a_2 = a_{20} + a_{21}(T - T_m) + a_{22}(P - P_m) \quad (11)$$

$$a_3 = a_{30}(T - T_m)^{1/2} \quad (12)$$

$$a_4 = a_{40} + a_{41}(x - x_m) + a_{42}(x - x_m)^2 + a_{43}(x - x_m)^3 \quad (13)$$

where T_m , P_m and x_m represent the melting (freezing) temperature, pressure and concentration, respectively. By substituting those dependences (Eqs. (11) - (13)) into the phase line equation (Eq. (8)), one gets

$$[a_{20} + a_{21}(T - T_m) + a_{22}(P - P_m)][a_{40} + a_{41}(x - x_m) + a_{42}(x - x_m)^2 + a_{43}(x - x_m)^3] = -\frac{3}{4}a_{30}^2(T - T_m) \quad (14)$$

By expanding the parenthesis and ignoring the cross terms such as $(T - T_m)(x - x_m)$ and $(P - P_m)(x - x_m)$ with the higher order terms in the expansion, we find that

$$T - T_m = a_0' + a_1'(x - x_m) + a_2'(x - x_m)^2 + a_3'(x - x_m)^3 + a_4'(P - P_m) \quad (15)$$

where

$$\begin{aligned} a_0' &= a_{20}a_{40}/a_0 \\ a_1' &= a_{20}a_{41}/a_0 \\ a_2' &= a_{20}a_{42}/a_0 \\ a_3' &= a_{20}a_{43}/a_0 \\ a_4' &= a_{22}a_{40}/a_0 \end{aligned} \quad (16)$$

with the definition of a_0 as

$$a_0 = -1/(a_{21}a_{40} + 3a_{30}^2/4) \quad (17)$$

We plot in Fig. 1 the $T - T_m$ versus $x_m - x$ (mass %) phase diagrams of n-paraffins ranging from n-C₁₃ to n-C₁₇ with various number of compounds at $P = P_m = 0.1$ MPa (atmospheric pressure) by using the experimental data [4] according to Eq. (15). From this fit, we obtained values of the coefficients a_0' , a_1' , a_2' and a_3' , which are given in Table 1. For the determination of the coefficients a_0' , a_1' , a_2' , a_3' and a_4' , our fitting procedure is the following: according to Eq. (15), by taking $P = P_m = 0.1$ MPa we obtained $T - T_m$ as a function of $x - x_m$ in the polynomial form, which was fitted to the experimental data [4] to determine the coefficients a_0' , a_1' , a_2' and a_3' . Similarly, by taking $x = x_m$ in Eq. (15) which was fitted to the experimental data [4] and the coefficients a_0' and a_4' were determined, as given in Table 1. Values of the uncertainties with the R^2 values are also indicated at Table 1. Melting temperatures were taken at $P = 0.1$ MPa by using the observed $P - T$ data [4]. The melting temperatures and compositions at $P = 0.1$ MPa are given at Table 1 for the mixtures (n-C₁₃ to n-C₁₇) from the observed data [4]. At the melting composition ($x = x_m$) from Eq. (15), variation of $T - T_m$ with the $P - P_m$ was obtained by using the observed data [4] for various mixtures (M_1 to M_9) for the liquid-solid phase transition in n-tridecane, as plotted in Fig. 2. Coefficients of a_0' and a_4' with the uncertainties and the R^2 values are given at Table 2.

3.2 Calculation of the Order Parameter and Susceptibility

Temperature dependence of the order parameter ψ for the solid – liquid equilibria in synthetic waxes can be obtained using Eq. (7) by means of Eqs. (11) and (12), as stated above. By substituting Eqs. (11) and (12) into Eq. (7) at the melting pressure ($P = P_m$), we get simply

$$\psi = \psi_0(T - T_m)^{1/2} \quad (18)$$

In our treatment, we ignored the $(T - T_m)^{-1/2}$ term in the expansion since the order parameter of the solid phase decreases and goes to zero as the melting temperature T_m is approached from the solid phase (ψ is zero in the liquid phase). We used the experimental data from the $P - T$ measurements of the mixtures M_1 to M_9 in n-tridecane at $P = 0.1$ MPa to calculate the order parameter ψ according to Eq. (18). We plot in Fig. 3 the order parameter ψ (normalized) as a function of the $T_m - T$ for the mixtures M_1 to M_9 in n-tridecane ($P = 0.1$ MPa).

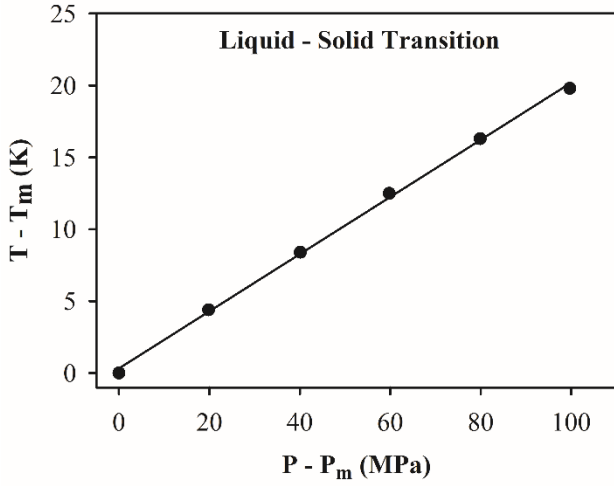


Figure 2. Liquid – solid phase transition temperatures of components (M_1 to M_9) in *n*-tridecane as a function of pressure according to Eq. (15) at $x = x_m$. T_m and P_m represent the melting temperature and pressure, respectively, with the experimental data [4] shown.

Similarly, temperature dependence of the order parameter susceptibility (χ_ψ) can be obtained as we obtained for ψ (Eq. (18)). By substituting Eqs. (11) – (13) into Eq. (10), we get the temperature and pressure dependence of χ_ψ^{-1} at $x = x_m$ as

$$\chi_\psi^{-1} = A + B(T - T_m) + C(P - P_m) + D(T - T_m)^{-1} \quad (19)$$

where

$$\begin{aligned} A &= \frac{2a_{20}}{a_{30}^2} (2a_{21}a_{40} - a_{30}^2) \\ B &= -\frac{2a_{21}}{a_{30}^2} (a_{30}^2 - a_{21}a_{40}) \\ C &= \frac{a_{22}}{a_{30}^2} (a_{30}^2 - a_{21}a_{40}) \\ D &= \frac{2a_{20}a_{40}}{a_{30}^2} [a_{20} + a_{22}(P - P_m)] \end{aligned} \quad (20)$$

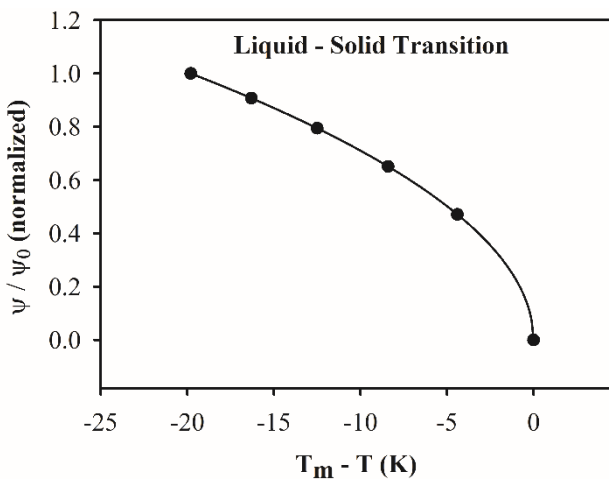


Figure 3. Temperature dependence of the order parameter ψ (normalized) for the solid phase, which was calculated according to Eq. (18) at the melting composition ($x = x_m$) using the temperatures, T_m , melting temperatures [4] for liquid – solid transition of various components (M_1 to M_9) of *n*-tridecane.

Note that the order parameter susceptibility (χ_ψ) can also be calculated directly from the temperature dependence of the order parameter ψ (Eq. (18)) according to Eq. (9) using Eqs. (11) – (13). By means of Eqs. (11) – (13) at $x = x_m$ ($P = P_m = 0.1$ MPa) we simply obtain

$$\chi_\psi^{-1} = \chi_0^{-1}(T - T_m) \quad (21)$$

when we take $a_{20} = 0$, where

$$\chi_0^{-1} = (16a_{21}^2 a_{40} / 3 a_{30}^2) - 2a_{21} \quad (22)$$

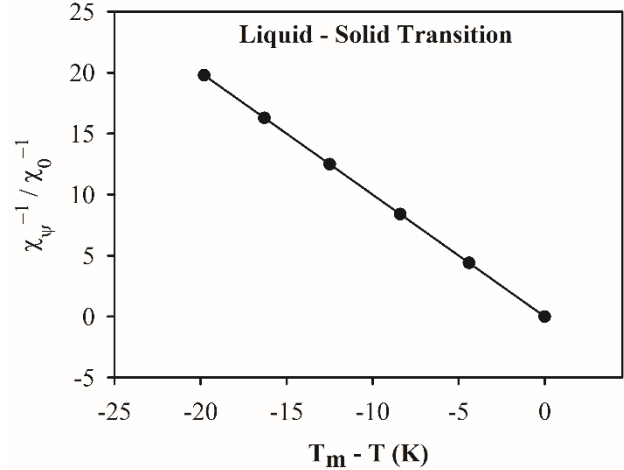


Figure 4. Temperature dependence of the inverse susceptibility χ_ψ^{-1} (normalized) for the order parameter ψ , which was calculated according to Eq. (21) at the melting composition ($x = x_m$) using the temperatures, T_m , melting temperatures [4] for liquid – solid transition of various components (M_1 to M_9) of *n*-tridecane.

In this study, the temperature dependence of χ_ψ^{-1} was calculated at $P = P_m = 0.1$ MPa according to Eq. (19) by ignoring the $(T - T_m)^{-1}$ term since the inverse susceptibility decreases as the melting temperature T_m is approached from the solid phase for the liquid – solid transitions, in particular, *n*-tridecane studied here. We plot in Fig. 4 the inverse susceptibility (χ_ψ^{-1}) normalized as a function of the $T_m - T$ for the mixtures M_1 to M_9 in *n*-tridecane ($P = 0.1$ MPa). As seen from Fig. 4 it is a single curve at various $T_m - T$ for those mixtures (M_1 to M_9) in *n*-tridecane.

3.3 Calculation of the Free Energy, Entropy, Enthalpy and Heat Capacity

We assumed the temperature dependence of the free energy in the functional form.

$$F = F_0(T - T_m)^2 \quad (23)$$

for the solid – liquid transition for the mixtures M_1 to M_9 in the *n*-tridecane ($P = 0.1$ MPa). Fig. 5 gives F (normalized) at various $T - T_m$ as a single curve. This results in the entropy $S = (\partial F / \partial T)_V$, which varies linearly variation with the temperature as

$$S = S_0(T - T_m) \quad (24)$$

We plot the entropy (normalized) as a function of $T - T_m$ in Fig. 6.

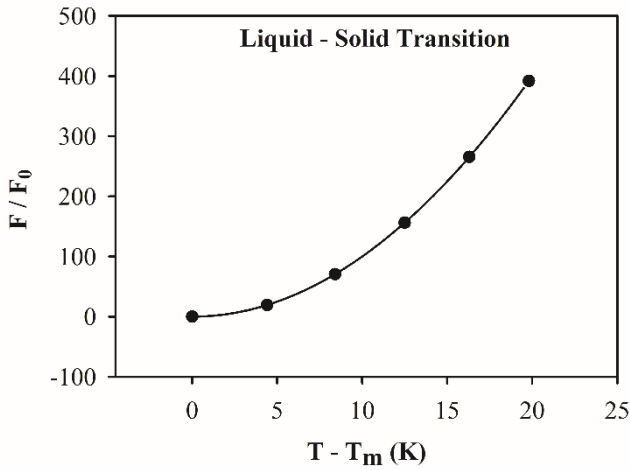


Figure 5. Temperature dependence of the free energy F (normalized) for the solid phase, which was calculated according to Eq. (23) at the melting composition ($x = x_m$) using the temperatures, T_m , melting temperatures [4] for liquid – solid transition of various components (M_1 to M_9) of *n*-tridecane.

Using the definition of the heat capacity $C_V = T(\partial S/\partial T)_V$, we obtain from Eq. (23),

$$C = C_0 T \quad (25)$$

where $C_0 = S_0$, as the linear variation of C with the temperature similar to the entropy S . We plot in Fig. 7 the heat capacity C (normalized) as a function of $T - T_m$ (above the melting temperature) for the various mixtures (M_1 to M_9) in the synthetic waxes. Finally, from the definition of $C_V = \partial H/\partial T$, we obtained the enthalpy function as

$$H(T) - H(T_m) = H_0(T^2 - T_m^2) \quad (26)$$

where $H_0 = S_0/2$. This is plotted in Fig. 8 for the solid – liquid transition in the mixtures studied.

4. Discussion

In this study, the $T - X$ and $T - P$ phase diagrams were calculated by means of the Landau phenomenological model using the experimental data [4] for composition (mass %) of the various mixtures (M_1 to M_9) for the solid – liquid equilibria of *n*-tridecane (*n*-C₁₃ to *n*-C₁₇). As given in the $T - T_m$ versus $x_m - x$ plots (Fig. 1), the composition (mass %) increases below the melting composition (x_m) for all the components of *n*-tridecane as we fitted Eq. (15) to the experimental data at $P = P_m$. The cubic polynomial fit (Eq. (15)) is reasonable to describe the experimental data for the variation of the liquid – solid transition temperatures with the composition below the melting point in various mixtures (M_1 to M_9) for *n*-tridecanes (*n*-C₁₃ to *n*-C₁₇) on the basis of the Landau mean field model. Since the experimental data were insufficient for the mixtures *n*-C₁₈ to *n*-C₂₄ [4], we were not able to perform the fitting procedure for the three mixtures. We also fitted Eq. (15) to the experimental $P - T$ data [4] at the melting composition ($x = x_m$) for mixtures (M_1 to M_9) to describe the liquid – solid phase transitions in complex waxy systems, as plotted in Fig. 2. As a single curve, variation of $T - T_m$ with the $P - P_m$ is linear (Eq. (15)) at $x = x_m$ for the pressure range (0.1 to 100 MPa) of those mixtures, which was also obtained experimentally [4] for the $T - P$ phase diagram.

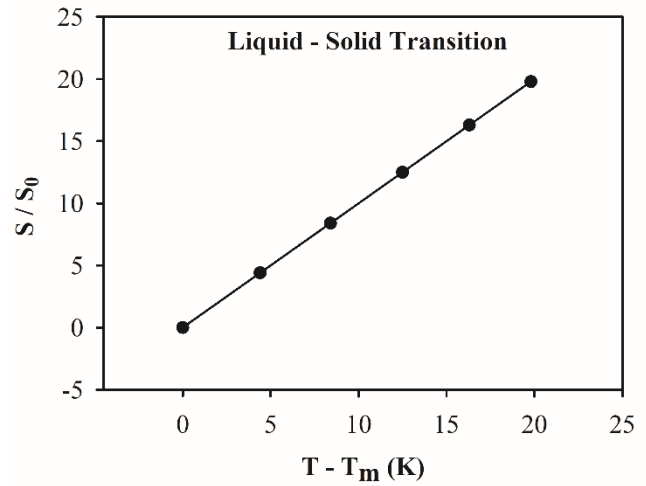


Figure 6. Temperature dependence of the entropy S (normalized) for the solid phase, which was calculated according to Eq. (24) at the melting composition ($x = x_m$) using the temperatures, T_m , melting temperatures [4] for liquid – solid transition of various components (M_1 to M_9) of *n*-tridecane.

Regarding the change in the temperature ($T - T_m$) per unit change in the composition ($x_m - x$), which gives rise to the slope, $d(T - T_m)/d(x_m - x)$ in the $T - T_m$ versus $x_m - x$ plot above the melting point, we find an almost linearity in the temperature range of $\sim 15 - 20$ K which corresponds to the composition range of 35 - 40 (mass %) for the mixtures of *n*-C₁₃, *n*-C₁₄ and *n*-C₁₅ (Fig. 1). This gives the slope value of ~ 2 K/mass (%) with the components of M_6 to M_9 (*n*-C₁₃ and *n*-C₁₄), M_7 to M_9 (*n*-C₁₅). For the components of M_8 and M_9 (*n*-C₁₆), and M_7 to M_9 (*n*-C₁₇), within the range of 15 – 25 K (13 – 16 mass %) and 10 – 22 K (8 – 12 mass %), respectively, the slope value is about 3 K/mass (%). Outside this range of the temperature and the composition (mass %) above the melting point, changes in the temperature ($T - T_m$) and in the composition ($x_m - x$) are nonlinear so that the slope change corresponds to the heavier components in the composition (mass %) of M_1 to M_5 in *n*-tridecane (*n*-C₁₃ to *n*-C₁₇), as shown in Fig. 1. We expect the same kind of behavior for the mixtures of *n*-C₁₈ and *n*-C₁₉ whose slope changes nonlinearly in the $T - T_m$ versus $x_m - x$ plot. For those two mixtures, we were not able to predict the variation of $T - T_m$ with the $x_m - x$ because of the lack of the experimental data [4], as stated previously.

Variation of the temperature change ($T - T_m$) with the pressure ($P - P_m$) can also be obtained by the slope value of nearly $\alpha_4' = 0.19 - 0.20$ K/MPa at $x = x_m$ from Eq. (15) for all the components of M_1 to M_9 (Table 2), which is a linear variation as plotted in Fig. 2. Thus the increase of pressure ($P - P_m$) by 1 MPa, changes the temperature ($T - T_m$) about 0.2 K within the pressure range of 0.1 MPa (atmospheric pressure) to 100 MPa at $x = x_m$ on the basis of the experimental measurements of all the components (M_1 to M_9) for the liquid – solid phase transition in tridecane. This change was nearly 2 K (*n*-C₁₃, *n*-C₁₄ and *n*-C₁₅) and 3 K (*n*-C₁₆ and *n*-C₁₇) per unit change in mass (%) for the linear variation in the temperature ($T - T_m$) and composition ($x_m - x$) intervals above the melting point in *n*-tridecane, as stated previously.

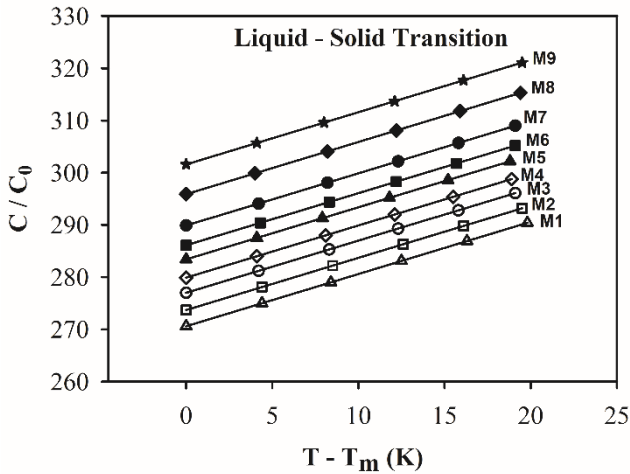


Figure 7. Temperature dependence of the heat capacity C (normalized) for the solid phase, which was calculated according to Eq. (25) at the melting composition ($x = x_m$) using the temperatures, T_m , melting temperatures [4] for liquid – solid transition of various components (M_1 to M_9) of n-tridecane.

Once we calculated the phase diagrams ($T - X$ and $T - P$) for the various mixtures (M_1 to M_9) of n-tridecane (n- C_{13} to n- C_{17}), we were then able to predict the temperature dependence of the order parameter ψ (Fig. 3), inverse susceptibility χ_ψ^{-1} (Fig. 4), free energy F (Fig. 5), entropy S (Fig. 6), the heat capacity C (Fig. 7) and enthalpy H (Fig. 8). Starting from the order parameter ψ , it decreases to zero as the melting temperature is approached from the solid phase (Fig. 3) for the n-tridecane system. The order parameter (normalized) values for all the mixtures (M_1 to M_9) fall onto a single curve as a function of $T_m - T$, as expected according to Eq. (18) with the critical exponent $1/2$. This is the critical exponent value expected from the mean field theory. Thus, at $P = P_m$ and $x = x_m$ for the components of the n-tridecane the order parameter ψ describes the liquid-solid transition (Eq. (18)) on the basis of the phase line equation (Eq. (15)). This can be tested experimentally by the measurements of ψ as a function of $T_m - T$ for various components of n-tridecane. On the other hand, variation of the inverse susceptibility χ_ψ^{-1} is linear with the $T_m - T$ (Fig. 4) according to Eq. (21) at $P = P_m$ for all the compositions (M_1 to M_9). In our calculation of the inverse susceptibility using Eq. (21), we considered the linear term in $T - T_m$ at $P = P_m$ (Eq. (19)) which dominates the behavior of the χ_ψ^{-1} for the liquid – solid phase transition in n- tridecane. This is also consistent with the behavior of the order parameter ψ (Fig. 3) for this mixture.

Regarding the quadratic temperature dependence of the free energy F (Eq. (23)), we obtained that F increases in the solid phase above the melting temperature T_m in the mixtures studied (Fig. 5). From the functional form of F (Eq. (23)), we arrived at a linear variation of the entropy S (Eq. (24)), as plotted in Fig. 6. As the F increases in the solid phase, S increases linearly with the temperature ($T - T_m$). The heat capacity C also varies linearly (Eq. (25)) above T_m for all the compositions (M_1 to M_9), as plotted separately for each component in Fig. 7. For the second order transitions (solid-solid transitions or transitions in liquid crystals), which is the concern of various theoretical models such as Ising model, Heisenberg model, Potts model, spherical model etc., the entropy S exhibits discontinuity at the critical temperature,

T_c . This gives rise to a continuous behaviour of the heat capacity C at the T_c . From the mean field theory, critical behaviour of the C is logarithmic. However, for the liquid-solid transition, which is of the first order, the entropy S and the heat capacity vary linearly with the $T - T_m$, as given in Figs. 6 and 7, respectively.

The heat capacity C (normalized) was plotted as a function of $T - T_m$ above the melting temperature T_m , as plots of the free energy F (Fig. 5), entropy S (Fig. 6) and enthalpy H (Fig. 8). Since the heat capacity was calculated above the T_m , a plot of C/C_0 versus $T - T_m$ provided us to compare all the components M_1 to M_9 with the same slope as a single (universal) curve (with the different C/C_0 values) for the liquid-solid transition in n-tridecane. Starting from the component M_1 up to M_9 , the heat capacity (C/C_0) increases linearly above the melting temperature with the same slope value as predicted from the Landau phenomenological model (Eq. (25)), as shown in Fig. 7. This also shows that the heavier component (M_1) in mass (%) has lower heat capacity in magnitude as compared to the lighter one (M_9) which has larger heat capacity for the liquid – solid phase transition in n-tridecane.

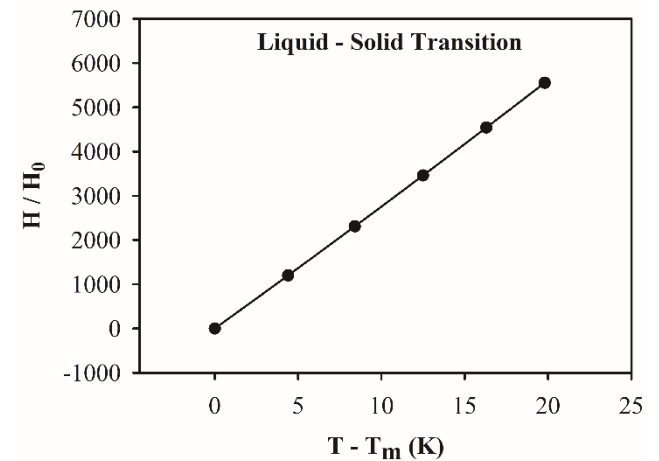


Figure 8. Temperature dependence of the enthalpy H (normalized) for the solid phase, which was calculated according to Eq. (26) at the melting composition ($x = x_m$) using the temperatures, T_m , melting temperatures [4] for liquid – solid transition of various components (M_1 to M_9) of n-tridecane.

As in the case of the free energy F which was described using a quadratic function (Eq. (23)), the enthalpy function was also described quadratically (Eq. (26)) for the liquid – solid transition in the n-tridecane (n- C_{13} to n- C_{17}) with various compositions (M_1 to M_9). It increases as the free energy F (Fig. 5), entropy S (Fig. 6) and the heat capacity C (Fig. 7) above the melting temperature T_m in the solid phase for the liquid – solid transition in tridecane, as expected from the mean field theory. Variation of the enthalpy $H(T)$ with the $T - T_m$ above the melting temperature (T_m), is quadratic according to Eq. (26) for the liquid-solid transition in n-tridecane, as stated previously. However, as shown in Fig. 8 this variation is linear for the temperatures with respect to the melting temperatures T_m (at $P = 0.1$ MPa) for the components M_1 to M_9 (Table 2) within the temperature interval $T - T_m \cong 20$ K according to the six experimental points [4] available for the analysis. This includes the pressure region of 0.1 to ~ 100 MPa for those components in n-tridecane. Most likely, for the pressures above 100 MPa,

correspondingly at higher temperatures, variation of $H(T)$ with the $T - T_m$ would turn into the quadratic (parabolic) according to Eq. (26) for all the components (M_1 to M_9) regarding the liquid-solid transition in n-tridecane. For our calculations of ψ , χ_ψ^{-1} , F , S , C and H as a function of $T - T_m$, the pressure varied with the temperature for the components M_1 to M_9 , starting from 0.1 to ~ 100 MPa on the basis of six experimental points [4], as shown in Fig. 2 ($T - T_m$ versus $P - P_m$).

In our treatment, calculation of the thermodynamic quantities studied here was based on the $T - X$ and $T - P$ phase diagrams of the liquid – solid transition in n-tridecane mixtures. The temperature dependence of the thermodynamic quantities of the order parameter, susceptibility, free energy, entropy, heat capacity and the enthalpy as predicted from the Landau phenomenological model, can be compared with the experimental measurements for the liquid – solid transition in n-tridecane (n-C₁₃ to n-C₁₉). Also, the pressure and composition dependence of those thermodynamic functions can be predicted for the liquid – solid transition in those mixtures by using the Landau model as studied here. This can be done by means of Eq. (15) for the $T - P$ dependence at $x = x_m$ (at the melting concentration) and also $T - x$ dependence at $P = P_m$ (at the melting pressure). Those dependences can be substituted into the temperature dependence of the order parameter ψ (Eq. (18)), the inverse susceptibility χ_ψ^{-1} (Eq. (21)), the free energy F (Eq. (23)), entropy S (Eq. (24)), the heat capacity C (Eq. (25)) and the enthalpy (Eq. (26)). One then obtains the pressure and concentration (mole fraction) dependence of those thermodynamic quantities for the liquid-solid transition in n-tridecane. These dependences expected from the Landau phenomenological model can be compared with the experimental data for n-tridecane. This provides the description of the phase transition mechanism in the tridecane system, particularly, the pressure effect on the phase transitions in some more details.

5. Conclusions

$T - X$ and $T - P$ phase diagrams were calculated by the Landau mean field theory for the solid – liquid phase equilibria in n-tridecane using the experimental data from the literature. On the basis of the phase diagrams calculated, the thermodynamic quantities of the order parameter, susceptibility, free energy, entropy, heat capacity and enthalpy were predicted as a function of temperature for the solid – liquid transition in n-tridecane ranging from n-C₁₃ to n-C₁₇ with various number of components.

Our calculations indicate that the Landau mean field model is adequate to describe the solid – liquid transition in those mixtures. The thermodynamic quantities predicted from the Landau model as studied here, can be compared with the experimental measurements for the n-tridecane when they are available in the literature. As an original work, calculating the phase diagrams and the thermodynamic quantities from the Landau mean field model led us to describe the mechanism of the solid-liquid transition in n-tridecane. Based on the experimental phase diagrams which were described adequately by the present model, predictions of the thermodynamic properties are also acceptable within the model for the solid-liquid transition in this system. Pressure and composition dependence of the thermodynamic quantities can also be studied for the solid – liquid equilibria in n-tridecane under the Landau phenomenological model

introduced here. The same approach can be performed for some other mixtures for their solid-liquid transition.

Nomenclature

T	temperature (K)
T_m	melting temperature (K)
x	concentration (mole fraction) (%)
x_m	melting concentration (%)
P	pressure (MPa)
P_m	melting pressure (MPa)
ψ	order parameter
χ_ψ	order parameter susceptibility
F	free energy (J/mol)
C, C_0	heat capacity (J/mol.K)
S, S_0	entropy (J/mol.K)
H, H_0	enthalpy (J/mol)
M	component



References:

- [1] M. Milhet, J. Pauly, J.A.P. Coutinho, M. Dirand, J.L. Daridon, "Liquid-solid equilibria under high pressure of tetradecane plus pentadecane and tetradecane plus hexadecane binary systems", *Fluid Phase Equilibria*, 235, 173-181, 2005.
- [2] K. Khimeche, Y. Boumrah, M. Benziane, A. Dahmani, "Solid-liquid equilibria and purity determination for binary n-alkane plus naphthalene systems", *Thermochimica Acta*, 444, 166-172, 2006.
- [3] G.C. Sekhar, P. Venkatesu, T. Hofman, M.V. P. Rao, "Solid-liquid equilibria of long chain n-alkanes (C18–C28) in N,N-dimethylacetamide", *Fluid Phase Equilibria*, 201, 219-231, 2002.
- [4] J.L. Daridon, J. Pauly, M. Milhet, "High pressure solid-liquid phase equilibria in synthetic waxes", *Phys. Chem. Chem. Phys.*, 4, 4458-4461, 2002.
- [5] U. Domanska, P. Morawski, R. Wierzbicki, "Phase diagrams of binary systems containing n-alkanes, or cyclohexane, or 1-alkanols and 2,3-pentanedione at atmospheric and high pressure", *Fluid Phase Equilibria*, 242, 154-163, 2006.
- [6] M. Krishnan, S. Balasubramanian, "n-heptane under pressure: Structure and dynamics from molecular simulations", *J. Phys. Chem. B*, 109, 1936-1946, 2005.
- [7] C. Ma, Q. Zhou, F. Li, J. Hao, J. Wang, L. Huang, F. Huang, Q. Cui, "Rotator phases of n-heptane under high pressure: Raman scattering and X-ray diffraction studies", *J. Phys. Chem. C*, 115, 18310-18315, 2011.
- [8] I. Denicolo, A.F. Craievich, J. Doucet, "X-ray diffraction and calorimetric phase study of a binary paraffin – C23H48-C24H50", *J. Chem. Phys.*, 80, 6200-6203, 1984.
- [9] G. Ungar, N. Masic, "Order in the rotator phase of normal alkanes", *J. Phys. Chem.*, 89, 1036-1042, 1985.
- [10] E. B. Sirota, "Rotator phases of the normal alkanes: An x-ray scattering study", *J. Chem. Phys.*, 98, 5809-5824, 1993.
- [11] E.B. Sirota, H.E. King, H.H. Shao, D.M. Singer, "Rotator phases in mixtures of n-alkanes", *J. Phys. Chem.*, 99, 798-804, 1995.

- [12] R.G. Snyder, G. Conti, H.L. Strauss, D.L. Dorset, "Thermally-induced mixing in partially microphase segregated binary n-alkane crystals", *J. Phys. Chem.*, *97*, 7342-7350, 1993.
- [13] E. B. Sirota, "Remarks concerning the relation between rotator phases of bulk n-alkanes and those of langmuir monolayers of alkyl-chain surfactants on water", *Langmuir*, *13*, 3849-3859, 1997.
- [14] P.K. Mukherjee, "Pressure effect on the rotator-II to rotator I transition of alkanes", *J. Chem. Phys.*, *130*, 214906, 2009.
- [15] D.S. Fu, Y.F. Liu, X. Gao, Y.L. Su, G.M. Liu, D.J. Wang, "Binary n-Alkane Mixtures from Total Miscibility to Phase Separation in Microcapsules: Enrichment of Shorter Component in Surface Freezing and Enhanced Stability of Rotator Phases", *J. Phys. Chem. B*, *116*, 3099-3105, 2012.
- [16] U. Zammit, M. Marinelli, F. Mercuri, S. Paoloni, "Analysis of the Order Character of the R-II-R-I and the R-I-R-V Rotator Phase Transitions in Alkanes by Photopyroelectric Calorimetry", *J. Phys. Chem. B*, *114*, 8134-8139, 2010.
- [17] D.S. Fu, Y.F. Liu, G.M. Liu, Y.L. Su, D.J. Wang, "Confined crystallization of binary n-alkane mixtures: stabilization of a new rotator phase by enhanced surface freezing and weakened intermolecular interactions", *Phys. Chem. Chem. Phys.*, *13*, 15031-15036, 2011.
- [18] I. Koljanin, M. Pozar, B. Lovrinevic, "Structure and Dynamics of liquid linear and cyclic alkanes: A molecular Dynamics study", *Fluid Phase Equilibria*, *550*, 113237, 2021.
- [19] B. He, V. Martin, F. Setterwall, "Liquid-solid phase equilibrium study of tetradecane and hexadecane binary mixtures as phase change materials (PCMs) for comfort cooling storage", *Fluid Phase Equilibria*, *212*, 97-109, 2003.
- [20] P. Morawski, J. A. P. Coutinho, U. Domanska, "High pressure (solid + liquid) equilibria of n-alkane mixtures: experimental results, correlation and prediction", *Fluid Phase Equilibria*, *230*, 72-80, 2005.
- [21] L. Robles, D. Mondieig, Y. Haget, M. A. Cuevas-diarte, X. Alcobé, "Non isomorphism and miscibility in the solid state: Determination of the equilibrium phase diagram n-octadecane C₁₈H₃₈ + n-nonadecane C₁₉H₄₀", *Mol. Cryst. Liq. Cryst.*, *281*, 279-290, 1996.
- [22] S.N. Gunasekara, S. Kumova, J.N. Chiu, V. Martin, "Experimental phase diagram of the dodecane-tridecane system as phase change material in cold storage", *Int. J. Ref.*, *82*, 130-140, 2017.
- [23] T. Shen, H. Peng, X. Ling, "Experimental Measurements and Thermodynamic Modeling of Melting Temperature of the Binary Systems n-C11H24-n-C14H30, n-C12H26-n-C13H28, n-C12H26-n-C14H30, and n-C13H28-n-C-15 H-32 for Cryogenic Thermal Energy Storage", *Ind. Eng. Chem. Res.*, *58*, 15026-15035, 2019.
- [24] T. Shen, S. Li, H. Peng, X. Ling, "Experimental study and thermodynamic modeling of solid-liquid equilibrium of binary systems: Dodecane-tetradecane and tridecane-pentadecane for cryogenic thermal energy storage", *Fluid Phase Equilibria*, *493*, 109-119, 2019.
- [25] H. Yurtseven, E. Kilit Dogan, "Calculation of the phase diagram of n-alkanes (C_nH_{2n+2}) by the Landau mean field theory", *Fluid Phase Equilibria*, *556*, 113377, 2022.
- [26] H. Yurtseven, T. Emirosmanoglu, O. Tari, "Calculation of the Liquid-Solid Phase Diagram and the Thermodynamic Quantities of the Binary System of Tetradecane and Hexadecane Using the Mean Field Theory", *J. Sol. Chem.*, *50*, 1335-1362, 2021.
- [27] O. Tari, H. Yurtseven, "Calculation of the T-X phase diagram of tetradecane+hexadecane and tetradecane+pentadecane under high pressure by the landau mean field theory", *Fluid Phase Equilibria*, *559*, 113499, 2022.
- [28] P.K. Mukherjee, "Tricritical behavior of the R-I-R-V rotator phase transition in a mixture of alkanes with nanoparticles", *J. Chem. Phys.*, *135*, 134505, 2011.

Review Article

Energy Structure Theory: A General Unified Thermodynamics Theory

¹*S. Shahsavari , ²S. M. A. Boutorabi 

^{1,2} School of Metallurgy and Material Engineering, Iran University of Science and Technology, Tehran, Iran
E-mail: ¹*shahsavari_saeed70@mail.iust.ac.ir

Received 28 February 2023, Revised 5 July 2023, Accepted 7 July 2023

Abstract

This study, while reviewing some of the established unified equations and fundamentals of the energy structure and providing a detailed interpretation of their physical concepts, expands the relevant equations for new topics and applications, and in fact, establishes novel results and equations from the energy structure analysis. In fact, this paper establishes an energy components-based-general model inspired by the first and second laws of thermodynamics as well as using a new division to the total energy of the system. The established model is completed by extracting the physical direction for the feasible processes based on the energy components of the system. As two of the most important achievements of the energy components approach, using a new quasi-statistical approach as well as a novel energy conservation principle, an entropy equation is gained that has a common basis as the Boltzmann entropy equation as well as a general solution to the different formulations of the second law of thermodynamics is established. The established equations are gained without any limiting assumptions, and are governed to any physical system. Several basic examples have been studied, and matching the obtained results with expected ones is shown.

Keywords: *Unified thermodynamics; high particle number systems; dependent energy components; energy structure equation; feasible processes; compatibility conditions; Boltzmann entropy equation.*

1. Introduction

While the principles of motion determine the relationship between forces and accelerations, the principle of energy conservation, as a unifying principle in physics, with respect to kinetic energies, different potential energies, etc., examines the general behavior of the system due to exchange energy with the surrounding [1-2]. Of course, this issue can also be raised in thermodynamics. [1]. Two thermodynamic laws were developed by Clausius in 1865[3]. The first law of thermodynamics is a result of the principle of energy conservation for thermodynamic cycles and states that the sum of work done and heat exchange in a closed cycle is equal to zero. While the second law of classical thermodynamics examines the feasibility of thermodynamic processes. Clausius [3] using the concept of entropy, stated the second law as a prediction of the increase of entropy in physical processes, and it is based on the fact that based on the second law, it is necessary that the entropy of the universe is always increasing. In fact, the second law of thermodynamics is also referred to as a summary of all laws governing nature [3]. The use of the above expression in scientific theories is not easy as we know that Isaac Newton does not pay attention to entropy in compiling the principles of mechanics, in other words, classical mechanics are written reversibly [4]. Certainly, there are ideas for applying the second law on the mechanic and thermodynamic coupling problems on a macroscopic scale, based on thermodynamic entropy [5]. The second law has attracted many scholars and has not lost its credibility even with the advent of advanced scientific theories [6,7]. Various mathematical models are proposed for the second law of thermodynamics [8,9]. It has

also been proven in various ways [10]. Some of these methods are based on statistical mechanics and some on the basis of quantum mechanics. However, in the quantum mechanical science, the law entitled "the generalization of the second law of thermodynamics" is formulated and presented, as well as the thermodynamic concept for negative entropy [11]. Today, the concept of entropy is wider than that defined by Clausius which is referred to as thermodynamic entropy, while some researchers have also defined entropy in addition to thermodynamic entropy that is used in relevant scientific fields to investigate problems [12,13]. These definitions are based on the energies that are involved in the relevant issues and the entropy changes depend on these energy changes. Processes in which entropy production is present are referred to as irreversible processes. The reasons of process irreversibility can be seen microscopically in theories that are used to prove the second law [8, 11]. In the macroscopic view, the existence of friction, the heating of a system with a finite rate, the presence of a temperature gradient, and etc., are considered as factors that cause the irreversibility of a process as well as entropy production [14-16]. Change in the structure and properties of the system can be considered as the main factors that cause the irreversibility in the microscopic view. These factors are the base of analysis in some branches of science such as Tribo-fatigue, unified mechanics theory, and also mechanothermodynamics [17-19]. In mechanothermodynamics, as a new branch of physics, an entropy is defined which is used as the base of MTD system analysis [20]. Also, energy and entropy are two main quantities to understand nanoparticle behavior [21]. In

addition, other quantities are including of chemical potential, strongly affecting the solubility, nucleation, and stability of the nanoparticle. Also, these quantities can be coupled with Gibbs free energy [21-23]. To investigate nanoparticle behavior from the perspective of the energy application, chosen element structure can have a very important role [24-25]. Moreover, in statistical physics, entropy is considered as a function of attainable states of the system at the corresponding energy level [26]. Achievable states can be calculated at the corresponding energy level using quantum concepts as well as probability theory [26]. Considering the assumptions of statistical physics, Boltzmann calculated her entropy equation in terms of attainable states of the system at the corresponding energy level [27]. Boltzmann equation can be used in general in particle systems as well as continuous media. This equation can be generally used to calculate entropy changes in reversible and irreversible processes and is not directly dependent on energy losses in the performed process. According to the basis of statistical physics, in order to study the energy losses in particle systems, the dynamics of system particles can be investigated [29-31]. Various cases have been observed both in the scientific position and in the applied position of scientific principles in nature, which require the simultaneous mastery of the first and second laws of thermodynamics as governing principles. As an example, the formation of two-layer oxide films in the material structure can be mentioned [32-40]. Double layer oxide films with their outstanding features are still in the stage of being known. However, according to what is known so far about these films and the conditions of their formation, they are formed in a highly irreversible process, and in fact, in their analysis, the results related to the energy conservation principle cannot be considered for these issues, and in fact, reaches obvious, and of course, inapplicable results in the study of these films. Therefore, in this situation, the practical role of the second law of thermodynamics, and of course, the role of coupled equations and the possibility of their applicability become very important. In this situation, there are various challenges that researchers are working on. For example, the unequal form of the second law generally cannot be used as an equation that can be applied in problems, in order to obtain the behavior of the system in a specific energy exchange with the surroundings. In fact, the relevant form is in the position of checking the feasibility of a physical solution for the behavior of the studied system. Also, the existence of different expressions and formulations for the second law of thermodynamics brings many practical and scientific challenges [41-55]. Attempts have been made to find a general solution for various expressions of the second law of thermodynamics in terms of system energy components for physical processes [56]. Also, the energy components of the system have been used to provide a quasi-statistical equation for entropy, such that the corresponding equation has the same basis as Boltzmann's entropy equation [57]. In fact, we can apply some of the effects of the second law on the energy structure of the system using its energy components [50,56,58-59]. Borchers presents his equations by considering mechanical and thermal variables in order to determine the behavior of the system in the representation of its internal energy, and also, using the relevant mathematical structure resulting from the definition of entropy in the second law of thermodynamics [60]. In this respect, the energy structure approach can be similar to Borchers approach. In fact, according to the achievements that have

been obtained from the perspective of the energy structure, the issue of its expansion and completion can be very valuable. References [50,56-59] provide the equation of energy structure with the assumptions of irreversibility in a physical process, and are used to provide the quasi-statistical equation for entropy as well as the different expressions of the second law of thermodynamics. In this study, the energy structure equation is extracted with the relevant mathematical analysis process, and used to define a new energy space. Feasible processes are investigated, and system compatibility conditions are derived. Also, the dynamic energy definition of the system is provided based on the extracted energy structure, from which valuable results can be obtained on the behavior of physical systems from the point of view of its energy components. The relevant perspective provides a simultaneous view of the first and second laws of thermodynamics, and is used in the energy coordinates of the system in order to express the processes that can be performed as a result of energy exchange with the surrounding. Another issue that results from this point of view is determining the structure of irreversibility, and also, defining the components of irreversibility. The analysis of irreversibility in a physical process using the energy structure equation is available in reference [59]. In this paper, according to the mathematical process established for deriving the equation of the energy structure as well as the definition of the new dynamic energy component and system compatibility conditions, a more comprehensive approach to the results presented for the analysis of irreversibilities is obtained. Finally, it must be noted that one of the goals of the energy structure perspective is to try to improve the relevant forms to express the energy of the system by providing its equations on the basis of the activated energy components and their structure and apply the governed principles that have recently become one of the challenges of scientists regarding the correct forms of the first and second laws of thermodynamics are converted, as well as the mathematical errors corresponding to these laws.

2. Notations and Definitions

In this part, the most important used concepts and notations are defined. At the first step, we need to provide a standard formulation to the first law of thermodynamics.

2.1 N.D.1. Energy Space

Energy space is combined of the all activated and non-activated energy components of the system in the performed process. During a physical process, one of the sub-spaces of the energy space participates in the performed process. All analysis are done based on the energy space of the system, and relations are written based on the independent and dependent energy components of the system. Notation u_i is used for energy components of system.

2.2 N.D.2. Independent Energy Components

For a performed process, independent energy components are that components that are activated independently of that how energy is applied to the system. In fact, these components are the basis of the performed process, and will be activated in all conditions of energy applying for the considered process.

2.3 N.D.3. Dependent Energy Components

Dependent energy components can be activated dependently to the independent energy components. In fact, these components are dependence that how energy is applied to the system, and also can be ranged as value-dependence ($g_j = g_j(u_1, u_2, \dots, u_m)$) and rate-dependence ($h_p = h_p(\dot{u}_1, \dots, \dot{u}_m)$) to the independent energy components activated in the performed processes. Where m is number of the activated independent energy components.

2.4 N.D.4. Energy Structure Equation

Energy structure equation is established and developed as an equation that can formulate the performed processes using activated, independent and dependent, energy components of the system, and also shows their dependence. Therefore, energy structure equation is used to study the physical processes from the perspective of the energy space of the system.

2.5 N.D.5. Quasi-Static Path

In a quasi-static path, energy is applied to the system with a zero rate. In fact, for independent components, it can be considered that in a quasi-static path $\dot{u}_i \cong 0$. This path is used as a reference path, and other paths are studied using comparison with the quasi-static path. In this path, only independent and value-dependence energy components can be activated.

2.6 N.D.6. General Paths

In a general path, energy is applied to the system with a non-zero rate (Or $\dot{u}_i \neq 0$).

2.7 N.D.7. Particular Process

All processes that have the same active independent energy components.

2.8 N.D.8. Various Conditions

All conditions that same energy amount is applied to the system.

3. Energy In A Physical System

When the principle of energy conservation is used for a physical problem, at first, it is necessary to express the proper term for the system energy, which includes those participating in the processes that are possible for the system and will change through. The principle of energy conservation relates these changes to each other as well as the exchange of energy with the environment. For example, when the principle of mechanical energy conservation is to be applied, the total mechanical energy is considered as a sum of potential energies and kinetic energy [61].

$$E_M = U_{sys} + K_{sys} \quad (1)$$

In that E_M is the total mechanical energy, U_{sys} and K_{sys} are respectively potential energy and kinetic energy. In this case, the principle of energy conservation states that the total energy change rate is equal to the exchange rate of energy with the environment.

If the desired problem has thermal effects too, then in writing the principle of energy conservation, it is necessary to consider the terms related to heat exchange. For a unit mass of the body, if dH is the variation in the heat collected, dE is the internal energy variation, dW of the work performed by the external forces, dV is the change of the

kinetic energy stored and dR is the heat changes transformed to the environment, then the principle of energy conservation is thus written [1]:

$$dH = dE + dW + dV + dR \quad (2)$$

Equation (2) identifies the relationship between the intrinsic, thermal and kinetic energy changes of the system to the work done and changes in the heat exchanged with the surrounding environment.

As an example, it can be argued that a vulnerable solid object can exchange heat with the surrounding environment. Sosnovsky [12] named these systems as mechanothermodynamic systems. He also considered the energy of the whole to analyze the mechanothermodynamic systems as follows:

$$E = E_T + E_M \quad (3)$$

Where E is the total energy, E_T and E_M are respectively thermal and mechanical energy. He used this expression to determine the mechanothermodynamic entropy.

In this paper, it is assumed that the total energy for the system can be considered as follows, as shown in figure 1:

$$U_T = U_{ND} + U_D \quad (4)$$

That U_T is the total energy, U_D is the dynamic energy and U_{ND} is the sum of all other types of energy. Fig 1 takes a scheme of this division:

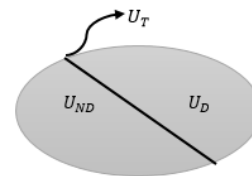


Figure 1. A new division of the total energy.

Dynamic energy is the sum of energies that are directly related to the inertia of the system. Non-dynamic energy is also the sum of energies that are not directly related to the inertia of the system and are related to the deformation of the system and its displacement. Energies such as the potential energy of the massless spring, the energy associated with the massless damper, the energy associated with changing the distance between the plates of a massless capacitor, etc. are the examples of non-dynamic energy. A component of the kinetic energy such as kinetic energy of a moving rigid body could be an example of dynamic energy, because it is directly related to the inertia of the system. This division enables us to apply the effects of the surrounding environment on the equation governing the behavior of the system, thus representing each physical process as a term appropriate for dynamic and non-dynamic energies. This manner of presentation allows us to incorporate the internal structure of the system and the processes that can be implemented for it in terms of non-dynamic energies.

Eq. (4) introduces a new approach for investigating the total energy of the system which its base is the direct dependence on the inertia of the system. Each energy type in this equation whether dynamic or non-dynamic could be divided into different components e.g. in studying damage of mechanothermodynamic systems, irreversible effective

energy in damage will be one of them, therefore this equation is more general than any other relation considering only a phenomena such as tribo-fatigue.

Using this assumption, a study on the energy structure of physical systems can be performed.

4. Non-Dynamic Energy Structure

In physical systems, the concepts of reversibility and irreversibility are an important issue for the performed process. It is in this situation that paying special attention to irreversibility factors has a special place [28-31]. In fact, physical processes are generally irreversible and this issue needs to be considered especially in the basis of the governing equations. Figure 2 shows a physical system in energy exchange with the surrounding environment and also according to its energy components:

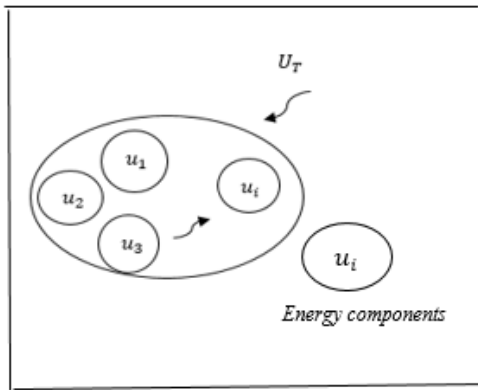


Figure 2. Scheme of a physical system with its energy components.

In Figure 2, a physical system with its non-dynamic energy components is shown. This system receives some energy from its surrounding. The total non-dynamic energy for the system can be expressed as follows:

$$U_{ND} = \sum_i u_i \quad (5)$$

That u_i is a non-dynamic energy component.

In a process performed by the system, some of the energy components remain constant, some others change independently in the process, and remaining will also change as a function of independent components. Therefore, assuming that the first m components are independently participating in the process, k components are the dependent ones, and the other components remain unchanged, the non-dynamic variation can be written as follows:

$$\delta U_{ND} = [\delta u_1 + \delta u_2 + \dots + \delta u_m] + [\delta u_{m+1} + \dots + \delta u_{m+k}] + 0 \quad (6)$$

Assuming that the process is quasi-static ($\dot{u}_i \cong 0$), then the dependent components can be rewritten as follows, as shown in figure 3.

$$\delta g_j \equiv \delta u_{m+j} \quad (7)$$

That:

$$g_j = g_j(u_1, u_2, \dots, u_m) \quad (8)$$

So the Eq. (6) can be rewritten as follows:

$$\delta U_{ND} = [\delta u_1 + \delta u_2 + \dots + \delta u_m] + [\delta g_1 + \dots + \delta g_k] \quad (9)$$

By calculating the non-dynamic energy of the Eq. (9):

$$U_{ND} = (u_1 + u_2 + \dots + u_m) + [g_1 + \dots + g_k] + U_{T_0} \quad (10)$$

That U_{T_0} is the sum of all the energies that have not participated in the process:

$$U_{T_0} = \sum_i u_{m+k+i} \quad (11)$$

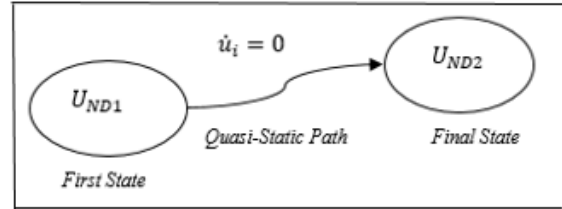


Figure 3. Non-dynamics energy change in the quasi-static process.

Path 1-2 is an ideal path on which the variations of the independent components occur in a quasi-equilibrium state. The quasi-static path occurs with remaining the system in internal equilibrium, even for an ideal process to be performed it could be supposed that infinite time is needed. As expected, in this case the relationship between the energy components is independent of time (because the functions g_j do not depend on time).

And in general case ($\dot{u}_i \neq 0$), as shown in figure 4, the following statement is used:

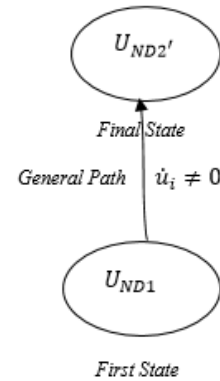


Figure 4. Non-dynamics energy change in general case.

$$U_{ND} = (u_1 + u_2 + \dots + u_m) + [g_1 + \dots + g_k] + [h_1 + \dots + h_n] + U_{T_0} \quad (12)$$

$$h_p = h_p(\dot{u}_1, \dots, \dot{u}_m) \quad (13)$$

Based on the Eq. (12), can be named **Energy Structure Equation**, in a physical process, the energy components that are activated can depend on the rate of energy applied to the system by the environment, and also on how it is applied, as well as the internal structure of the system. Eq. (12) states that in a non-static state, the energy given to the system is divided into more components than the static state.

The changes in Eq. (12) can be expressed as follows:

$$\delta U_{ND} = \sum_{i=1}^m \delta u_i + \sum_{j=1}^k \left(\frac{\partial g_j}{\partial u_1} \delta u_1 + \dots + \frac{\partial g_j}{\partial u_m} \delta u_m \right) + \sum_{p=1}^n \left(\frac{\partial h_p}{\partial \dot{u}_1} \delta \dot{u}_1 + \dots + \frac{\partial h_p}{\partial \dot{u}_m} \delta \dot{u}_m \right) \quad (14)$$

As δU_T is exchanged between system and surrounding, activated energy components will change based on how energy is applied to the system. So, considering this process, Eq. (15) can take the variations of the activated independent energy components (δU_T is not necessarily heat or work, and in general it can be a combination of them or the cause of a variation in the independent components of energy):

$$\begin{aligned} \delta u_1 &= \alpha_1 \delta U_T \\ &\vdots \\ \delta u_m &= \alpha_m \delta U_T \end{aligned} \quad (15)$$

The coefficients α_i can be named as loading coefficients that depend on how energy is applied to the system. Therefore, by assuming that:

$$\alpha = \left[\sum_{i=1}^m \alpha_i \left(1 + \sum_{j=1}^k \frac{\partial g_j}{\partial u_i} \right) \right] + \left[\sum_{i=1}^m \dot{\alpha}_i \left(\sum_{p=1}^n \frac{\partial h_p}{\partial \dot{u}_i} \right) \right] \quad (16)$$

$$\beta = \sum_{i=1}^m \alpha_i \left(\sum_{p=1}^n \frac{\partial h_p}{\partial \dot{u}_i} \right) \quad (17)$$

Equation (14) can be rewritten as follows:

$$\delta U_{ND} = \alpha \delta U_T + \beta \delta \dot{U}_T \quad (18)$$

The coefficients α and β depend on the amount and rate of energy applied to the system, as well as the inherent properties of the system. δU_T is not necessarily heat or work, and in general it can be a combination of them or the cause of a variation in the independent components of energy.

Equation (18) can also be expressed as:

$$\dot{U}_{ND} = \alpha \dot{U}_T + \beta \ddot{U}_T \quad (19)$$

Equation (19) depends on the variation of non-dynamic energies to the amount and variation of the rate of the energy that applied from the environment to the system as well as the coefficients α and β .

As an example, in one degree of freedom vibrational systems [30], the potential energy depends on the displacement of the mass while the dissipated energy depends on the velocity. Therefore, by assuming the potential energy as the independent energy component, the dissipated energy could be considered as the dependent one. It is also notable that some of these energy components could be considered as non-dynamic energy of the system.

The energy structure equation is based on the energy components of the system as well as the way of energy exchange between the system and the surrounding environment. In fact, according to the energy structure equation, in a physical process, some components are activated independently, and some participate in the physical process depending on the independent components, and the rest of the components remain inactive. Dependent components can be a function of the amount or rate of independent components. The components dependent on the rate of change of the independent components, in fact, show the irreversibility aspects of the performed physical process.

The energy structure perspective has no contradiction with the second law of thermodynamics. In fact, based on sub-structural approaches to the second law of thermodynamics [62-64], the perspective of energy structure is in complete agreement with this law.

5. Feasible Processes

In order to study the performed processes, classical thermodynamics considers their initial and final states, and heat exchange and work done in different paths are studied. Therefore, for thermodynamic processes with transferred heat and work done, as well as considering constant initial and final states, in paths that have similar initial and final states, the internal energy changes are equal, although the heat exchanged and also the work done in these paths are different, as shown in figure 5.

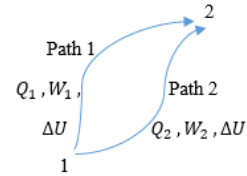


Figure 5. System behavior in different paths with fixed first and final states.

In this approach, as shown in figure 6, the energy exchanged between the system and the surrounding environment is considered equal in different paths, and the changes of the energy components in these paths are studied.

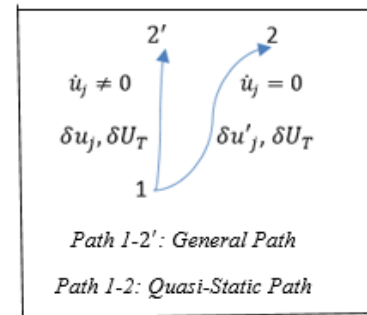


Figure 6. System behavior by applying the same energy in different paths.

To investigate the feasible processes, same amounts of energy are applied to a system in two different paths and thus the variation of the energy components will be compared. In fact, it is assumed that the variations of non-dynamic energies are equal in these two different paths and then the variations of independent components will be studied. In other words, the perspective of the energy structure studies the paths that have equal energy exchange and derives the governing condition for the feasible processes based on the energy components of the system.

As shown in figure 6, if Eq. (9) and Eq. (14) are equaled when the component u_j is the only independent component of the process, then the following relation can be concluded (That δu_j takes the variation of component u_j in general path ($\dot{u}_j \neq 0$) for the case that δU_T is exchanged between system and surrounding. Also, $\delta u'_j$ takes the variation of component u_j for the quasi-static path ($\dot{u}_j \cong 0$) for the case that δU_T is exchanged between system and surrounding.):

$$\delta u_j + \sum_{i=1}^k \left(\frac{\partial g_i}{\partial u_j} \delta u_j \right) + \sum_{p=1}^n \left(\frac{\partial h_p}{\partial u_j} \delta \dot{u}_j \right) = \delta u'_j + \sum_{i=1}^k \left(\frac{\partial g_i}{\partial u_j} \delta u'_j \right) \quad (20)$$

Therefore:

$$\left(1 + \sum_{i=1}^k \left(\frac{\partial g_i}{\partial u_j}\right)\right) (\delta u_j - \delta u'_j) = - \left(\sum_{p=1}^n \left(\frac{\partial h_p}{\partial \dot{u}_j}\right)\right) \delta \dot{u}_j \quad (21)$$

$$- \left[\frac{\left(\sum_{p=1}^n \left(\frac{\partial h_p}{\partial \dot{u}_j}\right)\right)}{\left(1 + \sum_{i=1}^k \left(\frac{\partial g_i}{\partial u_j}\right)\right)} \right] = \frac{(\delta u_j - \delta u'_j)}{\delta \dot{u}_j} \quad (22)$$

$$- \left[\frac{\left(\sum_{p=1}^n \left(\frac{\partial h_p}{\partial \dot{u}_j}\right)\right)}{\left(1 + \sum_{i=1}^k \left(\frac{\partial g_i}{\partial u_j}\right)\right)} \right] \left(\frac{\delta u_j - \delta u'_j}{\dot{u}_j}\right) = \frac{(\delta u_j - \delta u'_j)}{\delta \dot{u}_j} \left(\frac{\delta u_j - \delta u'_j}{\dot{u}_j}\right) \quad (23)$$

$$\left[\frac{\left(\sum_{p=1}^n \left(\frac{\partial h_p}{\partial \dot{u}_j}\right)\right)}{\left(1 + \sum_{i=1}^k \left(\frac{\partial g_i}{\partial u_j}\right)\right)} \right] \left(\frac{\delta u_j - \delta u'_j}{\dot{u}_j}\right) = - \frac{(\delta u_j - \delta u'_j)^2}{\dot{u}_j \delta \dot{u}_j} = -2 \frac{(\delta u_j - \delta u'_j)^2}{\delta (\dot{u}_j)^2} \quad (24)$$

Therefore, since a quasi-static path is used as reference path:

$$\left[\frac{\left(\sum_{p=1}^n \left(\frac{\partial h_p}{\partial \dot{u}_j}\right)\right)}{\left(1 + \sum_{i=1}^k \left(\frac{\partial g_i}{\partial u_j}\right)\right)} \right] \left(\frac{\delta u_j - \delta u'_j}{\dot{u}_j}\right) \leq 0 \quad (25)$$

The terms $\left(\sum_{p=1}^n \frac{\partial h_p}{\partial \dot{u}_j}\right)$ and $\left(\frac{\delta u_j - \delta u'_j}{\dot{u}_j}\right)$ are actually a description of the more energy distribution in applying energy to the system at a non-zero rate. The term $\left(1 + \sum_{i=1}^k \frac{\partial g_i}{\partial u_j}\right)$ also depends on the internal structure of the system and does not depend on the rate of energy applying.

Relationship (25) is established for any process that the system experiences. This inequality is expressed in the following Eq. (18) and shows that a physical system cannot experience any arbitrary process and inequality (25) must be established. This condition is very similar to the second law of thermodynamics, which states that in real processes, some entropy will always be generated.

Relationship (25) can also be considered as a constraint on processes performed by the system.

6. A Novel Energy Conservation Principle

Borchers considered the law of conservation of energy in terms of mechanical and thermal variables [60]. The perspective of energy structure actually uses energy components by considering the related dependence structure in order to express the energy of system. In fact, one of the achievements of the energy structure perspective mentioned in the references is providing a new expression for the energy conservation principle using a standard formulation to the first law of thermodynamics [50,57,65-66]. In this part, a brief overview of this statement is provided. Considering figure 7.

$$\delta U_j = \delta u_j - \delta u'_j \quad (26)$$

So, relation (25) takes:

$$\left[\frac{\left(\sum_{p=1}^n \left(\frac{\partial h_p}{\partial \dot{u}_j}\right)\right)}{\left(1 + \sum_{i=1}^k \left(\frac{\partial g_i}{\partial u_j}\right)\right)} \right] \left(\frac{\delta U_j}{\dot{u}_j}\right) \leq 0 \quad (27)$$

Or:

$$\left[\frac{\left(1 + \sum_{i=1}^k \left(\frac{\partial g_i}{\partial u_j}\right)\right)}{\left(\sum_{p=1}^n \left(\frac{\partial h_p}{\partial \dot{u}_j}\right)\right)} \right] \left(\frac{\delta U_j}{\dot{u}_j}\right) \leq 0 \quad (28)$$

Eq. (28), like Borchers equations [60], in addition to energy exchange, depends on the internal structure of the system as well as the way of energy exchange. Eq. (28) is general in system energy coordinates and according to the energy structure equation, and it is obtained without any limiting assumption. These conditions are provided in Borchers unified view in terms of mechanical and thermal variables that can provide a complete description of the system.

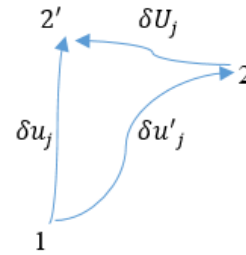


Figure 7. Difference between two different paths [65].

7. The Physical Significance of Entropy

Borchers considered the law of conservation of energy in terms of mechanical and thermal variables [60]. The perspective of energy structure

The second law can be expressed as follows [67]:

$$\oint \frac{\delta Q}{T} \leq 0 \quad (29)$$

Where δQ is the heat exchanged at temperature T . Also, for a continuous distribution of matter:

$$\frac{d}{dt} \int_p \rho s dV \geq \int_p \rho e dV - \int_{\partial p} \frac{q_i n_i}{T} da \quad (30)$$

So, in the differential form:

$$\frac{ds}{dt} - e - \frac{1}{\rho} \left(\frac{q_i}{T}\right)_{,i} \geq 0 \quad (31)$$

Where p is a material particle, and ∂p is the surface containing the volume of the particle p . Also, e is the rate of entropy entry from surrounding surface by external sources per unit mass of the material, q_i is the heat flux vector passing through the unit surface, ρ is density, n_i is the normal vector of surface, T is temperature, and s is entropy of the considered material point.

The equality state is for reversible processes, and the inequality state is for irreversible processes. Among the most important equations of classical thermodynamics in order to study irreversibility in performed process, Eq. 32 can be considered: [68]:

$$\vec{I}_k = \sum_l L_{kl} \vec{F}_l \quad (32)$$

Where \vec{I}_k is a set of general currents and \vec{F}_l is thermodynamic forces. Also, L_{kl} is a matrix of kinematic coefficients. For matrix L_{kl} it is required to satisfy the

symmetry equations in the OSAGER equations [69]. In this perspective, the irreversibility is studied using investigating the sub-structures of the system.

However, when there is no irreversibility in the performed process, Eq. (33) takes the entropy change in the process:

$$Tds = dQ \quad (33)$$

Based on the second law of thermodynamics, $ds \geq \frac{dQ}{T}$ or $ds_{gen} \geq 0$, that s_{gen} is the entropy generated, and must be always positive in all feasible process. The entropy generated is the basis for studying the amount of available work lost. In fact, irreversibility in a physical process is directly related to the amount of entropy production. The generated entropy increases the amount of thermal energy of the system, and this can be studied in the increase of changes related to the dependent components h_p activated in the performed process. The amount of irreversibility is considered as $T_0 \delta S_{gen}$ that is defined based on entropy generation and the environment temperature [67].

From the perspective of the statistical physics, Planck's theorem, entropy is considered as a function of the probability [70]. So:

$$S = f(W) \quad (34)$$

Where S is entropy, and W is the probability. Based on the considered properties for entropy, function f must satisfies the following conditions [70]:

$$S = S_1 + S_2 \quad (35)$$

$$f((W_1 \cdot W_2)) = f(W_1) + f(W_2) \quad (36)$$

That W_1 and W_2 are probabilities of sub-systems 1 and 2. So:

$$S = k \ln(W) + \text{constant} \quad (37)$$

That k is a constant. Plank equation for entropy is [26]:

$$S = k[(N + P) \ln(N + P) - N \ln(N) - P \ln(P)] \quad (38)$$

That N is resonators, and P is an integer. The equation of probability has been provided with diferent approaches [27]. As an example, Fermi-Dirac provide the following equation:

$$W = \prod_j \frac{g_j!}{(g_j - 1)! N_j!} \quad (39)$$

That N_j is the number of particles with the weighting factor of energy level g_j . Statistical mechanics determines the absolute value of entropy according to the energy levels of its constituent elements. In this view, the energy level of each particle is considered as a variable, and according to the set of all energy levels, statistical mechanics will be able to calculate the absolute value of entropy.

8. Energy Component's Approach to the Boltzmann Entropy Equation

Borchers considered the law of conservation of energy in terms of mechanical and thermal variables [60]. The perspective of energy structure

As one of the achievements of the energy structure perspective in the references, it is the presentation of the quasi-statistical equation of entropy, which has a common basis as Boltzmann's entropy equation [57]. In this section, a brief overview of this equation is provided. Figure 8 shows a scheme of the energy components approach:



Figure 8. Energy Component's approach for particles. system [57].

Considering Eq. (26) and rewriting Eq. (21):

$$\left(1 + \sum_{i=1}^k \left(\frac{\partial g_i}{\partial u_j}\right)\right) (\delta U_j) = - \left(\sum_{p=1}^n \left(\frac{\partial h_p}{\partial u_j}\right)\right) (\delta \dot{U}_j) \quad (40)$$

So, if Eq. (40) is replaced in the relation (28):

$$\left(-\frac{\delta \dot{U}_j}{\dot{U}_j}\right) \leq 0 \quad (41)$$

Or:

$$\delta[\ln(\dot{U}_j)] \geq 0 \quad (42)$$

Because it is necessary that the relation (42) be established for each independent activated component, so relation (43) can be derived:

$$\delta[\ln(\dot{U}_1)] + \delta[\ln(\dot{U}_2)] + \dots + \delta[\ln(\dot{U}_m)] \geq 0 \quad (43)$$

Therefore:

$$\delta[\ln(\prod_{j=1}^m \dot{U}_j)] \geq 0 \quad (44)$$

Considering $w_{u_j} = \dot{U}_j$, and also $W_u = \prod_{j=1}^m w_{u_j}$, therefore:

$$\delta[\ln(W_u)] = \delta[\ln(\prod_{j=1}^m w_{u_j})] = \sum_{j=1}^m \delta \ln(w_{u_j}) \geq 0 \quad (45)$$

Finally, as the Boltzmann equation, the quasi-statistical definition of entropy can be provided as follows:

$$\delta S = K_{MS} \delta[\ln(W_u)] \quad (46)$$

Where K_{MS} is a universal constant. The quasi-statistical equation of entropy relates entropy changes to the rate of energy components that are measured relative to the quasi-static path. It also obtains entropy changes depending on the amount and manner of energy exchange. Also, applicability for systems with a continuous distribution of matter as well

as the amount of acceptable calculations can be mentioned as two features of this equation [57].

9. Dynamic Energy and Compatibility Conditions of System

Using Eq. (4), the variation of the dynamic energy in a process can be written as follows:

$$\delta U_D = \delta U_T - \delta U_{ND} \quad (47)$$

By placing the Eq. (18) in (47):

$$\delta U_D = (1 - \alpha)\delta U_T - \beta\delta\dot{U}_T \quad (48)$$

Eq. (48) shows the dependence of the dynamic energy variation to the amount and rate of energy applied from the environment to the system as well as the coefficients α and β . By using Eq. (15) dynamic energy can also be written in terms of independent components:

$$\delta U_T = \frac{\delta u_j}{\alpha_j}, 1 \leq j \leq m, \alpha_j \neq 0 \quad (49)$$

$$\delta\dot{U}_T = \left(\frac{1}{\alpha_j}\right)\delta\dot{u}_j - \left(\frac{\dot{\alpha}_j}{\alpha_j^2}\right)\delta u_j \quad (50)$$

Therefore:

$$\delta U_D = \left[\left(\frac{1-\alpha}{\alpha_j}\right) + \left(\frac{\beta\dot{\alpha}_j}{\alpha_j^2}\right)\right]\delta u_j - \left(\frac{\beta}{\alpha_j}\right)\delta\dot{u}_j \equiv \gamma_j\delta u_j + \gamma_j'\delta\dot{u}_j \quad (51)$$

Eq. (51) gives the variation of dynamic energy in terms of the independent component of u_j and its changing rate. γ_j and γ_j' are the coefficients of influence of δu_j and $\delta\dot{u}_j$ on the variation of the dynamic energy of the system. The dependence of dynamic energy on the rate of the independent energy components indicates the possibility of more energy distribution by increasing the rate of applied energy to the system. The following relationship will also exist between the independent energy components:

$$\gamma_j\delta u_j + \gamma_j'\delta\dot{u}_j = \gamma_i\delta u_i + \gamma_i'\delta\dot{u}_i, 1 \leq i, j \leq m \quad (52)$$

The Eq. (52) indicates possible paths for independent energy components. This equation can be rewritten as follows:

$$(\gamma_j\delta u_j - \gamma_i\delta u_i) = (\gamma_i'\delta\dot{u}_i - \gamma_j'\delta\dot{u}_j) = \mu_{ij} \quad (53)$$

Where μ_{ij} is a scalar that depends on the performed process as well as δu_i and δu_j components. For a process performed by the system, each of the m independent components should be analyzed with $(m-1)$ other components by using the Eq. (52). Therefore, the number of $\frac{m(m-1)}{2}$ values could be calculated for μ_{ij} . These $\frac{m(m-1)}{2}$ equations state the compatibility conditions of the system that must be satisfied for the performed process.

If $\mu_{ij} = 0$ and $\gamma_j, \delta u_i, \delta\dot{u}_i, \gamma_j' \neq 0$:

$$\frac{\delta u_j}{\delta u_i} = \frac{\gamma_i}{\gamma_j} \quad (54)$$

And also:

$$\frac{\delta\dot{u}_j}{\delta\dot{u}_i} = \frac{\gamma_i'}{\gamma_j'} \quad (55)$$

Eq.s (54) and (55) must be established together. Therefore if $\mu_{ij} = 0$, $m(m-1)$ equations should be satisfied for the performed process, which in fact they specify the performed process as well as system compatibility conditions.

By using Eq. (19), the dynamic energy rate can also be expressed as:

$$\dot{U}_D = (1 - \alpha)\dot{U}_T - \beta\ddot{U}_T \quad (56)$$

That takes the rate of dynamic energy.

10. Energy State Equation

Using Eq. (4), the variation of the dynamic energy in a process can be written as follows:

In the case of $\beta = 0$, then dynamic and non-dynamic energy changes are independent of the exchange rate of energy with the environment and will only depend on the amount of energy exchanged. In this case, it is expected that for each value of the energy given to the system, the dynamic and non-dynamic energies will establish in a given relationship, which is dependent on the internal structure of the system.

If we consider this relation as follows:

$$G(U_{ND}, U_D) = 0 \quad (57)$$

In this case, by calculating the variation of Eq. (57) and using Eq.s (18) and (56), the following differential equation is obtained:

$$\alpha \frac{\partial G}{\partial U_{ND}} + (1 - \alpha) \frac{\partial G}{\partial U_D} = 0 \quad (58)$$

If $\alpha = 0$ or $\alpha = 1$, we obtain from the differential equation (58) that $G = c$, where c is a constant value. The value of $\alpha = 0$ represents the process by which all energy exchanged with the environment is converted to dynamic energy and in the case of $\alpha = 1$, all energy exchanged also increases non-dynamic energy and does not result in a change in the dynamic energy. If $\alpha = 1/2$, then from the differential Eq. (58), $U_{ND} - U_D = c$ is obtained, where c is a constant value.

In fact for a physical system, if $\beta = 0$ then every function G in the form of Eq. (58) represents a feasible process in the system.

11. A Few Energy-Related Basic Examples

In this part, the presented model, novel concepts, and established relations are developed for some energy-related basis examples. The main purpose is an applicable validation for the established concepts as well as relations. In the following examples, based on the established model, the distribution of the whole energy given to the system is shown. In some of them, a part of energy may be wasted and the remaining may be stored in the components of the system. No contradiction will be found in the relations. These basis problems can be combined with others to create a variety of systems, ranging from classical to modern domains, and are used to show the performance ability of the established energy structure approach. Also, the established model is used to investigating the linear viscoelasticity

models.

11.1 First Basic Example: Newton's Particle System

For Newton's particle shown in figure 9 with $F_{i,ext}$ as external force, and $F_{i,int}$ as internal force applied on the particle i :

$$\alpha = \beta = 0 \quad (59)$$

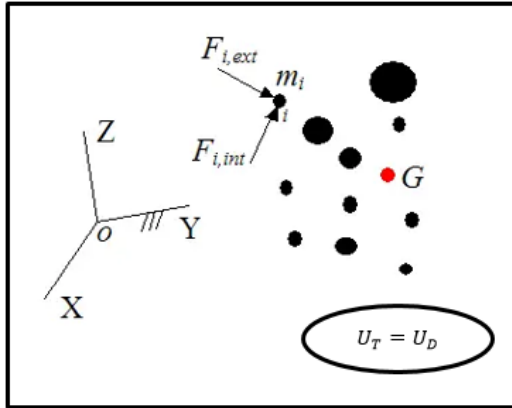


Figure 9. Dynamic and non-dynamic energy of Newton's particle system.

In this case, we obtain of the Eq. (60):

$$\dot{U}_D = \dot{U}_T \quad (60)$$

This equation states that the energy given to the system is completely transformed into dynamic energy.

In this case, the relation (28) is established in the equality state and the function G is also $G = 0$.

11.2 Second Basic Example: Elasticity Properties

An elastic rod with hardness k under the axial force p at the end is supposed, as shown in figure 10.

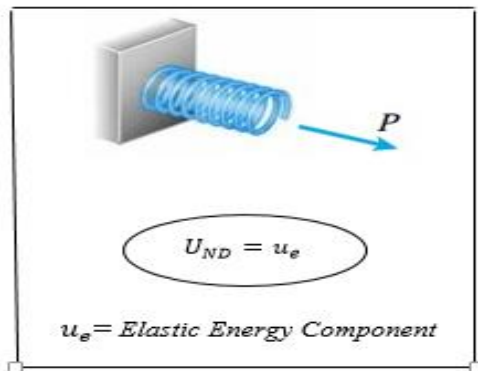


Figure 10. Non- dynamic energy related to the elasticity properties.

The elastic potential energy of the spring is considered as an independent component of the process:

$$U_{ND} = u_e \quad (61)$$

That u_e is the elastic potential energy. Therefore, the corresponding coefficient in Eq. (15) can be considered as follows:

$$\alpha_e = \frac{\sqrt{2ku_e}}{p} \quad (62)$$

From the Eq. (62), it can be concluded that the coefficient is a function of the current system condition and also the amount of energy applied to it.

Given that $\gamma_e = (\frac{1-\alpha_e}{\alpha_e})$ and $\gamma_e' = 0$, Eq. (63) also obtains the dynamic energy as follows:

$$\delta U_D = (\frac{1-\alpha_e}{\alpha_e}) \delta u_e \quad (63)$$

Therefore:

$$\delta U_D = \left(\frac{1 - \left(\frac{\sqrt{2ku_e}}{p} \right)}{\left(\frac{\sqrt{2ku_e}}{p} \right)} \right) \delta u_e \equiv (p - kv) \delta u_e \quad (64)$$

Where v is the displacement of the force location p . Using this equation, we will be able to calculate the dynamic energy available in the system. This energy belongs to all elements of the system and based on Eq. (64) is a function of the elastic potential energy of the system, $U_D = U_D(u_e)$.

As can be seen, Eq. (64) is completely equivalent to the result that expected, which determines the total entire system's dynamic energy.

Given that an independent energy component participates in the process, there is no need to apply a specific compatibility condition to the changes in the independent energy components ($\frac{m(m-1)}{2} = 0$ for $m = 1$).

The Eq. (42) indicates that the dynamic energy does not depend on the rate of change of the component u_e and therefore dissipation does not occur in the system due to non-zero energy applied rate and the more energy distribution is not occurred, in the other words, given that for this problem ($\sum_{p=1}^n \frac{\partial h_p}{\partial \dot{u}_j} = 0$), the relation (28) will be in the state of equality.

The differential equation for the function G is obtained as follows:

$$\left(\frac{\sqrt{2kU_{TV}}}{p} \right) \frac{\partial G}{\partial U_{ND}} + \left(1 - \frac{\sqrt{2kU_{TV}}}{p} \right) \frac{\partial G}{\partial U_D} = 0 \quad (65)$$

In fact, the above equation shows the energy states for the problem of figure 10.

11.3 Third Basic Example: System with Mass and Elastic Bounding

This example represents a sub-system of two point masses with elastic bonding so that the point masses can be moved along the line of their connection, as shown in figure 11:

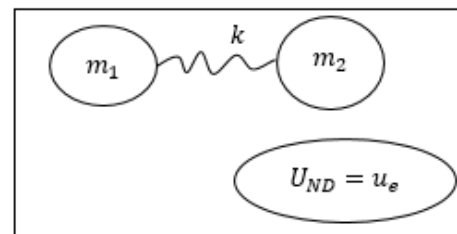


Figure 11. Non-dynamic energy for a system with mass and elastic bounding.

If the gravitational potential energy is ignored, and also considering u_e as elastic energy component, the non-dynamic energy for this system can be expressed as follows:

$$U_{ND} = u_e \quad (66)$$

Given that $\sum_{p=1}^n \frac{\partial h_p}{\partial \dot{u}_j} = 0$, the relation (28) is established for this problem in its equality state.

11.4 Fourth Basic Example: System with Electric Charges and Elastic Bonding

The figure 12 is shown a system including two point electric charges with elastic bonding so that the point electric charge can be moved along the line of their connection:

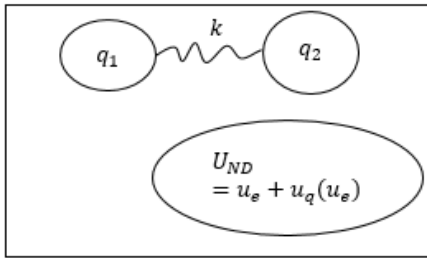


Figure 12. Non-dynamic energy for a system with electric charges and elastic bonding.

Considering u_e as elastic energy component, and u_q as electrical energy component, the following equation can be expressed for non-dynamic energy of this system:

$$U_{ND} = u_e + \frac{c_1}{c_2\sqrt{u_e+c_3}} \quad (67)$$

Where c_1 , c_2 and c_3 are constants depend on the structure of the system and the initial and final conditions of the process. Eq. (67) can explain the processes that electric charges move along the lines of each other.

Given $\sum_{p=1}^n \frac{\partial h_p}{\partial \dot{u}_j} = 0$, relation (28) is established for this problem in its equality state.

11.5 Fifth Basic Example: Combining Third and Fourth Examples

Figure 13 illustrates two examples by combining the third and fourth examples. These examples are samples of multi-component systems. For models shown in figure 13, the components of energy that are important are: the potential energy of springs and electrical charge, and also the compatibility conditions will be important for the investigation of these systems.

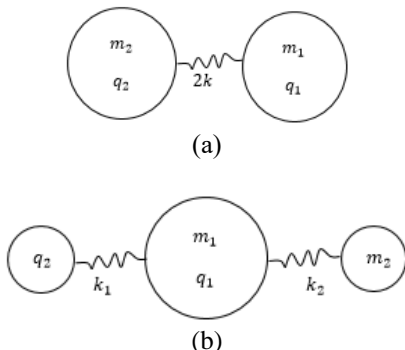


Figure 13. Two different schemes of combining two points electric charge with elastic bonding.

For figure (13-a) with considering $u_e' = 2u_e$, non-dynamic energy equation can be written:

$$U_{ND} = u_e' + \frac{c_1}{c_2\sqrt{u_e'+c_3}} \quad (68)$$

And for figure (13-b) it can be written:

$$U_{ND} = u_{e1} + u_{e2} + \frac{c_1}{c_2\sqrt{u_{e1}+c_3}} \quad (69)$$

That u_{e1} and u_{e2} are the elastic potential energy of k_1 and k_2 . Respectively based on Eq. (30) dynamic energy is:

$$\delta U_D = \gamma_j \delta u_{ej} + \gamma_j' \delta \dot{u}_{ej}, \quad j = 1 \text{ or } 2 \quad (70)$$

And compatibility condition for this system is:

$$\gamma_1 \delta u_{e1} + \gamma_1' \delta \dot{u}_{e1} = \gamma_2 \delta u_{e2} + \gamma_2' \delta \dot{u}_{e2} \quad (71)$$

Because for this problem β_1 and β_2 are zero, therefore γ_1' and γ_2' are zero too, so Eq.s (70) and (71) can be rewritten as follows:

$$\gamma_1 \delta u_{e1} = \gamma_2 \delta u_{e2} \quad (72)$$

$$\delta U_D = \gamma_j \delta u_{ej}, \quad j = 1 \text{ or } 2 \quad (73)$$

And by using Eq. (51):

$$\left(\frac{1-\alpha}{\alpha_{e1}}\right) \delta u_{e1} = \left(\frac{1-\alpha}{\alpha_{e2}}\right) \delta u_{e2} \quad (74)$$

$$\delta U_D = \left(\frac{1-\alpha}{\alpha_{ej}}\right) \delta u_{ej}, \quad j = 1 \text{ or } 2 \quad (75)$$

Also by using the Eq.s (16) and (17):

$$\alpha = \alpha_{e1} + \alpha_{e2} \left(1 - \frac{c_1 c_2}{(2\sqrt{u_{e1}})(c_2\sqrt{u_{e1}+c_3})^2}\right) \quad (76)$$

$$\beta = 0 \quad (77)$$

Therefore Eq.s (74) and (75) can be rewritten as follow:

$$\left(\frac{\delta u_{e1}}{\alpha_{e1}}\right) = \left(\frac{\delta u_{e2}}{\alpha_{e2}}\right) \quad (78)$$

$$\delta U_D = \left(\frac{1 - (\alpha_{e1} + \alpha_{e2} \left(1 - \frac{c_1 c_2}{(2\sqrt{u_{e1}})(c_2\sqrt{u_{e1}+c_3})^2}\right))}{\alpha_{ej}}\right) \delta u_{ej}, \quad j = 1 \text{ or } 2 \quad (79)$$

Given the Eq. (15), the Eq. (79) has the same result as we expected. The Eq. (58) gives the dynamic energy of the system in all possible processes. By using Eq. (76), Eq. (79) can be rewritten as following too:

$$\delta U_D = D \delta U_T \quad (80)$$

Where:

$$D = \left(1 - \left(\alpha_{e1} + \alpha_{e2} \left(1 - \frac{c_1 c_2}{(2\sqrt{u_{e1}})(c_2\sqrt{u_{e1}+c_3})^2}\right)\right)\right) \quad (81)$$

The coefficient D indicates how much of the input energy into the system will be converted to dynamic energy. This coefficient can provide a description of the internal structure of the system, its inertia as well as the processes that can be performed. Also, according to Eq. (47), energy conservation principle, the rest of the energy will be converted to non-dynamic energy of the system, therefore:

$$\delta U_{ND} = \delta U_T - \delta U_D \quad (82)$$

$$\delta U_{ND} = (1 - D)\delta U_T \equiv D^*\delta U_T \quad (83)$$

The coefficient D^* denotes the share of non-dynamic energies. This coefficient can provide a description of the possibility of distributing non-dynamic energies in the system. If the variation of the Eq. (69) is calculated, the result will be the Eq. (82).

11.6 Sixth Basic Example: Generalized Maxwell and Kelvin's Viscoelasticity Models

From the point of view of energy behavior, viscoelastic materials have components of stored energy and wasted energy. The way of activation and dependence of the relevant components depends on the relevant viscoelasticity model, and also the amount and manner of energy applying is included in determining the loading coefficients of the components. Therefore, the investigation of viscoelastic materials and their energy behavior in the perspective of energy structure can provide important results about them, and also be a suitable topic to express the applications of the perspective of energy structure. So, In this section, the presented approach is used to linear viscoelasticity problems. For example, generalized Kelvin and Maxwell's models are studied. Eq. (84) shows the general linear form of U_{ND} with two components: one independent component and one dependent component.

$$U_{ND} = u_1 + (c_1\dot{u}_1 + c_2) \quad (84)$$

Eq. (84) can be used for investigating the linear viscoelasticity models. Since, if the component of stored energy is shown by u_e and the component of dissipated energy shown by u_d , for the kelvin model [35], as shown in figure 14:

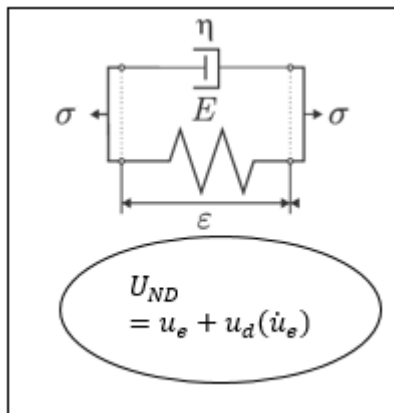


Figure 14. Energy structure equation for viscoelasticity kelvin model.

$$\frac{du_e}{dx} = Ex \quad (85)$$

$$\frac{du_d}{dx} = \eta\dot{x} \quad (86)$$

Therefore:

$$\frac{d^2u_e}{dxdt} = \left(\frac{E}{\eta}\right)\frac{du_d}{dx} \quad (87)$$

$$u_d = \left(\frac{E}{\eta}\right)u_e + constant \quad (88)$$

And also for the Maxwell model [35], as shown in figure 15:

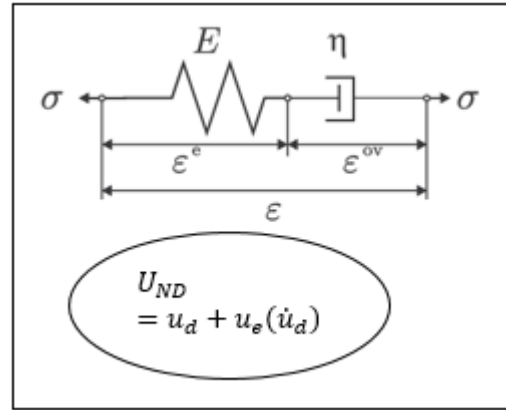


Figure 15. Energy structure equation for viscoelasticity Maxwell model.

$$\dot{\epsilon}^{OV} = \frac{E}{\eta}\epsilon^e \quad (89)$$

Therefore:

$$\frac{du_d}{d\epsilon^{OV}} = \eta\dot{\epsilon}^{OV} = E\epsilon^e = \frac{du_e}{d\epsilon^e} \quad (90)$$

$$\frac{du_d}{\dot{\epsilon}^{OV}dt} = \frac{du_e}{\dot{\epsilon}^e dt} \quad (91)$$

$$u_e = \frac{\eta}{2E}\dot{u}_d \quad (92)$$

In fact, if the independent component is assumed the component of stored energy, that means $u_1 = u_e$ and $c_1 = \frac{E}{\eta}$, equation (84) can be used for kelvin model and if the independent component is assumed the component of dissipated energy, that means $u_1 = u_d$ and $c_1 = \frac{\eta}{2E}$, Eq. (84) can be used to Maxwell model. And also c_1 is determined with Eq.s (88) and (92).

And also by using of Eq.s (16) and (17), for example, for the kelvin model:

$$\alpha = \alpha_e + c_1\dot{\alpha}_e \quad (93)$$

$$\beta = c_1\alpha_e \quad (94)$$

And about determining the α_e , it can be written based on the energy conservation principle:

$$\delta U_T = \delta u_e + \delta u_d \quad (95)$$

And also:

$$\delta u_d = \left(\frac{E}{\eta}\right)\delta\dot{u}_e \quad (96)$$

$$\delta u_d = \left(\frac{\eta}{E}\right) [\dot{\alpha}_e \delta U_T + \alpha_e \delta \dot{U}_T] \quad (97)$$

Therefore:

$$\delta U_T = (\alpha_e) \delta U_T + \left(\frac{E}{\eta}\right) [\dot{\alpha}_e \delta U_T + \alpha_e \delta \dot{U}_T] \quad (98)$$

Or:

$$\dot{U}_T = (\alpha_e) \dot{U}_T + \left(\frac{E}{\eta}\right) [\dot{\alpha}_e \dot{U}_T + \alpha_e \ddot{U}_T] \quad (99)$$

$$\dot{\alpha}_e + \left[\frac{\dot{U}_T + \left(\frac{E}{\eta}\right) \ddot{U}_T}{\left(\frac{E}{\eta}\right) \dot{U}_T} \right] \alpha_e = \left(\frac{\eta}{E}\right) \quad (100)$$

Therefore, α_e is calculated from Eq. (100) in functional of the how energy is applied to the system.

The obtained energy structure can be easily generalized for different combinations of the corresponding elements. For example, figure 16 can be considered:

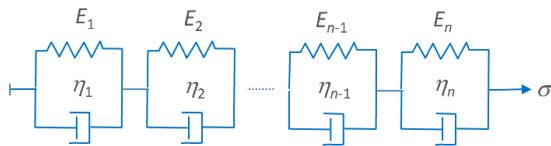


Figure 16. Energy structure equation for generalized Kelvin elements.

$$U_V = u_{e1} + u_{e2} + \dots + u_{eN} + c_{e1} \dot{u}_{e1} + c_{e2} \dot{u}_{e2} + \dots + c_{eN} \dot{u}_{eN} + \text{constant} \quad (101)$$

Derived structure of Eq. (101) also can be used for generalized Maxwell elements:

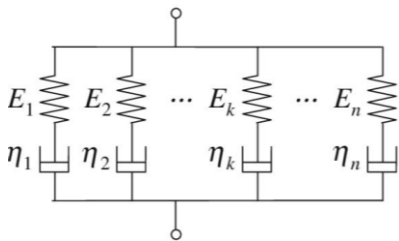


Figure 17. Energy structure equation for generalized Maxwell element.

$$U_V = u_{d1} + u_{d2} + \dots + u_{dN} + c_{d1} \dot{u}_{d1} + c_{d2} \dot{u}_{d2} + \dots + c_{dN} \dot{u}_{dN} + \text{constant} \quad (102)$$

In addition to obtain the structure of non-inertial energies, it actually obtains the feasible processes and the way energy components change as a result of energy exchange between the system and the surrounding environment.

12. Irreversibility Analysis

Analysis of irreversibility in the perspective of energy structure has been done using a novel definition in references [58-59,71]. In this section, a brief overview is provided. Considering figures 18 and 19.

Considering Eq.s (103-104):

$$\delta H_i = \left(\sum_{p=1}^n \left(\frac{\partial h_p}{\partial u_i} \right) \right) \delta \dot{U}_i \quad (103)$$

$$\delta \Psi = \sum_{i=1}^m \delta H_i \quad (104)$$

So, irreversibility is derived as follows:

$$\varphi = \frac{\delta \Psi}{\delta U_T} = \sum_{i=1}^m \frac{\delta H_i}{\delta U_T} = \sum_{i=1}^m \varphi_i \quad (105)$$

That always has positive sign (as well as $\varphi_i \geq 0$) [58-59,71].

Eq. (105) gives irreversibility from the point of view of the energy structure. Also, another important feature of this equation is obtaining irreversible components that determine the amount and manner of the effect of each component in the total irreversibility. Therefore, irreversibilities are clearly dependent on the internal structure of the system, the amount and manner of energy exchange between the system and the surrounding, which are presented in Eq. (105).

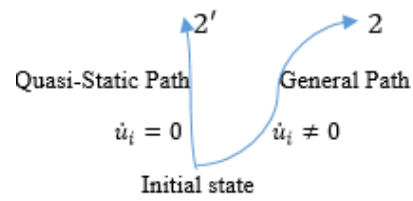


Figure 18. Different paths for the performed process [71].

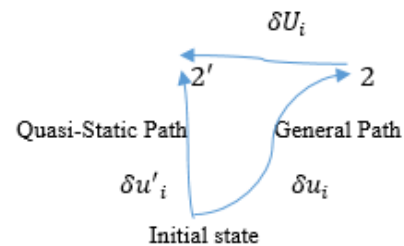


Figure 19. Deviation from the quasi-static path to the general [71].

13. Conclusions

The perspective of energy structure suggests the use of activated energy components and their structure to represent energy in physical systems. In fact, due to the role of the energy conservation principle as a unifying principle in physics, energy components are able to expand the range of responses and processes that can be performed by physical systems. Valuable achievements have also been presented in this direction, which have been gathered in this paper, as well as the perspective of the energy structure has been developed and the relevant equations for the development of a closed space of a scientific theory have been established and generalized in order to explain and analyze the physical processes of physical systems. The effort has been to find the simplest form of equations in order to close the solution spaces. In fact, given the energy components of the system as quantities that can describe the process performed, new space is created for the set of governing equations. In the resulting space, the effects of the second law of thermodynamics can be directly applied to the energy structure of the system and in fact, the sensitivity of the system to the second law can be examined. Also, one of the advantages of this new approach is that a particular process in various conditions is studied instead of studying a particle of the system. In fact, this approach gives a general view regarding the studied process as well as the internal structure of the system in response to the energy exchange with the

environment. This paper established an energy components-based-general model inspired by the first and second laws of thermodynamics as well as using a new division to the total energy of the system. The established model is completed by extracting the physical direction for the feasible physical processes based on the energy components of the system. Also, the presented model has developed for the high particle number systems as well as some energy-related basis examples. As three cases of the other achievements of the energy structure approach is the providing a quasi-statistical equation to entropy, a general solution to the different formulations of the second law of thermodynamics as well as irreversibility analysis using a novel definition. The problems studied are the energy-related basis systems that can be combined with others to create a variety of systems. Eq. (52) can also derive dynamic energy in terms of independent energy components. These relations can also describe the dynamics of the system with respect to independent component changes. The energy coordinates of the system by relying on the energy conservation principle obtain a standard and error-free mathematical method for the first and second laws in such a way that unification and a wide range of applications are provided, and applicability in classical and modern problems is created.

Acknowledgements:

We sincerely thank Dr. Mehran Moradi, from the Department of Mechanical Engineering of Isfahan University of Technology, for the wonderful scientific support that he has had in the direction of presenting and developing Energy Structure Theory. Also, I express my best gratitude to Mrs. Zahra Amini, from Andishmand-Lahijan non-profit institution, for her countless support in order to complete and present this article. Finally, we are grateful to Dr. Mahmoud Hemami, Dr. Mahdi Salmlani Tehrani and Prof. Mohammad Reza Forouzan, from the Department of Mechanical Engineering of Isfahan University of Technology, as well as Mr. Pooya Torkman, from the School of Metallurgy and Materials Engineering of Iran University of Science and Technology, for their various support.

Nomenclature

g_j : Value-dependent energy component with SI (metric) dimension (*Joule*).

h_n : Rate-dependent energy component with SI (metric) dimension (*Joule*).

K_{MS} : Universal constant of quasi-statistical entropy definition without SI (metric) dimension.

u_i : Energy component (Dependent and Independent) of the system with SI (metric) dimension (*Joule*).

U_T : Total energy of the system with SI (metric) dimension (*Joule*).

U_{ND} : Non-Dynamic energy component of the system with SI (metric) dimension (*Joule*).

U_D : Dynamic energy component of the system with SI (metric) dimension (*Joule*).

s : Entropy of the system with SI (metric) dimension ($\frac{Joule}{K}$).

Greek Letters

ϕ : Irreversibility component with SI (metric) dimension (*Joule*).

α : Change energy coefficient without SI (metric) dimension.

β : Change energy-rate coefficient without SI (metric) dimension.

γ : Change energy component coefficient without SI (metric) dimension.

Ψ : Irreversibility with SI (metric) dimension (*Joule*).

ϵ : Strain without SI (metric) dimension.

σ : Stress with SI (metric) dimension ($\frac{N}{m^2}$).

η : Viscosity coefficient with SI (metric) dimension ($\frac{m^2}{s}$).

References:

- [1] A. Bejan, *Advanced engineering thermodynamics*, New Jersey: John Wiley & Sons, 2016.
- [2] P. G. Tait, *Sketch of thermodynamics*, Edinburgh: D. Douglas, 1877.
- [3] R. Clausius, "The second law of thermodynamics", *The World of Physics*, 1, 1865.
- [4] J. M. Heath, XXVI. "On the principles of thermodynamics", *The London, Edinburgh, and Dublin Philosophical Magazine and Journal of Science*, Vol. 40, no. 266, pp. 218-220, 1870, doi.org/10.1080/14786447008640386.
- [5] C. Maes, and H. Tasaki, "Second law of thermodynamics for macroscopic mechanics coupled to thermodynamic degrees of freedom", *Letters in Mathematical Physics*, Vol. 79, pp. 251-261, 2007, doi.org/10.1007/s11005-006-0136-9.
- [6] S. F. Wu, Wang, B. Yang, G.H. and P. M. Zhang, "The generalized second law of thermodynamics in generalized gravity theories", *Classical and Quantum Gravity*, Vol. 25, no. 23, p.235018, 2008, doi.org/10.1088/0264-9381/25/23/235018.
- [7] J. Xuereb, S. Campbell, J. Goold, and A. Xuereb, "DQC1 as an Open Quantum System", arXiv preprint arXiv:2209.03947, 2022, doi.org/10.48550/arXiv.2209.03947.
- [8] B. C. Eu, "Kinetic theory and irreversible thermodynamics", *Accounts of Chemical Research*, Vol. 19, no. 5, pp. 153-160, 1986, doi.org/10.1021/ar00125a005.
- [9] E. H. Lieb, and J. Yngvason, "The physics and mathematics of the second law of thermodynamics", *Physics Reports*, Vol. 310, no. 1, pp. 1-96, 1999, doi.org/10.1016/S0370-1573(98)00082-9.
- [10] R. C. Nichols, XLIV. "On the proof of the second law of thermodynamics", *The London, Edinburgh, and Dublin Philosophical Magazine and Journal of Science*, Vol. 1, no. 5, pp. 369-373, 1876, doi.org/10.1080/14786447608639054.
- [11] L. D. Rio, J. Åberg, R. Renner, O. Dahlsten, and V. Vedral, "The thermodynamic meaning of negative entropy", *Nature*, Vol. 474, no. 7349, pp. 61-63, 2011.
- [12] L. A. Sosnovskiy, and S. S. Sherbakov, "Mechanothermodynamic entropy and analysis of damage state of complex systems", *Entropy*, Vol. 18, no. 7, p.268, 2016, doi.org/10.3390/e18070268.
- [13] L. A. Sosnovskiy, and S. S. Sherbakov, "A model of mechanothermodynamic entropy in tribology", *Entropy*, Vol. 19, no. 3, p.115, 2017, doi.org/10.3390/e19030115.

- [14] P. V. Coveney, "The second law of thermodynamics: entropy, irreversibility and dynamics", *Nature*, Vol. 333, no. 6172, pp. 409-415, 1988, doi.org/10.1038/333409a0.
- [15] W. J. Macquorn Rankine, C. E. LL. D. F. SS. L, "On the second law of thermodynamics", *The London, Edinburgh, and Dublin Philosophical Magazine and journal of science*, Vol. 30, no. 203, 1965.
- [16] C. M. Dafermos, "The second law of thermodynamics and stability", *Archive for Rational Mechanics and Analysis*, Vol. 70, no. 2, pp. 167-179, 1979.
- [17] C. Basaran, and C. Y. Yan, "A thermodynamic framework for damage mechanics of solder joints" *J. Electron. Packaging*, 120, 4, 1998, doi.org/10.1115/1.2792650.
- [18] C. S. Desai, C. Basaran, T. Dishongh, and J. L. Prince, "Thermomechanical analysis in electronic packaging with unified constitutive model for materials and joints", *IEEE Transactions on Components, Packaging, and Manufacturing Technology: Part B*, Vol. 21, no. 1, pp. 87-97, 1998, doi.org/10.1109/96.659511.
- [19] L. A. Sosnovskiy, and S. S. Sherbakov, "On the development of mechanothermodynamics as a new branch of physics", *Entropy*, Vol. 21, no. 12, p. 1188, 2019, doi.org/10.3390/e21121188.
- [20] R. Bendikiene, A. Bahdanovich, R. Cesnavicius, A. Ciuplys, V. Grigas, A. Jutas, D. Marmysh, A. Nasan, L. Shemet, S. Sherbakov, and L. Sosnovskiy, "Tribofatigue behavior of austempered ductile iron MoNiCa as new structural material for rail-wheel system", *Materials Science*, Vol. 26, no. 4, pp. 432-437, 2020, doi.org/10.5755/j01.ms.26.4.25384.
- [21] T. Hiemstra, "Formation, stability, and solubility of metal oxide nanoparticles: Surface entropy, enthalpy, and free energy of ferrihydrite", *Geochimica et Cosmochimica Acta*, 158, pp. 179-198, 2015, doi.org/10.1016/j.gca.2015.02.032.
- [22] M. Sheikholeslami, M. Jafaryar, E. Abohamzeh, A. Shafee, and H. Babazadeh, "Energy and entropy evaluation and two-phase simulation of nanoparticles within a solar unit with impose of new turbulator", *Sustainable Energy Technologies and Assessments*, 39, p.100727, 2020, doi.org/10.1016/j.seta.2020.100727.
- [23] M. Sheikholeslami, M. Jafaryar, E. Abohamzeh, A. Shafee, Z. Li, and R. U. Haq, "Heat transfer of nanoparticles employing innovative turbulator considering entropy generation", *International Journal of Heat and Mass Transfer*, 136, pp. 1233-1240, 2019, doi.org/10.1016/j.ijheatmasstransfer.2019.03.091.
- [24] M. W. Glasscott, A. D. Pendergast, S. Goines, A. R. Bishop, A. T. Hoang, C. Renault, and J. E. Dick, "Electrosynthesis of high-entropy metallic glass nanoparticles for designer, multi-functional electrocatalysis", *Nature Communications*, Vol. 10, no. 1, p.2650, 2019, doi.org/10.1038/s41467-019-10303-z.
- [25] C. Zhang, Z. Peng, C. Huang, B. Zhang, C. Xing, H. Chen, H. Cheng, J. Wang, and S. Tang, "High-energy all-in-one stretchable micro-supercapacitor arrays based on 3D laser-induced graphene foams decorated with mesoporous ZnP nanosheets for self-powered stretchable systems", *Nano Energy*, 81, p.105609, 2021, doi.org/10.1016/j.nanoen.2020.105609.
- [26] J. F. Klein, *Physical significance of entropy or of the second law*, New York: D. Van Nostrand Company, 1910, doi.org/10.5962/bhl.title.19423.
- [27] E. G. D. Cohen, "Boltzmann and Einstein: Statistics and dynamics—An unsolved problem", *Pramana*, 64, pp. 635-643, 2005, doi.org/10.1007/BF02704573.
- [28] W. Thomson, "The kinetic theory of the dissipation of energy", *Proceedings of the Royal Society of Edinburgh*, 8, pp. 325-334, 1875, 9. doi.org/10.1017/S0370164600029680.
- [29] S. H. Burbury, "A theorem on the dissipation of energy", *The London, Edinburgh, and Dublin Philosophical Magazine and Journal of Science*, Vol. 13, no. 83, pp. 417-419, 1882, LII. doi.org/10.1080/14786448208627206.
- [30] R. Lord, "On the dissipation of energy", *Van Nostrand's Eclectic Engineering Magazine*, Vol. 12, no. 78, pp. 1869-1879.
- [31] W. Thomson, "On a Universal Tendency in Nature to the Dissipation of Mechanical Energy", *Proceedings of the Royal Society of Edinburgh*, 3, pp.139-142, 1857, 2. doi.org/10.1017/S0370164600027541.
- [32] H. Lee, N. Campbell, J. Lee, T. J. Asel, T. R. Paudel, H. Zhou, J. W. Lee, B. Noesges, J. Seo, B. Park, and L. J. Brillson, "Direct observation of a two-dimensional hole gas at oxide interfaces", *Nature materials*, Vol. 17, no. 3, pp. 231-236, 2018, doi.org/10.1038/s41563-017-0002-4.
- [33] M. Akbarifar, M. Divandari, S. M. A. Boutorabi, S. H. Ha, Y. O. Yoon, and S. K. Kim, "Short-time oxidation of Al-Mg in dynamic conditions", *Oxidation of Metals*, 94, pp. 409-429, 2020, doi.org/10.1007/s11085-020-09999-y.
- [34] A. Dehghani, and S. M. A. Boutorabi, "Thickness estimation (folds and wrinkles) on short time dynamically formed double oxide film in Al-7Si-Mg alloyed with beryllium", *Materials Research Express*, Vol. 6, no. 10, p.106574, 2019, doi.org/10.1088/2053-1591/ab35ed.
- [35] J. Campbell, "The consolidation of metals: The origin of bifilms", *Journal of materials science*, 51, pp. 96-106, 2016, doi.org/10.1007/s10853-015-9399-9.
- [36] G. Gyarmati, G. Fegyverneki, T. Mende, and M. Tokár, "Characterization of the double oxide film content of liquid aluminum alloys by computed tomography", *Materials Characterization*, 157, p.109925, 2019, doi.org/10.1016/j.matchar.2019.109925.
- [37] H. Lee, N. Campbell, J. Lee, T. J. Asel, T. R. Paudel, H. Zhou, J. W. Lee, B. Noesges, J. Seo, B. Park, and L. J. Brillson, "Direct observation of a two-dimensional hole gas at oxide interfaces", *Nature materials*, Vol. 17, no. 3, pp. 231-236, 2018, doi.org/10.1038/s41563-017-0002-4.
- [38] A. Dehghani, and S. M. A. Boutorabi, "Nano Double Oxide Film (NDOF) Characteristics of A356 Alloy Casting Protected With Beryllium in Turbulence Conditions", *Founding Research Journal*, Vol. 2, no. 2,

pp. 71-78, 2018.

- [39] S. M. A. Boutorabi, P. Torkaman, J. Campbell, and A. Zolfaghari, "Structure and properties of carbon steel cast by the ablation process", *International Journal of Metalcasting*, 15, pp. 306-318, 2021, doi.org/10.1007/s40962-020-00466-7.
- [40] A. H. Fazeli, H. Saghafian, S. M. A. Boutorabi, and J. Campbell, "The fluidity of aluminium ductile irons", *International Journal of Metalcasting*, pp. 1-10, 2021, doi.org/10.1007/s40962-021-00581-z.
- [41] Y. Mishin, "Thermodynamic theory of equilibrium fluctuations", *Annals of Physics*, 363, pp. 48-97, 2015, doi.org/10.1016/j.aop.2015.09.015.
- [42] A. Bravetti, C. S. Lopez-Monsalvo, and F. Nettel, "Contact symmetries and Hamiltonian thermodynamics", *Annals of Physics*, 361, pp. 377-400, 2015, doi.org/10.1016/j.aop.2015.07.010.
- [43] R. Dann, and R. Kosloff, "Quantum signatures in the quantum Carnot cycle", *New Journal of Physics*, Vol. 22, no. 1, p.013055, 2020, doi.org/10.1088/1367-2630/ab6876.
- [44] G. Bulnes Cuetara, A. Engels, and M. Esposito, "Stochastic thermodynamics of rapidly driven quantum systems", *New Journal of Physics*, 17, p.055002, 2015, doi.org/10.1088/1367-2630/17/5/055002.
- [45] R. Gallego, J. Eisert, and H. Wilming, "Thermodynamic work from operational principles", *New Journal of Physics*, Vol. 18, no. 10, p. 103017, 2016, doi.org/10.1088/1367-2630/18/10/103017.
- [46] G. Gour, M. P. Müller, V. Narasimhachar, R. W. Spekkens, and N. Y. Halpern, "The resource theory of informational nonequilibrium in thermodynamics", *Physics Reports*, 583, pp. 1-58, 2015, doi.org/10.1016/j.physrep.2015.04.003.
- [47] A. Puglisi, A. Sarracino, and A. Vulpiani, "Temperature in and out of equilibrium: A review of concepts, tools and attempts", *Physics Reports*, 709, pp. 1-60, 2017, doi.org/10.1016/j.physrep.2017.09.001.
- [48] Z. Said, L. S. Sundar, A. K. Tiwari, H. M. Ali, M. Sheikholeslami, E. Bellos, and H. Babar, "Recent advances on the fundamental physical phenomena behind stability, dynamic motion, thermophysical properties, heat transport, applications, and challenges of nanofluids", *Physics Reports*, 946, pp. 1-94, 2022, doi.org/10.1016/j.physrep.2021.07.002.
- [49] M. N. Bera, A. Riera, M. Lewenstein, and A. Winter, "Generalized laws of thermodynamics in the presence of correlations", *Nature communications*, Vol. 8, no. 1, p.2180, 2017, doi.org/10.1038/s41467-017-02370-x.
- [50] S. Shahsavari, "Possibility unique combination for first and second law of thermodynamics", *Quantum Journal of Engineering, Science and Technology*, Vol. 2, no. 5, pp. 51-52, 2021,.
- [51] L. Qiu, N. Zhu, Y. Feng, E. E. Michaelides, G. Żyła, D. Jing, X. Zhang, P. M. Norris, C.N. Markides, and O. Mahian, "A review of recent advances in thermophysical properties at the nanoscale: From solid state to colloids", *Physics Reports*, 843, pp. 1-81, 2020, doi.org/10.1016/j.physrep.2019.12.001.
- [52] Á. Rivas, "Strong coupling thermodynamics of open quantum systems", *Physical review letters*, Vol. 124, no. 16, p.160601, 2020, doi.org/10.1103/PhysRevLett.124.160601.
- [53] I. Peshkov, M. Pavelka, E. Romenski, and M. Grmela, "Continuum mechanics and thermodynamics in the Hamilton and the Godunov-type formulations", *Continuum Mechanics and Thermodynamics*, 30, pp.1343-1378, 2018, doi.org/10.1007/s00161-018-0621-2.
- [54] K. Ptaszyński, and M. Esposito, "Thermodynamics of quantum information flows", *Physical review letters*, Vol. 122, no. 15, p.150603, 2019, doi.org/10.1103/PhysRevLett.122.150603.
- [55] L. Masanes, and J. Oppenheim, "A general derivation and quantification of the third law of thermodynamics", *Nature communications*, Vol. 8, no. 1, pp. 1-7, 2017, doi.org/10.1038/ncomms14538.
- [56] S. Shahsavari, and M. Moradi, "A General Solution to the Different Formulations of the Second Law of Thermodynamics", *Journal of Advanced Research in Fluid Mechanics and Thermal Sciences*, Vol. 82, no. 2, pp. 61-71, 2021, doi.org/10.37934/arfmts.82.2.6171.
- [57] S. Shahsavari, M. Moradi, and P. Torkaman, "A Quasi-Statistical Approach to the Boltzmann Entropy Equation Based on a Novel Energy Conservation Principle", *Journal of Advanced Research in Fluid Mechanics and Thermal Sciences*, Vol. 101, no. 2, pp. 99-110, 2023, doi.org/10.37934/arfmts.101.2.99110.
- [58] S. Shahsavari, and M. Moradi, "A New Approach to the Energy Conservation Principle and Physical Systems", Ph.D. dissertation, Department of Mechanical Engineering, Isfahan University of Technology, IR, 2022.
- [59] S. Shahsavari, and M. Moradi, "A Study of the Entropy Production in Physical Processes from a New Perspective of the Energy Structure", *Asian Journal of Applied Sciences* (ISSN: 2321-0893), 8, 2020, doi.org/10.24203/ajas.v8i6.6472.
- [60] H. J. Borchers, "Some remarks on the second law of thermodynamics", *Reports on mathematical physics*, Vol. 22, no. 1, pp. 29-48, 1985, doi.org/10.1016/0034-4877(85)90004-7.
- [61] B. C. Eu, "Kinetic theory and irreversible thermodynamics", *Accounts of Chemical Research*, Vol. 19, no. 5, pp. 153-160, 1986, doi.org/10.1021/ar00125a005.
- [62] R. D. Gregory, *Classical mechanics*, Cambridge University Press, 2006.
- [63] É. Roldán, *Irreversibility and dissipation in microscopic systems*, Springer, 2014, doi.org/10.1007/978-3-319-07079-7.
- [64] D. R. Bland, *The theory of linear viscoelasticity*, New York: Courier Dover Publications, 2016.
- [65] S. Shahsavari, and P. Torkaman, "Energy Conservation Principle from the Perspective of the Energy Structure Theory", *Asian Journal of Applied Sciences* (ISSN:

- 2321–0893) Vol. 10, no. 5, 2022, doi.org/10.24203/ajas.v10i5.6950.
- [66] T. Z. Kalanov, "On the correct formulation of the first law of thermodynamics", *In APS April Meeting Abstracts*, pp. D1-055, 2006.
- [67] S. Carnot, R. Clausius, and W. T. B. Kelvin, *The Second Law of Thermodynamics*, American Book Company, 1899.
- [68] R. Luzzi, Á. R. Vasconcellos, and J. G. Ramos, "On the statistical foundations of irreversible thermodynamics", *Fortschritte der Physik: Progress of Physics*, Vol. 47, no. 4, pp. 401-432, 1999.
- [69] L. Onsager, "Reciprocal relations in irreversible processes", *I. Physical review*, Vol. 37, no. 4, p. 405, 1931, doi.org/10.1103/PhysRev.37.405.
- [70] M. Planck, "On the law of the energy distribution in the normal spectrum", *Ann. Phys*, Vol. 4, no. 553, pp. 1-11, 1901, doi.org/10.1016/B978-0-08-012102-4.50013-9.
- [71] S. Shahsavari, M. Moradi, and M. Esmailpour, "On the Irreversibility in Mechanical Systems Using a New Macroscopic Energy Structure Modeling", *Asian Journal of Applied Sciences* (ISSN: 2321–0893), Vol. 8, no. 6, 2020, doi.org/10.24203/ajas.v8i6.6473.
- [72] M. R. von Spakovsky, "The second law: A unified approach to thermodynamics applicable to all systems and all states", *In AIP Conference Proceedings*, Vol. 1033, no. 1, pp. 302-308, American Institute of Physics, 2008, doi.org/10.1063/1.2979049.
- [73] V. N. Pokrovskii, "A derivation of the main relations of nonequilibrium thermodynamics", *International Scholarly Research Notices*, 2013, doi.org/10.1155/2013/906136.
- [74] M. Esposito, and C. Van den Broeck, "Three faces of the second law. I. Master equation formulation", *Physical Review E*, Vol. 82, no. 1, p.011143, 2010, doi.org/10.1103/PhysRevE.82.011143.
- [75] M. S. Ma, and R. Zhao, "Corrected form of the first law of thermodynamics for regular black holes", *Classical and Quantum Gravity*, Vol. 31, no. 24, p.245014, 2014, doi.org/10.1088/0264-9381/31/24/245014.
- [76] T. W. Xue, and Z. Y. Guo, "What is the real Clausius statement of the second law of thermodynamics", *Entropy*, Vol. 21, no. 10, p.926, 2019.
- [77] V. N. Pokrovski, "Extended thermodynamics in a discrete-system approach", *European journal of physics*, Vol. 26, no. 5, p.769, 2005, doi.org/10.1088/0143-0807/26/5/009.
- [78] V. A. Etkin, "Methodological principles of modern thermodynamics", arXiv preprint arXiv:1401.0550, 2014.
- [79] J. Serrin, "Conceptual analysis of the classical second laws of thermodynamics", *Archive for Rational Mechanics and Analysis*, Vol. 70, no. 4, pp. 355-371, 1979, doi.org/10.1007/BF00281160.
- [80] P. Podio-Guidugli, "A virtual power format for thermomechanics", *Continuum Mechanics and Thermodynamics*, 20, pp. 479-487, 2009, doi.org/10.1007/s00161-009-0093-5.